

Towards realistic modelling of free-solution electrophoresis: a case study on charged macromolecules

DISSERTATION
zur
Erlangung des Doktorgrades
der Naturwissenschaften

vorgelegt beim Fachbereich Physik
der Goethe-Universität Frankfurt am Main

von
Kai Christian Grass

aus
Bielefeld

Frankfurt (2009)

vom Fachbereich Physik der Goethe-Universität
Frankfurt am Main als Dissertation angenommen.

Dekan: Prof. Dr. Dirk-Hermann Rischke

1. Gutachter: PD Dr. Christian Holm

2. Gutachter: JP Dr. Karin Hauser

Datum der Disputation: 2. März 2009

Abstract

This thesis contributes to the field of soft matter research and studies the importance of hydrodynamic interactions during free-solution electrophoresis of linear polyelectrolytes by means of coarse-grained molecular dynamics simulations including full electro-hydrodynamic interactions. The center of attention is the specific role of hydrodynamic interactions on the electrophoretic behaviour of charged macromolecules. Points of interest are the dependence of hydrodynamic interactions on the chain length, the chain flexibility and the surrounding counterions, and their combined influence on important observables such as the static chain conformations and the dynamic transport coefficients, *i.e.*, the diffusion and the electrophoretic mobility. These problems are addressed by extensive computer simulations that are quantitatively matched with experimental results. Existing theoretical predictions are carefully examined and are augmented by the observations in this thesis.

Starting with the static chain properties of the polyelectrolyte and the counterion distribution around the chain, the influence of hydrodynamic and electrostatic interactions is investigated, especially with respect to the screening due to a finite salt concentration in the solution. Additionally, the perturbation by an external electric field is studied and it is shown that, within the linear response regime, static and dynamic properties are not affected by the electric field.

The dynamic properties of flexible polyelectrolyte chains are determined in dependence of the chain length. The comparison of the simulations to existing theories and experiments underlines the importance of hydrodynamic interactions. The simulations can be quantitatively matched to available experimental data and specifically show the experimentally observed maximum in the electrophoretic mobility for intermediate chains, currently not covered by existing theories.

To understand this interesting behaviour on a microscopic level, five independent estimators are formulated and used to determine the effective charge of the polyelectrolyte. The estimators are analysed with respect to their accuracy, as well as their applicability and efficiency in simulations and their transferability to experiments. The effective charge of the polyelectrolyte turns out to be reduced by counterions surrounding the chain and moving with the polyelectrolyte. An important observation in this context is the fact that the effective charge is not depending on hydrodynamic interactions.

Additionally, it is shown that the counterions have a crucial influence on the effective friction of the polyelectrolyte complex during electrophoresis. Based on the mobility measurements and on the charge estimates, the length-dependence of the effective friction is quantified and exhibits a sharp decrease in the friction per monomer due to hydrodynamic shielding. This shielding is reduced as the chain length

Abstract

is increased, indicating an equal exposure of all parts of the chain to the fluid. The results clearly show a screening of hydrodynamic interactions, which is explained by the presence of counterions creating a fluid flow inside the polyelectrolyte coil. The associated screening length is similar to the Debye length for electrostatic screening, emphasizing the role of counterions.

With the analysis of the effective charge and the effective friction a detailed picture of the dynamic behaviour of charged macromolecules during electrophoresis is created. The previously unexplained mobility maximum is shown to be a direct consequence of a different scaling of charge and friction. Similarly, the constant free-solution mobility of long polyelectrolyte chains, the free-draining behaviour, can be attributed to the linear dependence on chain length of both properties for sufficiently long chains.

The detailed microscopic understanding of the underlying processes during free-solution electrophoresis with respect to the interplay between hydrodynamic and electrostatic forces paved the way for studying compounds consisting of a polyelectrolyte and an attached drag-tag, like they are used for end-labeled free-solution electrophoresis. The contribution of various drag-tags to the total effective friction based on their hydrodynamic size is studied in order to contribute to the improvement of this method for the separation of polyelectrolytes in free-solution.

Summarizing, the main results and observations of this thesis contribute to the theoretical understanding of polyelectrolyte electrophoresis and provide an in-depth understanding of the microscopic processes that govern the macroscopic behaviour of charged polyelectrolytes in free-solution electrophoresis. Having a simulation model at hand, which matches the experimental data and confirms theoretical predictions, opens new possibilities of investigating the dynamic behaviour of charged macromolecules. Due to the complex interactions between the system components, a purely theoretical description is often not possible or too general to provide insight into a specific problem. Under the right assumptions, the problem remains tractable by simulations. This highlights their general importance in the area of soft matter research and specifically the contribution made by the presented work.

Ausführliche Zusammenfassung

Im Rahmen der vorliegenden Doktorarbeit aus dem Forschungsgebiet der sogenannten „Weichen Materie“ (soft matter) wird im Besonderen der Einfluss hydrodynamischer Wechselwirkungen auf die Elektrophorese linearer Polyelektrolyte in freier Lösung, d. h. in Abwesenheit eines trennenden Gels, untersucht. Hierzu wird eine vergrößerte Molekulardynamiksimulation verwendet, die die vollständigen elektrostatischen und hydrodynamischen Wechselwirkungen zwischen allen Komponenten des Systems berücksichtigt. Ein besonderes Gewicht liegt auf der Analyse der Rolle der Hydrodynamik für das elektrophoretische Verhalten geladener Makromoleküle. Diese Arbeit untersucht die Längenabhängigkeit der hydrodynamischen Wechselwirkungen, den Einfluss der Kettenflexibilität und der das Polyelektrolyt umgebenden Gegenionen, sowie ihre gemeinsame Wirkung auf die dynamischen Transportkoeffizienten, die Diffusion und die elektrophoretische Mobilität. Diese Problemstellung wird mit Hilfe umfangreicher Computersimulationen bearbeitet, deren Ergebnisse quantitativ mit experimentellen Resultaten verglichen werden können. Dabei werden bestehende Theorien sorgfältig analysiert und durch die in dieser Arbeit ermittelten Erkenntnisse erweitert.

Polyelektrolyte als Teil der Weichen Materie

Die Erforschung der Weichen Materie ist ein relativ neues Forschungsgebiet, das sich verschiedenen Problemklassen von Teilchensuspensionen über Polymerlösungen zu Zellnetzwerken widmet. Darin eingeschlossen sind Strukturen in fast allen biologischen Systemen – so auch die im menschlichen Körper. Die unterschiedlichen Prozesse, in denen diese Strukturen involviert sind, haben oft eine gemeinsame Längen- und Energieskala auf der Größenordnung von Nano- bis Mikrometern bzw. vergleichbar mit der thermischen Energie der Umgebung. Die relevanten Zeitskalen variieren dabei zwischen Bruchteilen von Sekunden bis hin zu Stunden.

Computersimulationen kommt seit jeher eine wichtige Rolle bei der Studie derartiger Systeme zu, wobei deren komplexe Natur jedoch eine große Herausforderung darstellt. Biologische Vorgänge sind häufig von starkvariierenden lokalen Kräften dominiert, die nur mit höherem Modellierungsaufwand erfasst werden können. Vergrößerte Simulationsmodelle auf mesoskopischen Längenskalen erweisen sich dabei als besonders erfolgreich in der Bewältigung dieser Probleme, in dem sie die Komplexität auf die essentiellen Eigenschaften der mikroskopischen Physik reduzieren, die dann mit aktuellsten Algorithmen auf Hochleistungsrechnersystemen effizient gelöst werden können.

Ausführliche Zusammenfassung

Diese Doktorarbeit widmet sich hauptsächlich der Klasse der Polyelektrolyte, d.h. geladenen molekularen Ketten. Sie übernehmen eine fundamentale Rolle in der Strukturbildung, der Stabilität in verschiedensten molekularen Systemen. Ihre einzigartigen Eigenschaften werden in einer Vielzahl von technischen und industriellen Anwendungen nutzbar gemacht, das wichtigste Einsatzgebiet ist jedoch die Biologie bzw. die Biochemie. Dies liegt daran, dass faktische alle Proteine sowie die Erbsubstanz, die DNS, selbst geladene Makromoleküle sind.

Leider ist das theoretische Verständnis ihrer Eigenschaften weniger gut vorangeschritten als das neutraler Polymere, da sich die Beschreibungen in wichtigen Punkten unterscheiden. Insbesondere sind die Wechselwirkungen unterschiedlicher Polyelektrolyten untereinander bis dato größtenteils unerforscht.

Die Polyelektrolytcharakterisierung erfolgt hauptsächlich durch Elektrophorese, mit der es zum Beispiel gelungen ist, die menschliche DNS zu trennen und so das gesamte Genom zu entschlüsseln. Dieser Erfolg erhöht den Bedarf an verbesserten und schnelleren Sequenzierungsmethoden, um auch zukünftige Herausforderungen bewältigen zu können.

Hierzu ist ein grundlegendes Verständnis des Verhaltens geladener Polyelektrolyte in externen elektrischen Feldern notwendig. Das Ziel dieser Arbeit ist, dieses fundamentale Wissen für den Prozess der elektrophoretischen Separation zu erarbeiten. Aus dem breiten Anwendungsspektrum der Elektrophorese folgt, dass die erzielten Ergebnisse von großer Relevanz für die Forschung auf den Gebieten der Elektrophorese, der Mikrofluidik und darüber hinaus sind.

Statische und dynamische Eigenschaften

Angefangen bei den statischen Ketteneigenschaften eines Polyelektrolyts sowie der Verteilung der Gegenionen um diese Kette wird der Einfluss der Hydrodynamik und der Elektrostatik systematisch untersucht, insbesondere im Hinblick auf die Abschirmung dieser Wechselwirkungen durch die Gegenwart von Salzionen in der Lösung. Zusätzlich wird der Störeinfluss betrachtet, der von einem externen angelegten elektrischen Feld ausgeht.

Dabei wird gezeigt, dass für kleine Feldstärken im „linearen Antwortbereich“ (linear response regime) statische und dynamische Ketteneigenschaften nicht beeinflusst sind. Die Ergebnisse zeigen das theoretisch erwartete Verhalten für Polyelektrolytketten: die Kettengröße, ausgedrückt durch den End-zu-End-Abstand, den Gyrationradius sowie den hydrodynamischen Radius, wächst für kurze Ketten mit einem Exponenten, der zwischen 1 und dem Floryexponenten für ungeladene Ketten liegt. Es wird gezeigt, dass der effektive Skalierungsexponent abnimmt, wenn die Salzkonzentration und damit die elektrostatische Abschirmung erhöht wird.

Darüberhinaus wird der Einfluss des externen elektrischen Felds auf die Kettenkonformationen und die Verteilung der Gegenionen untersucht. Unterhalb eines kritischen Wertes ist, in Übereinstimmung mit der linearen Antworttheorie, keine Abhängigkeit von der Feldstärke beobachtbar. Höherer Feldstärken verändern

die statischen (und auch der dynamischen) Eigenschaften der Polyelektrolyte. Die Grenze zwischen linearer und nicht linearer Wirkung des elektrischen Feldes wird ermittelt und liegt im theoretisch vorhergesagten Bereich.

Anschließend werden die dynamischen Eigenschaften flexibler Polyelektrolytketten in Abhängigkeit von der Kettenlänge bestimmt. Dabei wird das Modell angepasst, sodass die Transportkoeffizienten von Polystyrenesulfonaten (PSS) bestimmt werden können. Diese werden dann mit den Ergebnissen zweier unabhängiger experimenteller Messungen verglichen. Es kann eine quantitative Übereinstimmung zwischen den Simulationsergebnissen und den Experimenten sowie den theoretischen Vorhersagen hergestellt werden, solange die hydrodynamischen Wechselwirkungen zwischen Polyelektrolyt, Gegenionen und Lösungsmittel korrekt berücksichtigt werden. Ein Simulationsmodell, welches diese Wechselwirkungen vernachlässigt, ist nicht in der Lage, das dynamische Verhalten kurzer PSS-Ketten zu beschreiben. Dahingegen ist es möglich, die chemischen Details des Moleküls zu vernachlässigen und nur eine generalisierte Darstellung eines Polyelektrolyts zu verwenden.

Zusätzlich wird die Rolle der Gegenionen und der Einfluss der Stärke des elektrischen Feldes untersucht, wobei der Schwerpunkt aber auf der Betrachtung hydrodynamischer Wechselwirkungen liegt, deren enorme Wichtigkeit besonders durch den Vergleich zu den experimentellen Daten unterstrichen wird. Darüberhinaus zeigen die Simulationen das experimentell beobachtete Maximum in der elektrophoretischen Mobilität für Ketten von mittlerer Länge, welches derzeit nicht in der Theorie erfasst ist.

Effektive Ladung und effektive Reibung

Um das Verständnis dieses Verhaltens auf mikroskopischer Ebene zu erweitern, werden fünf unabhängige Schätzer zur Bestimmung der effektiven Ladung des Polyelektrolyts formuliert, die im Hinblick auf ihre Genauigkeit, ihre Anwendbarkeit und Effizienz für Simulationen sowie im Bezug auf die Bedeutung im experimentellen Rahmen untersucht werden. Die Analyse zeigt, dass die effektive Ladung des Polyelektrolyts teilweise durch die die Ketten umgebenden und sich mit ihr bewegenden Gegenionen reduziert wird. Eine hervorhebenswerte Beobachtung in diesen Zusammenhang ist die Tatsache, dass die ermittelte effektive Ladung unabhängig von der Art und Stärke der hydrodynamischen Wechselwirkungen ist.

Zwei dieser Schätzer sind besonders vielversprechend. Für den auf einem reinen Langevinmodell basierende Schätzer ist es nur notwendig, die elektrophoretische Mobilität zu bestimmen. Alle anderen Parameter ergeben sich direkt aus dem Modell. Die Tatsache, dass die effektive Ladung unabhängig von den hydrodynamischen Wechselwirkungen ist, erlaubt die Bestimmung der Mobilität unter Vernachlässigung dieser bei geringem Simulationsaufwand.

Die Abschätzung über die Ionendifusionsmessung ist numerisch aufwändiger, hat aber den entscheidenden Vorteil gegenüber allen anderen Methoden, dass es möglich ist, sie direkt in einer experimentellen Messung anzuwenden. Alle notwendigen

Größen, d.h. der freie Diffusionskoeffizient der Ionen, der Diffusionskoeffizient der gebundenen Ionen und der Polyelektrolytdiffusionskoeffizient, können mittels Standardverfahren bestimmt werden. Dieser Schätzer ist der erste, der eine direkte Messung einer mikroskopischen Eigenschaft, hier der effektiven Ladung, im Experiment erlaubt.

Mit der effektiven Ladung wird außerdem der wichtige Beitrag der Gegenionen zur effektiven Reibung des Polyelektrolytkomplexes mit dem Lösungsmittel während der Elektrophorese herausgestellt. Ausgehend von den Mobilitätsmessungen sowie den Schätzungen für die effektive Ladung ist es möglich, die effektive Reibung in Abhängigkeit von der Kettenlänge zu quantifizieren. Es zeigt sich mit steigender Länge ein anfänglicher steiler Abfall der Reibung pro Monomer bedingt durch die hydrodynamische Abschirmung der Monomere untereinander. Diese Abschirmung nimmt mit Wachstum der Kettenlänge ab, welches ein Hinweis darauf ist, dass alle Bereiche der Kette im gleichen Maße der Flüssigkeit ausgesetzt sind. Die Analyseergebnisse zeigen darüberhinaus eindeutig die Abschirmung der hydrodynamischen Wechselwirkungen, die mit der Präsenz von Gegenionen und des von ihnen erzeugten Flüssigkeitsflusses erklärt werden kann. Die zugordnete Abschirmlänge ist vergleichbar mit der Debyelänge zur elektrostatischen Abschirmung, welches zusätzlich die Rolle der Gegenionen zur Dynamik unterstreicht.

Die Analyse der effektiven Ladung und der effektiven Reibung erzeugt ein detailliertes Bild des dynamischen Verhaltens geladener Makromoleküle während der Elektrophorese. Das zuvor unerklärte Mobilitätsmaximum ergibt sich hierbei als direkte Folge einer unterschiedlichen Abhängigkeit von Ladung und Reibung gegenüber der Länge des Polyelektrolyts. Gleichmaßen ist es möglich, die konstante elektrophoretische Mobilität langer Polyelektrolytketten, das sogenannte „Durchdringungsregime“ (free-draining), auf die lineare Abhängigkeit beider Größen von der Länge für lange Ketten zurückzuführen.

Polyelektrolyte mit molekularem Anhang

Das detaillierte mikroskopische Verständnis der zugrundeliegenden Prozesse während des Elektrophoresevorgangs in freier Lösung im Hinblick auf die Wechselwirkung von hydrodynamischen und elektrostatischen Kräften bereitet den Weg für das Studium zusammengesetzter Moleküle bestehend aus einem Polyelektrolyt und einem angehängten Reibungskern, wie sie für die „Elektrophorese in freier Lösung mit molekularem Anhang“ (end-labeled free-solution electrophoresis) verwendet werden. Diese Arbeit untersucht den Beitrag der verschiedenen Reibungskerne zur Gesamtreibung basierend auf ihrer hydrodynamischen Größe, und trägt damit zur Verbesserung dieser Methode zur Separation von Polyelektrolyten in freier Lösung bei.

Nach einer Analyse der bestehenden Theorie auf Grundlage der Erkenntnisse dieser Arbeit wird das Simulationsmodell für die Bestimmung der elektrophoretischen Mobilität eines Polyelektrolyts verwendet, welches an einem Ende mit einem

linearen ungeladenen Polymer verbunden ist. Die Ergebnisse werden in guter Übereinstimmung mit der erweiterten Theorie verglichen.

Im Anschluss wird das lineare Polymer durch ein verzweigtes Polymer ersetzt, um kürzlich getroffene Vorhersagen zu überprüfen. Hierbei wird gezeigt, dass der zusätzliche Reibungsbeitrag der von dem angehängten Molekül ausgeht, direkt proportional zu seiner hydrodynamischen Größe ist. Im Vergleich mit den Simulationen des linearen Polymers zeigt sich, dass der Reibungsbeitrag pro Monomer am größten für die unverzweigte Kette ist. Experimentelle Einschränkungen in der Synthese dieser Moleküle begrenzen jedoch ihre praktische Anwendbarkeit. Hier schafft das Anhängen von Seitenketten Abhilfe, da es die Möglichkeit bietet, die hydrodynamische Größe und damit den Reibungsbeitrag zu erhöhen, ohne die lineare Länge des Polymers zu verändern. Es wird gezeigt, dass die Effektivität eines derartigen verzweigten Moleküls mit der Länge der Seitenketten zunimmt.

Die dritte Klasse von möglichen molekularen Anhängen, die untersucht wird, scheint in besonderem Maße für die Anwendung in der Polyelektrolytseparation geeignet zu sein. Temporär gebundene Mizellen verfügen über einen signifikant höheren Reibungsbeitrag, da sie einen großen hydrodynamischen Radius besitzen. Die Untersuchung zeigt, dass der Reibungskoeffizient linear mit der Größe der Mizelle zunimmt. Daraus ergibt sich, dass die Wirksamkeit dieser Anhangklasse nur durch die Größe der synthetisierbaren Mizellen begrenzt ist.

Das erfolgreiche Zusammenspiel von Theorie und Computersimulation dazu trägt dazu bei, die Entwicklung neuer Anhangsmoleküle zu unterstützen, und erweitert somit die Anwendbarkeit dieser Methode der elektrophoretischen Separation.

Realistische Modellierung der Elektrophorese

Diese Arbeit bietet eine detaillierte Studie des Einfluss hydrodynamischer Wechselwirkungen auf die Elektrophorese geladener Makromoleküle auf der Basis einer vergrößerten Molekulardynamiksimulation unter Berücksichtigung der vollständigen elektrohydrodynamischen Wechselwirkungen.

Die Hauptergebnisse und Beobachtungen liefern einen Beitrag zum theoretischen Bild der Polyelektrolytelektrophorese und bieten ein tiefgehendes Verständnis der mikroskopischen Prozesse, die das makroskopische Verhalten geladener Makromoleküle in freier Lösung bestimmen.

Ein Simulationsmodell, welches die experimentellen Beobachtungen abbilden und bestätigen kann, eröffnet neue Möglichkeiten, das elektrophoretische Verhalten kurzer Polyelektrolytketten zu untersuchen, welches bislang nur unzureichend durch bestehende Theorien erfasst ist. Die Komplexität der Wechselwirkung zwischen den einzelnen Systembestandteilen verhindert eine exakte analytische Beschreibung. Unter geeigneten Annahmen ist das Problem jedoch mit Hilfe von Computersimulationen zu beschreiben. Dies unterstreicht die Wichtigkeit solcher Simulationen für die Forschung auf dem Gebiet der Weichen Materie und den Beitrag, den diese Arbeit leistet.

Contents

Abstract	iii
Ausführliche Zusammenfassung	v
1. Introduction	1
1.1. Polyelectrolyte electrophoresis	1
1.2. State of the art	2
1.3. Aim of this work	3
1.4. Overview	3
2. Theoretical background on polyelectrolytes in free-solution	7
2.1. Hydrodynamics	7
2.2. Polymer chains	11
2.3. Diffusion of polymer chains	16
2.4. Polyelectrolytes	20
2.5. Electrophoresis of polyelectrolytes	25
2.6. Model requirements	29
3. A coarse-grained model for polyelectrolytes	31
3.1. On physical and computational complexity	31
3.2. The model at a glance	33
3.3. Coarse-grained molecular dynamics	34
3.4. Continuum electrostatics	35
3.5. Modelling the fluid	38
3.6. System parameters	45
3.7. Implementation	48
4. Static properties of polyelectrolytes in electric fields	49
4.1. Introduction	49
4.2. Visualisation	50
4.3. Chain scaling	50
4.4. Counterions	54
4.5. Summary	60

5. Dynamic properties	61
5.1. Introduction	61
5.2. Experimental techniques	62
5.3. Determining transport coefficients in simulations	64
5.4. Results	67
5.5. Summary	76
6. Effective charge and effective friction	77
6.1. Introduction	77
6.2. Charge estimators	77
6.3. Effective friction	85
6.4. Counterion induced hydrodynamic screening	87
6.5. Summary	88
7. Size-separation by end-labeled free-solution electrophoresis	91
7.1. Introduction	91
7.2. Theory	93
7.3. Modelling drag-tags	95
7.4. Linear drag tags	96
7.5. Branched drag tags	102
7.6. Micellar drag tags	104
7.7. Summary	106
8. Outlook: Other free-solution separation methods	109
8.1. Surface electrophoresis	109
8.2. Confinement-driven separation	110
9. Concluding remarks	113
A. Green-Kubo formula for the electrophoretic mobility	117
B. Sample ESPResSo scripts	121
B.1. Simulation script	121
B.2. Analysis script	136
Acknowledgments	145
Bibliography	147
Curriculum Vitae	163

1. Introduction

The field of *soft matter* research is a relatively new field that deals with various problems, ranging from particle suspensions over polymer solutions to cell networks. This includes most of the structures in actual biological systems – such as the human body. These different systems typically share a mesoscopic length scale, *i.e.*, their relevant dimensions are of the order of nano- to micrometers, and the processes happen at energy scales comparable to the thermal energy. On the other hand, the relevant time scales can be as short as nanoseconds or as long as hours.

Computer simulations have played an important role in the study of soft matter systems, but their complex nature poses great challenges. Additionally to the length, energy and time scale requirements, biological processes are often driven by strongly varying forces, which increase the complexity of the modelling. Mesoscopic or coarse-grained simulation methods show promising results in dealing with this complexity by reducing the system properties to the essential features of the microscopic physics. The system can then be efficiently solved using state-of-the-art algorithms on high-performance computer systems.

The aim of soft matter research is to test physical theories, predict previously untested behaviours, and create ideas for novel experimental approaches. The focus of this thesis is the study of free-solution electrophoresis of polyelectrolytes, and in particular to elucidate the role of hydrodynamic interactions on mesoscopic length scales.

1.1. Polyelectrolyte electrophoresis

Polyelectrolytes are charged macro-molecular chains, commonly present in soft matter systems. They play a fundamental role in determining the structure, stability and interactions of various molecular assemblies, and their unique properties are being exploited in a wide range of technological and industrial fields. One of their major roles, however, seems to be the one played in biology and biochemistry. This is due to the fact that virtually all proteins, as well as the DNA and RNA, are polyelectrolytes.

Unfortunately, the theoretical understanding of polyelectrolytes is little developed as the approaches describing their statistical properties differ profoundly from those of their uncharged counterparts. Furthermore, their interactions with each other and with the other biomolecules is not completely understood. This is mainly due to the difficult treatment of long range interactions in theory and simulations. Promising approaches using approximations will be discussed in the next section.

1. Introduction

Electrophoresis is one of the main experimental techniques employed to characterise polyelectrolytes. Furthermore, it is widely used to separate DNA molecules by size and has shown its effectiveness in the sequencing of entire genomes, including our own [1]. This success story also increased the demand for improved and faster sequencing methods, in order to meet the upcoming challenges.

1.2. State of the art

Over the last years, many experimental investigations have been performed in the field of polyelectrolyte electrophoresis, in order to improve existing methods or to develop new separation techniques which yield a faster or better separation [2–18]. These experimental improvements gave rise to many interesting questions that still need to be dealt with from a theoretical point of view.

Biomolecules like DNA and proteins are usually charged, and predominantly exist in aqueous solutions. The dynamics of biomolecules in such an environment is determined by an interplay of various factors: external forces, the local flow of the medium, short-range interactions, long-range electrostatic and hydrodynamic interactions. Externally applied flow or external electric fields are used to manipulate and separate biomolecules in analytic devices.

In order to understand these processes from a theoretical point of view, the biomolecules must be modeled with high detail. However, a full simulation of a microchannel, which accounts explicitly for every single water molecule, is not only a formidable task, but also unnecessarily inefficient. Since typical channel sizes are still much larger than the size of small molecules, a solvent treatment on the level of a continuum theory is perfectly sufficient. On the other hand, simplified models, which replace the solvent, the counterions, and the salt ions by effective interactions, miss many relevant physical phenomena.

So far, computer simulations of DNA electrophoresis have often used Brownian dynamics [19–25], *i.e.*, the medium was replaced by a simple random noise and friction term. Furthermore, electrostatic interactions between the polyelectrolyte and the surrounding ions have not been accounted for. This treatment was reasonably successful, and led to results which were in accord with experiments both for the cases of gel electrophoresis [19–21] and electrophoresis in microchannels [24, 25].

However, a closer inspection shows that there are problems with such a simplified description: first, the often assumed hydrodynamic screening only applies to the mobility of DNA in free solution. If the DNA is stopped by an obstacle, the hydrodynamic drag of the DNA is no longer balanced by the counterion friction, because the counterions are still mobile [26]. Furthermore, hydrodynamic interactions affect the diffusion of the chain [27, 28], and for systems of many molecules intricate inter-particle effects exist, as is known from colloidal dispersions [29, 30] and neutral polymer solutions [31].

Second, a theory which accounts for the electrostatic screening on a mean-field level without explicit counterions, like a linearised or fully nonlinear Poisson-

Boltzmann treatment, cannot describe the subtle dependence of the free-solution mobility of DNA on the composition of the buffer - the salt concentration, the pH, the valency of the ions etc. [32, 33]. Already for the static case drastic deviations from this mean-field description are known to occur, namely, effective attractions between like charged macromolecules [34] and the effect of overcharging, where the macro ion charge gets overcompensated by its (usually multivalent) counterions [35].

Now, looking at a non-equilibrium situation as it is the case in an electrophoresis experiment, one has to account for the fact that a certain amount of the counterions surrounding the DNA may be dragged along with the DNA, which leads to an effective charge renormalisation. The amount of co-moving counterions, however, may depend in a subtle way on the hydrodynamic interactions.

1.3. Aim of this work

While there exist several theories [36–39] that have been successfully used to describe qualitatively the experimentally observed behaviour of various polyelectrolytes, there are still many open problems to address.

A thorough understanding of the behaviour of polyelectrolytes in external fields is needed in order to improve current electrophoretic separation methods and to support the development of new methods for efficient separation of charged biopolymers by length. This has recently become an area of significant activity due to the fact that genome sequencing techniques make heavy use in electrophoretic separation techniques.

The aim of this thesis is to provide fundamental understandings of the electrophoretic separation process. Based on the existing experimental results, a coarse-grained simulation model will be developed that allows to treat all the necessary interactions with the required accuracy. Based on this model, recently suggested electrophoresis methods will be tested and characterised. Ultimately, this work can contribute to the the design of novel separation techniques. Since the thesis deals with a topic which is beneficial for a wide variety of potential applications, the achieved results should be of broad interest to the electrophoresis, microfluidics, nano science community, and beyond.

1.4. Overview

This thesis is organised as follows:

Chapter 2 provides the theoretical framework and established concepts that will be used throughout the thesis to interpret and analyse the results of this work.

Chapter 3 outlines the simulation model used to describe the behaviour of polyelectrolytes during free-solution electrophoresis.

1. Introduction

Chapter 4 contains the results on the static properties of polyelectrolytes and the surrounding counterions as obtained from the simulations.

Chapter 5 is dedicated the dynamical properties of polyelectrolytes as measured in electrophoretic experiments.

Chapter 6 offers a detailed analysis of the electrophoretic mobility of polyelectrolytes, especially with regards to length dependence by determining the effective friction of the polyelectrolyte chain and its surrounding counterions with the solvent.

Chapter 7 studies the modification of the effective friction in the process of free-solution electrophoresis by attaching additional drag targets to the polyelectrolyte chains.

Chapter 8 provides a brief outlook on further free-solution separation techniques for polyelectrolytes.

Chapter 9 summarises the results and concludes this thesis.

The main part of the thesis is followed by a brief appendix that contains the derivation of the Green-Kubo expression to determine the electrophoretic mobility at vanishing external electric field (Equation 5.4). A second appendix contains an annotated simulation script.

The work of Chapters 4 through 6 has been concisely presented in the following publications:

- K. Grass, U. Böhme, U. Scheler, H. Cottet, and C. Holm. Importance of hydrodynamic shielding for the dynamic behavior of short polyelectrolyte chains. *Physical Review Letters*, 100(9):096104, 2008;
- K. Grass and C. Holm. On the importance of hydrodynamic interactions in polyelectrolyte electrophoresis. *J. Phys.: Condens. Matter*, 20(494217), 2008;
- K. Grass and C. Holm. Polyelectrolytes in electric fields: Measuring the dynamical effective charge and effective friction. *Soft Matter*, *accepted*, 2009. <http://arxiv.org/abs/0902.1886>.

The results of Chapter 7 are prepared for publication as:

- K. Grass, C. Holm, and G. W. Slater. Optimizing end-labeled free-solution electrophoresis by increasing the hydrodynamic friction of the drag labels. *Submitted to Macromolecules*, 2009. <http://arxiv.org/abs/0902.1889>.

Furthermore, the author contributed to a comprehensive review on separation methods for DNA:

- G. W. Slater, C. Holm, M. V. Chubynsky, H. W. de Haan, A. Dubé, K. Grass, O. A. Hickey, C. Kingsburry, D. Sean, T. N. Shendruk, and L. Zhan. Modeling separation processes: A review of current computer simulation methods. *Electrophoresis*, (30):792–818, 2009.

2. Theoretical background on polyelectrolytes in free-solution

This chapter introduces the main theoretical concepts that will be used to describe the properties of polyelectrolytes during free-solution electrophoresis.

Firstly, the theory of hydrodynamic interactions will be briefly reviewed, then the standard polymer theory will be summarised. Following the static properties, the dynamic quantities will be investigated. After describing the polymers, the polyelectrolytes – the charged equivalent of polymers – will be introduced.

The chapter concludes by formulating the requirements for the simulation model presented in the next chapter.

2.1. Hydrodynamics

In order to study the behaviour of particles within a solvent, a precise understanding of the fluid is needed. Due to the nonlinear and long-range nature of the forces involved, fluid mechanics is a highly complex topic and a complete description of hydrodynamic interactions easily fills books, such as the standard references by H. Lamb [45] or by Landau and Lifshitz [46]. The essential concepts and quantities that will be used throughout this thesis are briefly summarised in the following.

2.1.1. What are hydrodynamic interactions?

The Merriam-Webster’s dictionary¹ defines *hydrodynamics* as “. . . a branch of physics that deals with the motion of fluids and the forces acting on solid bodies immersed in fluids and in motion relative to them”.

Simply speaking, hydrodynamic interactions are long-range interactions arising within a fluid. An object that is moved through the fluid creates a movement of fluid particles around its surface called *flow*. This local disturbance of the fluid propagates through the medium. It can affect the movement of another object: if the flow created by the first object is strong enough, the second object might even be dragged along. The interaction necessary to mediate this force is called *hydrodynamic interaction*. Likewise, the presence of an object, *e.g.*, a wall, inside a moving fluid can influence the flow and divert it in such a way that other objects inside the fluid are not affected by it any more. The first object (the wall) *shields* the second object from the flow, thereby reducing the force exerted by the fluid on this particle. This effect is called *hydrodynamic shielding*.

¹<http://mw1.m-w.com/dictionary>

2. Theoretical background on polyelectrolytes in free-solution

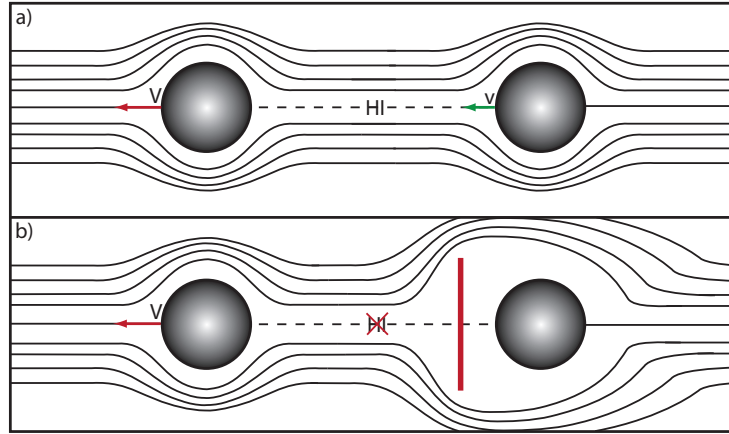


Figure 2.1: The motion of fluids and the forces acting on solid bodies immersed in them is called hydrodynamics. a) The flow created by a moving body can induce motion in a second body. b) An object placed in between the two bodies can block the hydrodynamic interactions (HI).

In the following section, the theoretical framework that describes hydrodynamics from a physicist's point of view is presented.

2.1.2. Navier-Stokes equation

In general, a fluid is composed of small particles or molecules that move around and collide with each other and with immersed objects following some conservation laws, namely the conservation of mass, momentum and energy known from classical mechanics. However, due to the large number of such particles within the fluid, a continuum assumption can be made. Only the combined effect of the individual fluid molecules is considered. In this case, the individual particle properties are replaced by averaged local quantities such as the density ρ and the flow velocity \vec{v} .

The dynamics of the continuous fluid are then described by the *Navier-Stokes equation*, which in its most general form can be written as:

$$\rho \left(\frac{\partial \vec{v}}{\partial t} + \vec{v} \cdot \nabla \vec{v} \right) = -\nabla p + \nabla \cdot \mathbb{T} + \vec{f}, \quad (2.1)$$

where \vec{v} is the fluid velocity, ρ is the fluid density, p is the pressure, \mathbb{T} is the general stress tensor, and \vec{f} sums all forces acting on the fluid, be that gravity, centrifugal forces, etc.

As the Navier-Stokes equation only ensures conservation of momentum, an additional equation has to be enforced for conservation of mass:

$$\frac{\partial \rho}{\partial t} + \nabla \cdot (\rho \vec{v}) = 0. \quad (2.2)$$

Equation 2.1 can be simplified if additional assumptions about the nature of the fluid are taken into account. In the present study, only incompressible Newtonian fluids will be considered, for which the stress tensor \mathbb{T} is proportional to the local strain $\nabla\vec{v}$ with the *dynamic viscosity* η as proportionality constant. In this case the Navier-Stokes equation can be simplified:

$$\rho \left(\underbrace{\frac{\partial\vec{v}}{\partial t}}_{\text{Unsteady acceleration}} + \underbrace{\vec{v}\cdot\nabla\vec{v}}_{\text{Convective acceleration}} \right) = \underbrace{-\nabla p}_{\text{Pressure gradient}} + \underbrace{\eta\nabla^2\vec{v}}_{\text{Viscosity}} + \underbrace{\vec{f}}_{\text{Other forces}}. \quad (2.3)$$

Solving the Navier-Stokes equation

In general, the set of Navier-Stokes equations (Eq. 2.1) is composed by nonlinear partial differential equations in almost every real situation. Few exceptions exist, for example, in one dimensional flow, called also the Stokes flow (or creeping flow), for which Eq. 2.1 boils down to the single ordinary differential equation that can be easily solved analytically. Due to the nonlinearity, many problems are difficult or impossible to solve analytically. Furthermore, no closed-form solutions are proved to exist for the unsimplified Navier-Stokes equations.

However, many computational methods to solve the Navier-Stokes equations are known: finite volume methods (FVM)², finite element methods (FEM)³, and finite difference methods (FDM)⁴ to name a few. All of these methods discretise the whole fluid volume into smaller elements, and the partial differential equations are specialised to these elements making them numerically solvable. In general, the accuracy of the solution depends on the geometry of flow and the chosen discretisation.

In the next chapter, *mesoscopic fluid models* will be introduced (see Section 3.5.2) that solve Navier-Stokes equations and allow for direct coupling to chosen simulation approach.

2.1.3. Important hydrodynamic quantities

When describing a specific fluid and its properties a whole zoo of hydrodynamic quantities can be used. So far, the fluid density ρ and the dynamic viscosity η have been introduced to describe the fluid itself. Often one is especially concerned with the ratio between the viscous force and the inertial force. This ratio is characterised by the *kinematic viscosity* ν :

$$\nu = \frac{\eta}{\rho}. \quad (2.4)$$

²<http://tinyurl.com/sdbp3>

³Ciarlet, Phillippe G. (1978). *The Finite Element Method for Elliptic Problems*. Amsterdam: North-Holland

⁴William F. Ames, *Numerical Methods for Partial Differential Equations*, Section 1.6. Academic Press, New York, 1977. ISBN 0-12-056760-1.

2. Theoretical background on polyelectrolytes in free-solution

As a guideline, the density of water is roughly $\rho = 1\text{g/cm}^3$, and its dynamic viscosity is $\eta \approx 1\text{mPa} \cdot \text{s} = 1\text{cP}$ (centi poise⁵). This leads to a kinematic viscosity of $\nu = 1\text{mm}^2/\text{s} = 1\text{cSt}$ (centi stokes).

To characterise the fluid flow, several dimensionless physical quantities have been introduced. Below the four most commonly used ones are listed. All of them describe the ratio between different physical aspects of the fluid and can be used to distinguish different flow characteristics.

The *Reynolds number* Re quantifies the ratio between the inertial forces ($V^2\rho D^2$) and the viscous forces (ηDV), where D is the relevant physical length scale, and it is a dimensionless quantity that is defined as follows:

$$\text{Re} = \frac{\rho V D}{\eta}, \quad (2.5)$$

with V being the average fluid velocity. The Reynolds number is used to describe the onset of turbulent flow. Flows with a Reynolds number below a critical value ($\approx 10^4$ for pipes) are laminar, whereas flows with a higher Reynolds number might show turbulence.

For example, the Reynolds number of the blood flow in the aorta is $\text{Re} \approx 10^3$, the one of a person swimming is $\text{Re} \approx 10^6$, and finally the one of a large ship moving at full speed is $\text{Re} \approx 10^9$.

The second dimensionless number, the *Schmidt number* Sc , defines the ratio of momentum diffusivity ($\propto \nu$) and mass diffusivity D :

$$\text{Sc} = \frac{\nu}{D} = \frac{\eta}{\rho D}. \quad (2.6)$$

As such, the Schmidt number relates the convective matter transport to the diffusive transport.

In liquids, such as water, $\text{Sc} \approx 1000$ and the momentum transport is much more prominent than actual matter transport. For example, while water waves collectively transport large momenta, the individual water molecule on average moves over very small distances.

Another dimensionless number is the *Knudsen number* Kn . It is a microscopic quantity defined as the ratio between the molecular mean free path length λ , the distance a molecule travels until the first collision, to a representative physical length scale L :

$$\text{Kn} = \frac{\lambda}{L}. \quad (2.7)$$

The Knudsen number can be used to determine whether a fluid should be described by statistical mechanics or by continuum mechanics. If $\text{Kn} > 1$, *i.e.*, the mean free path of a molecule is comparable or larger to the relevant length scale, a continuum approximation is no longer valid.

All problems discussed in this thesis have Knudsen numbers smaller than one.

⁵named after Jean Louis Marie Poiseuille

The *Mach number* Ma describes the speed of an object v moving through a fluid relative to the speed of sound c_s in it:

$$\text{Ma} = \frac{v}{c_s}. \quad (2.8)$$

Objects that move with a speed higher than $\text{Ma} = 1$ travel faster through a medium than the disturbance they cause to the medium. Obviously, this leads to strongly nonlinear effects that are not the subject of this thesis. All velocities in the systems of interest are subsonic with $\text{Ma} < 1$.

2.2. Polymer chains

The theoretical description of polymer chains in solution can be found nicely explained in several standard textbooks. The author especially recommends the works by M. Doi and S. F. Edwards, by M. Rubinstein and R. H. Colby, and by I. Teraoka [27, 47, 48]. The concepts essential for this thesis will be reviewed in this section.

A polymer is a molecule consisting of several identical repeating units, the monomers. The number N of monomers in a chain is also referred to as *degree of polymerisation*. Usually N is very large, *i.e.*, ranging up to 10^6 or more units, and the polymer properties depend less on the individual small monomer than on the total assembly of linked particles. Thus, it is possible to formulate a description which is independent on the chemical detail and use this generic model to describe polymers.

Many different models of this kind exist that differ in the way the polymer is described, but most of them can be mapped to one another in the limit of large N .

2.2.1. Ideal chains

An intuitively simple model, displayed in Figure 2.2, is the *freely jointed chain* (FJC) model, in which a polymer is described by a series of points that are linked by connections representing the polymer's bonds of fixed length b_0 . The FJC model belongs to the ideal chain models, *i.e.*, there are no interactions between two points i and j as long as they are separated by a sufficient number of bonds $|i - j| \gg 1$. As a consequence, it is possible that points of different parts of the chain overlap and the chain crosses itself. In Section 2.2.2, models for real chains, where the chain crossings are prevented, will be introduced and discussed.

If no external forces influence the chain conformations, long enough chains form an isotropic random coil with spherical shape maximizing the entropy that can be described by the *end-to-end vector* shown in Figure 2.2:

$$\vec{R}_e = \vec{r}_N - \vec{r}_1 = \sum_{i=1}^{N-1} \vec{b}_i, \quad (2.9)$$

2. Theoretical background on polyelectrolytes in free-solution

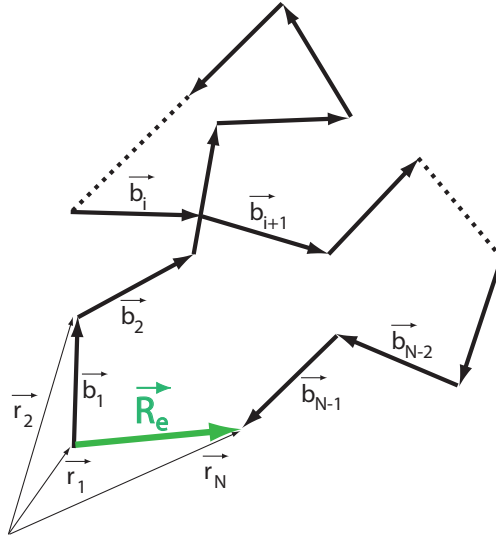


Figure 2.2: Scheme of the freely jointed chain model.

with \vec{r}_1 and \vec{r}_N being the position of the first and the last point of the polymer chain and the \vec{b}_i are the $(N - 1)$ bond vectors between the N points of the polymer.

One quantity that can be used to describe the random coil formed by an ideal chain is the *mean squared end-to-end distance*:

$$\langle R_e^2 \rangle = \sum_{i,j=1}^{N-1} \langle \vec{b}_i \cdot \vec{b}_j \rangle = \sum_{i=1}^{N-1} \langle b_i^2 \rangle + 2 \sum_{i=1}^{N-1} \sum_{j=i+1}^{N-1} \langle \vec{b}_i \cdot \vec{b}_j \rangle. \quad (2.10)$$

Here the $\langle \dots \rangle$ denote the averaging over *all* possible configurations $\vec{r}_1, \dots, \vec{r}_N$.

In the FJC model, the orientations of two different bond vectors \vec{b}_i and \vec{b}_j ($i \neq j$) are not correlated:

$$\langle \vec{b}_i \cdot \vec{b}_j \rangle = 0. \quad (2.11)$$

From Equations 2.10 and 2.11 one immediately obtains that characteristic length of the polymer, R_e , the average distance between both chain ends of a FJC polymer grows proportionally to the square root of the number of bonds $N - 1$:

$$R_e = \langle R_e^2 \rangle^{1/2} = b_0(N - 1)^{1/2}. \quad (2.12)$$

In other words, the random coil generated by the FJC model is an object with a fractal dimension of 2. Later, in Section 2.3.1, it will be shown how the random configurations of a polymer chain can be compared to the random movement of a particle in solution due to Brownian motion.

The scaling relation in Equation 2.12 also holds for other models describing ideal chains, most importantly for the *Gaussian chain* model, as long as Equation 2.11 is fulfilled. In this model, the distance between two connected monomers is no longer fixed to b_0 but is drawn randomly from a Gaussian distribution with a known average b . This average value b replaces b_0 as *effective bond length* in Equation 2.12.

A second quantity of importance is the *radius of gyration* R_g , which is defined similarly to the moment of inertia of a rigid body of N unit masses:

$$R_g^2 = \frac{1}{N} \sum_{i=1}^N (\vec{r}_i - \vec{r}_{\text{cm}})^2. \quad (2.13)$$

Here, $\vec{r}_{\text{cm}} = 1/N \sum_{i=1}^N \vec{r}_i$ is the center of mass of the chain. The average radius of gyration for an ideal chain exhibits the same scaling behaviour as the end-to-end distance:

$$R_g = \langle R_g^2 \rangle^{1/2} = \frac{b_0}{\sqrt{6}} (N - 1)^{1/2}. \quad (2.14)$$

The ideal chain models can be used to derive further observables for polymer chains, *i.e.*, *structure factors*, but they are omitted here, as they will not be used in this study.

2.2.2. Real chains

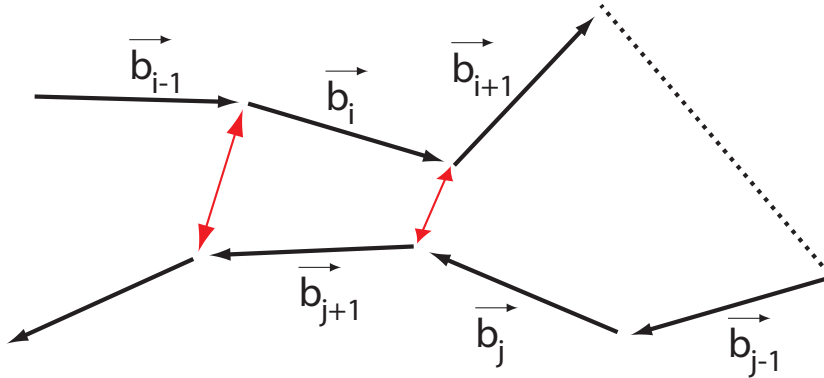


Figure 2.3: The excluded volume effect prevents two different chain segments from coming close to each other.

So far, theoretical models were discussed that described idealised chains only, where interactions between points separated by a couple of bond lengths were neglected. In reality, however, different parts of a polymer chain do interact if they come close to each other. The most obvious of such interactions is the steric interactions between the individual monomers of the polymer chain depicted in Figure 2.3.

2. Theoretical background on polyelectrolytes in free-solution

Each chain monomer has a finite size that prevents them from coming close to each other. This leads to a finite volume around each point from which all other points are excluded, with the resulting effect that the chain swells compared to the non-interacting one. The effect is called *excluded volume effect*.

Depending on the interactions between the chain monomers and interactions with the surrounding solvent the scaling exponent in Equations 2.12 and 2.14 will vary, and a more general formulation is needed:

$$R_e = \langle R_e^2 \rangle^{1/2} \approx (N - 1)^\nu, \quad (2.15)$$

and

$$R_g = \langle R_g^2 \rangle^{1/2} \approx (N - 1)^\nu. \quad (2.16)$$

Here, ν is the scaling exponent, which describes the dependence of the polymer conformations on the number of monomers.

Flory derived an expression of ν for polymer chains at dilute and semi-dilute concentrations in a good solvent [49], *i.e.*, a solvent in which the polymer can be easily dissolved, which was later generalised by Fisher [50]:

$$\nu = \frac{3}{2 + d}, (1 \leq d \leq 4). \quad (2.17)$$

The scaling exponent in good solvent depends solely on the dimensionality d . The prediction has been confirmed for one and two dimensions [51], where Flory's mean-field approach is exact. The most precise estimate for ν in three dimensions, $\nu = 0.588$ [52], was obtained by renormalization group theory and differs slightly from the Flory prediction $\nu = 3/5$. A more detailed analysis of the Flory formula (Eq. 2.17) can be found in Reference 53.

Semi-flexible chains

The chain models presented so far described *fully flexible* chains, *i.e.*, there were no restriction to the angle between two consecutive bonds. In reality, however, chemical details restrict the bond angle α between two linked monomers to a specific range. Consequently, the orientations of two neighbouring bonds \vec{b}_i and \vec{b}_{i+1} are correlated:

$$\langle \vec{b}_i \cdot \vec{b}_{i+1} \rangle \neq 0. \quad (2.18)$$

This correlation changes the local chain structure and violates the assumptions made in Section 2.2.1 for the derivation of Eq. 2.12. Locally, the chain appears to be more stretched out and less flexible. However, on a large scale, *i.e.*, for long chains, the correlations between more distant bond vectors decay

$$\langle \vec{b}_i \cdot \vec{b}_j \rangle = 0, \text{ if } |j - i| \gg 1, \quad (2.19)$$

and the chain appears to be fully flexible again. Such chains are called *semi-flexible chains*.

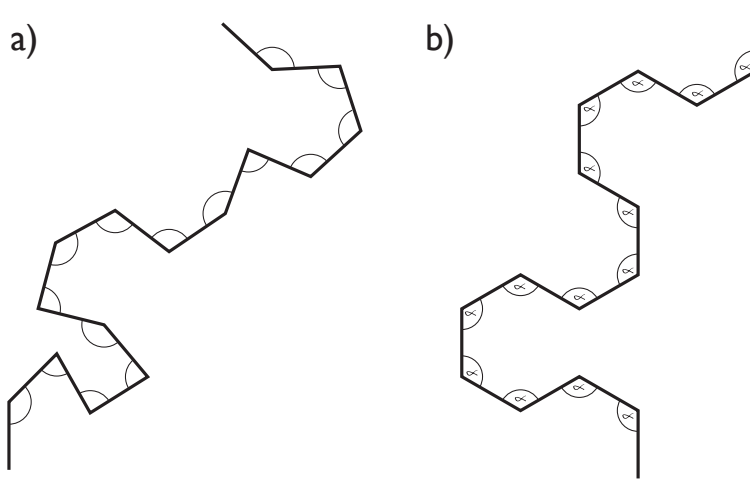


Figure 2.4: A fully flexible chain has unrestricted bond angles (a), unlike a semi-flexible chain, where chemical properties may demand a specific bond angle α (b).

It is possible to define a rescaled polymer chain with larger but again independent segments for every semi-flexible chain. The fixed bond length b is replaced by the distance between two uncorrelated bonds. This distance is called *Kuhn length* $b_K = nb$, where n is the distance between two bonds in which the correlation between the bond vectors goes to zero. Consequently, the number of such independent *Kuhn segments* is $N_K = N/n$. Using b_K and N_K the scaling behaviour of a semi-flexible chain can be described analogously to the scaling of flexible chains:

$$R_e = \langle R_e^2 \rangle^{1/2} = b_K N_K^\nu, \quad (2.20)$$

and

$$R_g = \langle R_g^2 \rangle^{1/2} = \frac{b_K}{\sqrt{6}} N_K^\nu. \quad (2.21)$$

A basic mechanical property related to the Kuhn length is the *persistence length* l_p that measures the stiffness of a polymer chain. Figure 2.5 shows two polymer chains with different persistence length. The left polymer has very short persistence length, making it more flexible and allowing it to change directions over relative short distances. The polymer with a larger persistence length behaves more like a flexible rod and remains straighter. The fully flexible models presented here describe chains that are longer than their persistence length and thus resemble more the first type of polymers.

Similar to the Kuhn length, the persistence length is defined as the length along the polymer chain after which the correlations between the bond vectors vanish. It can be shown that the average correlation function decays exponentially with the

2. Theoretical background on polyelectrolytes in free-solution



Figure 2.5: Two polymers with a different persistence length. The left polymer with a small persistence length is more flexible and changes direction over relatively short distances. The right polymer has a much larger persistence length, and therefore remains straighter.

distance $|i - j|$ between the bond vectors:

$$\langle \vec{b}_i \cdot \vec{b}_j \rangle = b^2 e^{-l_p/|i-j|}. \quad (2.22)$$

To give a visual impression, a piece of cooked spaghetti has a persistence length on the order of 10 cm, whereas double-stranded DNA has a persistence length of about 50 nanometers.

The persistence length is found to be one half the Kuhn length:

$$l_p = b_K/2. \quad (2.23)$$

2.3. Diffusion of polymer chains

The quantities R_e and R_g describe the spatial extension of polymer chains in the solvent medium, but do not characterise their motion through it. Even in an equilibrium situation in the absence of external forces the polymer chain is not at rest, but moves through the medium. This non-directed motion is called *diffusion* and is caused by thermal fluctuations of the solvent molecules colliding with the polymer, *cf. Brownian motion*.

2.3.1. Single-particle diffusion

Let's first look at a single particle embedded in a solvent. This particle is constantly subject to random collisions with the the fluid particles moving due to their thermal energy. Each collision imparts a small momentum to the solute particle, and the combined effect of all collisions is a macroscopic random motion of the particle, the *Brownian motion* or *diffusion*.

One can characterize the diffusion process analogously to the size of random polymer chain (*cf.* 2.2.1). While the first one is a random walk in time, the latter one is a random walk in space. The end-to-end distance of the polymer is replaced

by the mean-square displacement of the diffusing particle, the number of chain segments by the number of random moves of the particle which is proportional to the time t .

The equivalent of Equation 2.12 is the used to define the diffusion coefficient, or diffusivity, D :

$$\langle [\vec{r}(t) - \vec{r}(0)]^2 \rangle = 2dDt, \quad (2.24)$$

where $\vec{r}(0)$ and $\vec{r}(t)$ are the initial and final particle position, and the constant d is the dimensionality of the random walk, *e.g.*, $d = 3$ for the purpose of this thesis.

Equation 2.24 can be used to obtain the diffusion coefficient of a particle by measuring the mean-square-displacement:

$$D = \frac{\langle [\vec{r}(t) - \vec{r}(0)]^2 \rangle}{6t}. \quad (2.25)$$

Again, the angular brackets $\langle \dots \rangle$ denote an averaging over different random walks.

For a single particle, the diffusion coefficient D_0 is related to the resistance Γ_0 the particle experience from the solvent when it moves through it:

$$D_0 = \frac{k_B T}{\Gamma_0}, \quad (2.26)$$

with k_B being the Boltzmann constant and T the temperature. This ratio is also known as *Einstein relation*. The value of Γ_0 mainly depends on the size and the shape of the particle and on the type of interaction with the solvent. As the interaction with the solvent creates a frictional force on the particle, Γ_0 is also referred to as *friction coefficient*.

Only for very few cases a closed form for the friction coefficient can be given, *e.g.*, for a sphere with radius R in a homogeneous medium with viscosity η one obtains the *Stokes law*:

$$\Gamma_0 = 6\pi\eta R. \quad (2.27)$$

Combining Stokes law (2.27) with the Einstein relation (2.26) results in a simple equation for the diffusion coefficient of a spherical particle in a homogeneous solvent, also known as *Stokes-Einstein relation*:

$$D = \frac{k_B T}{6\pi\eta R}. \quad (2.28)$$

2.3.2. Chain diffusion

Similarly to the single-particle diffusion, one can define the single-chain diffusion of a polymer chain. As before, the corresponding diffusion coefficient D fulfils Einstein relation:

$$D(N) = \frac{k_B T}{\Gamma(N)}. \quad (2.29)$$

Here, both the diffusion and the friction coefficient are functions of the polymer length N . Again, the functional form of $\Gamma(N)$ strongly depends on the type of interactions that are taken into account. The two most important cases for polymer chains are described in the coming section.

2. Theoretical background on polyelectrolytes in free-solution

Rouse dynamics

The simplest expression for $\Gamma(N)$ is obtained when all long-range interactions between individual monomers are neglected. This regime is called *Rouse* regime [54]. The hydrodynamic interaction with the solvent is only treated locally, *i.e.*, each of the N monomers interacts as an independent single particle. Thus, the total friction coefficient is the sum of the individual friction coefficients:

$$\Gamma_{\text{R}}(N) = \sum_{i=1}^N \Gamma_i = N\Gamma_0. \quad (2.30)$$

Substituting Equation 2.30 into Equation 2.29 results in a $1/N$ -scaling for the diffusion coefficient of a polymer chain in the Rouse regime:

$$D_{\text{Rouse}}(N) = \frac{k_{\text{B}}T}{\Gamma_0} \frac{1}{N}. \quad (2.31)$$

Zimm dynamics

The hydrodynamic interactions between the monomers that are neglected in the Rouse regime only slowly decay with the distance r between the particles:

$$f_{\text{HI}}(r) \propto 1/r. \quad (2.32)$$

The hydrodynamic forces f_{HI} can be neglected for dense polymer melts, but are important in dilute solutions. In this regime, the polymer follows *Zimm dynamics* [55].

Every chain monomer displaces the surrounding solvent molecules, effectively dragging them along when it moves. From the outside, the polymer coil and the pervaded solvent move as one compact object through the surrounding solvent. The hydrodynamic radius of such an object formed by a real chain and the solvent is estimated as in Equation 2.16:

$$R(N) \approx bN^\nu. \quad (2.33)$$

The friction of the total object is given by Stokes law (Eq. 2.27):

$$\Gamma_{\text{Z}}(N) \approx 6\pi\eta R(N). \quad (2.34)$$

Using once again Stokes-Einstein relation (Eq. 2.28), the diffusion of a polymer chain in the Zimm model is obtained:

$$D_{\text{Z}}(N) \approx \frac{k_{\text{B}}T}{\Gamma_{\text{Z}}(N)} \approx \frac{k_{\text{B}}T}{6\pi\eta R(N)} \approx \frac{k_{\text{B}}T}{6\pi\eta bN^\nu}. \quad (2.35)$$

In other words, the diffusion coefficient D_{Z} of a polymer chain is expected to show a length-dependent scaling with $N^{-\nu}$.

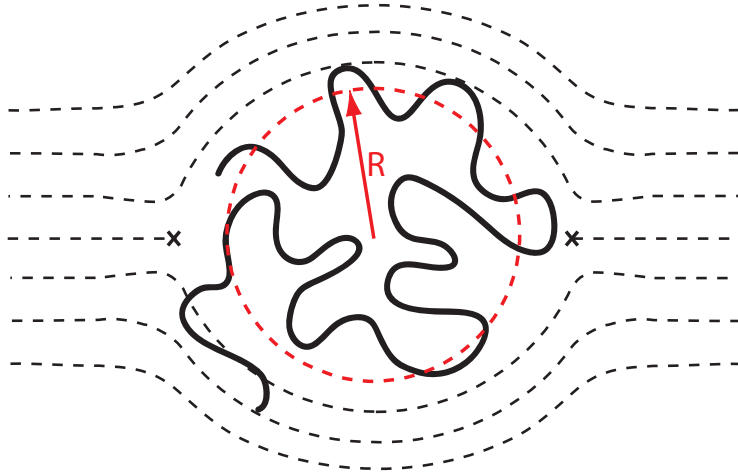


Figure 2.6: The Zimm model assumes that the moving polymer chain drags along the surrounding solvent, forming a compact object with radius R that moves through the medium. The hydrodynamic flow through the polymer is blocked (schematically displayed by the broken flow lines).

A more detailed analysis is offered by Kirkwood-Zimm theory, which is reviewed nicely in Reference 56. The hydrodynamic interactions between the chain monomers are taken into account via the Oseen tensor, yielding the following formula for the diffusion coefficient originally suggested by Kirkwood and Riseman [57]:

$$D_{\text{KZ}}(N) = \frac{D_0}{N} + \frac{k_{\text{B}}T}{6\pi\eta} \left\langle \frac{1}{R_{\text{h}}} \right\rangle, \quad (2.36)$$

with D_0 being the monomer diffusion coefficient and R_{h} being the so-called *hydrodynamic radius* defining the effective size of the polymer in the solvent. The hydrodynamic radius is given by

$$\left\langle \frac{1}{R_{\text{h}}} \right\rangle = \frac{1}{N} \sum_{i \neq j} \left\langle \frac{1}{\|\vec{r}_i - \vec{r}_j\|} \right\rangle. \quad (2.37)$$

Here, \vec{r}_i the position of the i -th monomer, and \vec{r}_{cm} the center of mass of the polyelectrolyte chain. The angular brackets $\langle \dots \rangle$ indicate an ensemble average.

For large N the average value for R_{h} is expected to scale with N^ν , like the other measures for the polymer size. Within this limit, the Zimm diffusion D_{Z} and the Kirkwood-Zimm diffusion D_{KZ} agree up to the monomer diffusion term, which can be neglected for long chains.

2.4. Polyelectrolytes

Polyelectrolytes are polymers whose monomers carry an electrolyte group which dissociates in water, leaving the monomer with an electric charge. Additionally, an oppositely charged counterion is released into the solvent. The charged nature of polyelectrolytes plays a fundamental part in determining their dynamic and static behaviour, which differs from those of their uncharged counterparts.

2.4.1. Chain conformations

The presence of charges along the polyelectrolyte chain causes a repulsion between the individual monomers, which leads to an intrinsic stiffness of the polyelectrolyte chain. Even an otherwise fully flexible chain has a non-zero persistence length due to the electrostatics.

The long-ranged electrostatic interactions influence the static chain properties, especially the chain conformation. For a polyelectrolyte in (infinite) dilution, neglecting the influence of the counterions (see Section 2.4.2), the size-dependence on the number of monomers can be estimated as follows.

The Hamiltonian of a polyelectrolyte chain is:

$$H = H_0 + \frac{1}{2}k_B T \sum_{i=1}^N \sum_{j \neq i} \frac{l_B}{|\vec{r}_i - \vec{r}_j|}. \quad (2.38)$$

Here, H_0 is the energy of the neutral polymer chain. The double summation over all monopairs accounts for the electrostatic interaction energy, with l_B being the Bjerrum length, which characterizes the strength of electrostatic interactions in the solvent (see Section 2.4.2).

The energy contribution of the neutral polymer, H_0 , contains all terms describing the chemical nature of the polymer and short range excluded volume interactions. In the simplest case of a Gaussian ideal chain, one obtains:

$$H_0 = \frac{3k_B T}{2b^2} \sum_{i=1}^N (\vec{r}_{i+1} - \vec{r}_i)^2. \quad (2.39)$$

The total energy can be express by the so-called *Flory free energy* of the polyelectrolyte in dependence of its size R , neglecting all prefactors of the order 1 [58]:

$$E_{\text{Flory}} = k_B T \left(\frac{R^2}{Nb^2} + \frac{N^2 l_B}{R} \right), \quad (2.40)$$

which after minimalization with respect to R yields the equilibrium size of the polyelectrolyte chain

$$R \propto N (l_B b^2)^{1/3}. \quad (2.41)$$

In other words, the electrostatic repulsion between the monomers leads to a swelling of the polyelectrolyte and to an extended conformation with a scaling exponent $\nu = 1$, *i.e.*, all static chain properties scale with the number of monomers:

$$R_{e,g,h} \propto N^1. \quad (2.42)$$

As a reminder, without charges ν is the Flory exponent, *i.e.*, $\nu \approx 0.588$.

However, this derivation is only applicable in the absence of electrostatic screening by the counterions which will be detailed in the following section.

2.4.2. Counterions

After looking at the chain conformations, we now take a look at the counterion distribution around the polyelectrolyte chains. The dissociated counterions are attracted to the charged polyelectrolyte by long-ranged Coulomb interactions. This attraction leads to the formation of a typically loosely bound *counterion cloud* around the polyelectrolyte. Nevertheless, these counterions strongly influence the polyelectrolyte conformation and its static and dynamic properties. The major parts of this thesis are devoted to the in-depth analysis of the complex interaction between polyelectrolyte and counterions mediated by the electrostatic and hydrodynamic interactions.

Counterion condensation

It is observed that strongly charged polyelectrolytes permanently attract some of the released counterions and effectively reduce their line charge density. This phenomenon was predicted by Onsager and later on described by Manning and Oosawa under the term *counterion condensation* [59, 60]. This topic has been discussed from varying viewpoints (see [61, 62] and the references therein).

The attraction of the counterions is not based on chemical bonding, but can be explained by the system's desire to minimize the free energy resulting from a competition between electrostatic energy and entropy:

$$\Delta F = \Delta E - k_B T \Delta S \quad (2.43)$$

The most common derivation, shown in Figure 2.7, uses the electrostatic potential created by an infinite stiff rod with a line-charge density equal to

$$\lambda = e/b, \quad (2.44)$$

where b is the spacing of the charged monomers of the polyelectrolyte approximated by the stiff rod.

The electrostatic potential around the rod decays logarithmically with the distance to the rod, more specifically, the energy difference for a counterion between an arbitrary point R and a point r , which marks the distance of closest approach to the rod, is given by:

$$\Delta E \sim e \frac{\lambda}{2\pi\epsilon} \ln \frac{R}{r}. \quad (2.45)$$

2. Theoretical background on polyelectrolytes in free-solution

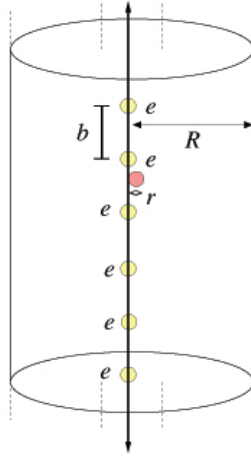


Figure 2.7: Scheme to motivate the counterion condensation phenomena based on the competition between electrostatic energy and entropy. The linear rod is modelled by a series of discrete charges e that have a linear separation of b . The counterion can move freely around the rod, but only approach it up to a minimal distance r .

On the other hand, the entropy is proportional to the volume accessible to the counterion, *i.e.*, a confinement close to the charge reduces the entropy:

$$\Delta S \sim \ln \frac{V_R}{V_r} \approx 2 \ln \frac{R}{r}. \quad (2.46)$$

Substituting Equations 2.45 and 2.46 into Equation 2.43 yields an approximation for the free energy of a counterion in dependence on its position R :

$$\Delta F \sim \left(\frac{l_B}{b} - 1 \right) 2k_B T \ln \frac{R}{r}. \quad (2.47)$$

Consequently, the distribution of counterions around highly charged rodlike polyelectrolytes can be described in terms of the Manning parameter

$$\xi = l_B/b, \quad (2.48)$$

where b is the distance between charges along the backbone of the polyelectrolyte, *i.e.*, the inverse line charge density, and l_B is the Bjerrum length

$$l_B = \frac{e_0^2}{4\pi\epsilon_0\epsilon_r k_B T}, \quad (2.49)$$

which represents the distance at which two unit charges experience an electrostatic potential that is equal to the thermal energy $k_B T$. Here, k_B is the Boltzmann constant, and e_0 the elementary charge. The Bjerrum length defines the length

scale for electrostatic interactions and depends on the investigated system, *e.g.*, for water at room temperature $l_B \approx 7.1\text{\AA}$.

For $\xi < 1$, the system is entropy dominated, *i.e.*, the counterions try to maximize the accessible volume. On the other hand, for $\xi > 1$, the system is energy dominated, which means that the electrostatic interactions makes it more favourable for a fraction of counterions to always be in the vicinity of the polyelectrolyte. These fraction of ions are the so-called *condensed counterions*.

In this study highly charged polyelectrolytes with $\xi > 1$ are investigated. The condensed counterions reduce the effective charge of the created polyelectrolyte-counterion compound. The theory predicts the fraction of those condensed counterions to be

$$f_{\text{CI}} = 1 - \frac{1}{\xi}, \quad (2.50)$$

and thus the total number N_{CI} is

$$N_{\text{CI}} = (1 - 1/\xi) N. \quad (2.51)$$

The counterion condensation has also been investigated by mean-field Poisson-Boltzmann approaches and, for the systems studied in this thesis, similar results are obtained [63–65].

2.4.3. Electrostatic screening

The presence of counterions in the vicinity of the polyelectrolyte has an important effect on it, as the electrostatic interactions between the chain monomers are partly screened.

To derive an expression for this screening, one can start out with the Poisson equation defining electrostatics for a system of positive and negative unit charges:

$$\nabla^2 \psi(\vec{r}) = -\frac{e}{\epsilon} \left(n^{(+)}(\vec{r}) - n^{(-)}(\vec{r}) \right). \quad (2.52)$$

Here, $n^{(+/-)}(\vec{r})$ is the density of positive and negative charges at position \vec{r} .

The electrochemical potential of each ion is

$$\mu^{(+/-)} = e\psi + k_B T \ln n^{(+/-)}, \quad (2.53)$$

from which one obtains the Boltzmann expression for the densities:

$$n^{(+/-)} = n_0^{(+/-)} e^{(-/+)\psi/k_B T}. \quad (2.54)$$

Combining Equations 2.52 and 2.54 yields the *Poisson-Boltzmann equation*:

$$\nabla^2 \psi(\vec{r}) = -\frac{e}{\epsilon} \left(n_0^{(+)} e^{-\psi/k_B T} - n_0^{(-)} e^{+\psi/k_B T} \right), \quad (2.55)$$

and for a simple electrolyte of monovalent salt, where $n_0 = n_0^{(+)} = n_0^{(-)}$, this can be rewritten as

$$\nabla^2 \psi(\vec{r}) = \frac{2e}{\epsilon} n_0 \sinh(\psi/k_B T). \quad (2.56)$$

2. Theoretical background on polyelectrolytes in free-solution

The linearization of the Poisson-Boltzmann equation leads to the *Debye-Hückel approximation*:

$$\nabla^2\psi(\vec{r}) = 8\pi l_B n_0 \psi(\vec{r}) = \lambda_D^{-2}\psi(\vec{r}) = \kappa^2\psi(\vec{r}), \quad (2.57)$$

which has an exponential solution for the electrostatic potential:

$$\psi(\vec{r}) = Ae^{-\kappa r}, \quad (2.58)$$

where κ is called the screening parameter, and λ_D is called the *Debye-Hückel screening length*, or *Debye length* for short:

$$\kappa^2 = \lambda_D^{-2} = 8\pi l_B n_0. \quad (2.59)$$

According to *Debye-Hückel* theory, the electrostatic interaction energy is reduced due to the presence of additional neutralizing charges in the solution:

$$U_{\text{DH}}(r) = U_{\text{Coulomb}}(r)e^{-\kappa r}. \quad (2.60)$$

For a solution containing the polyelectrolyte and its counterions, as well as additional salt, the Debye screening parameter has to be adjusted and depends on the concentration of the counterions c_{CI} and of the (monovalent) salt c_{S} :

$$\kappa^2 = 4\pi l_B (c_{\text{CI}} + 2c_{\text{S}}). \quad (2.61)$$

For example, at physiological conditions (inside the human body) the salt concentration is $c_{\text{S}} \approx 0.1\text{M}$, which leads to $\lambda_D \approx 1\text{nm}$. In other words, although the Coulombic interactions are long-ranged, in physiological conditions they are highly screened above length scales of a few nanometers.

The precise influence of the electrostatic screening on the static and dynamic properties will be investigated in this thesis (Chapters 4 and 5). Likewise, the related effect of *hydrodynamic screening* is the topic of Chapter 6.

Screening and polyelectrolyte conformations

The electrostatic screening effectively neutralises the electrostatic interactions on long length scales, *i.e.*, long polyelectrolyte chains are expected to show a similar scaling behaviour as uncharged polymer chains. Thus, the scaling exponent ν will asymptotically approach the Flory value for uncharged chains. This transition is faster the higher the electrostatic screening is, *i.e.*, the shorter the Debye length is.

For short polyelectrolyte chains, the influence of electrostatic interactions remains important. Most importantly, the effective persistence length has two contributions:

$$l_{\text{P,eff}} = l_{\text{P,0}} + l_{\text{P,ES}}, \quad (2.62)$$

where $l_{\text{P,0}}$ is the intrinsic persistence length of the polyelectrolyte and $l_{\text{P,OSF}}$ is the additional contribution due to electrostatic interactions. For a fully flexible polyelectrolyte $l_{\text{P,0}}$ vanishes, but $l_{\text{P,ES}}$ remains finite [66, 67]:

$$l_{\text{P,ES}} = \frac{l_B}{4b^2\kappa^2}. \quad (2.63)$$

The effective persistence length $l_{P,\text{eff}}$ has to be used when calculating the Kuhn segments length for a polyelectrolyte in solution.

2.5. Electrophoresis of polyelectrolytes

The charged nature of polyelectrolytes allows their manipulation by electric fields. During *electrophoresis* charged particles are moved through a medium by applying an external electric field. Electrophoresis has many variants and numerous applications, one of which is the separation of polyelectrolytes by length. For detailed reviews on the various current techniques see References 68–71.

2.5.1. Free-solution electrophoresis

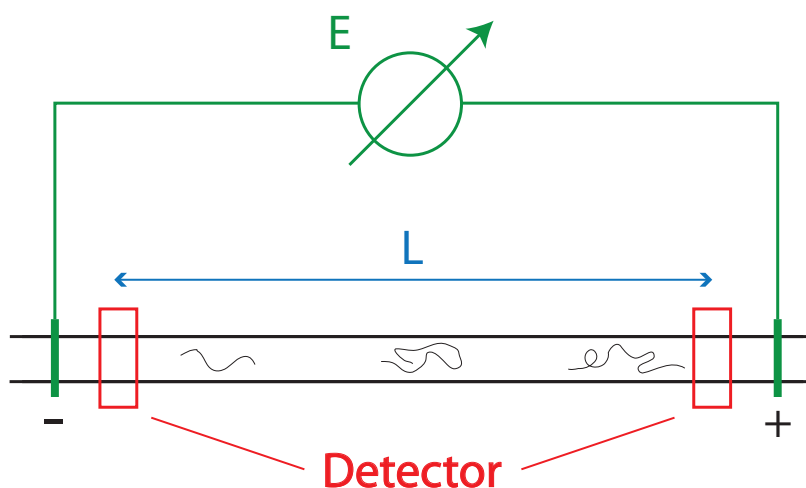


Figure 2.8: Electrophoresis of polyelectrolytes by capillary free-solution electrophoresis: the polyelectrolytes are driven by an external electric field E and the detectors measure the time t that is needed to travel along length L inside the capillary.

The method investigated in detail in this thesis is called *capillary electrophoresis*, displayed in Figure 2.8 [28, 32, 72]. The polyelectrolyte is dissolved in an aqueous solution and driven through a narrow capillary by an external DC electric field with field strength E . In contrast to the widely used method of *gel electrophoresis*, no sieving matrix is used in this technique, which is why it is also named *free-solution electrophoresis*. A detector measures the time t the polyelectrolyte needs to travel the known length L of the capillary.⁶ From this data the *electrophoretic mobility* μ

⁶Usually, UV absorbance or fluorescence detection cells are used.

2. Theoretical background on polyelectrolytes in free-solution

is calculated:

$$\mu = \frac{L/t}{E} = \frac{v}{E}. \quad (2.64)$$

Commonly used silica capillaries have a diameter of $50\mu\text{m}$ and a detector length of 30 cm , the applied electric field strengths are about 1000 V/cm . As the mobilities for standard polyelectrolytes such as polystyrene sulfonate (PSS) or DNA are of the order of $3\text{--}4 \cdot 10^{-4}\text{ cm}^2/\text{Vs}$, the elution times t for electrophoretic separation are only a couple of minutes. These short elution times represent the main advantage of the free-solution electrophoresis over other electrophoretic methods such as the predominantly used gel electrophoresis.

On the other hand, size separation of polyelectrolytes of different length is only possible if the mobility itself is a function of length. Unfortunately, this is not the case for all polyelectrolyte lengths. This is why, nowadays, gel electrophoresis still is the separation method of choice despite its speed disadvantage. Possible approaches to size separation without a sieving matrix are discussed in Chapter 8 and also in Ref. 71.

2.5.2. Current theoretical understanding of free-solution electrophoresis

In the scheme of the free-solution electrophoresis of flexible polyelectrolytes shown in Figure 2.9, one can see that the mobility is a function of length only for short chains. For long chains a constant value is approached so that separation of longer macromolecules by electrophoresis is not possible. This limit, called the *free draining* regime, is well described by analytical methods [37–39].

Local force picture

When the polyelectrolyte moves at a constant velocity, the system is in a steady state where the applied electrical force \vec{F}_E is exactly balanced by the frictional drag force \vec{F}_D the solvent exerts on the moving polyelectrolyte (see Fig. 2.10).

The electric force is given by

$$\vec{F}_E = Q_{\text{eff}}\vec{E}, \quad (2.65)$$

where Q_{eff} is the *effective charge* of the object. As mentioned in Section 2.4.2, the bare charge of the polyelectrolyte is reduced by the condensation of counterions. For long polyelectrolyte chains, Manning's theory predicts (*cf.* Equation 2.51):

$$Q_{\text{eff}} = (1/\xi)N. \quad (2.66)$$

In Chapter 6 this prediction for the long-chain limit will be revisited and several estimators for the effective charge of the polyelectrolyte-counterion complex will be introduced and analysed in detail.

The counteracting drag force exerted by the solvent is given in analogy to the Stokes friction by

$$\vec{F}_D = -\Gamma_{\text{eff}}\vec{v}. \quad (2.67)$$

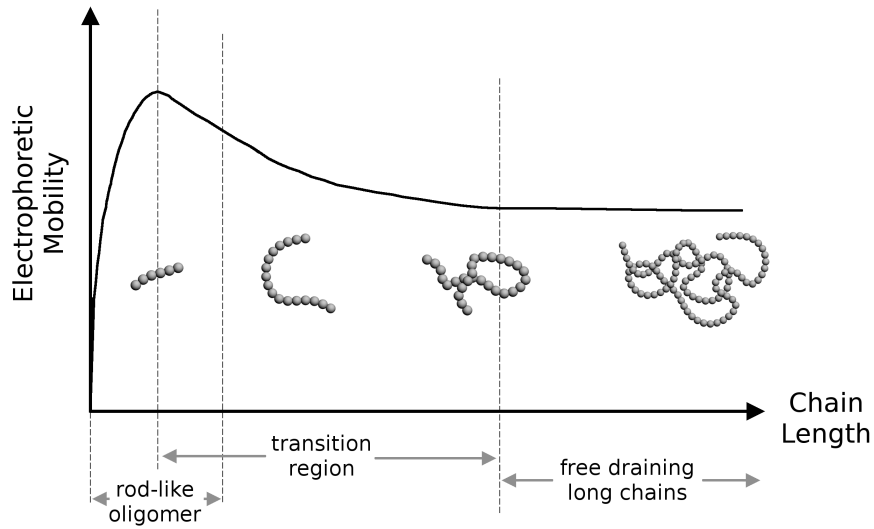


Figure 2.9: Scheme of the dependence of the electrophoretic mobility on the length of a flexible polyelectrolyte in free solution. Short rod-like oligomers show a monotonic increase in electrophoretic mobility with chain length. The mobility approaches a constant for long globular chains in the free draining regime. Between these two behaviours lies a transition region in which both counterion and hydrodynamic effects must be accounted for. This figure is based on experimental results presented in References 33, 73 and 74.

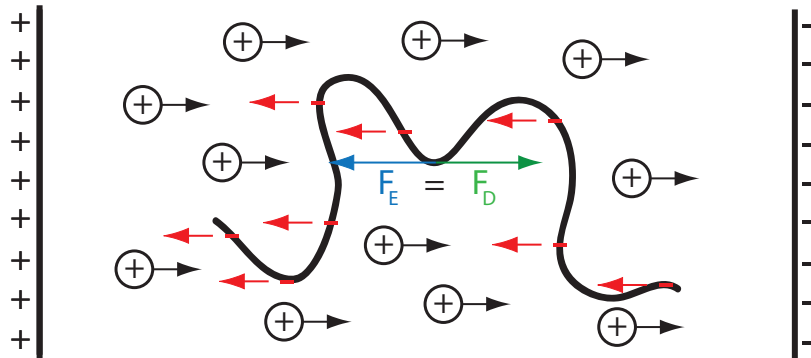


Figure 2.10: For a polyelectrolyte traveling at constant velocity v the electrical force \vec{F}_E and the solvent drag force \vec{F}_D are balanced.

2. Theoretical background on polyelectrolytes in free-solution

Here, Γ_{eff} is the *effective friction* of the polyelectrolyte. Using the scaling of the diffusion coefficient of a polymer (Eq. 2.35) and the Einstein relation (Eq. 2.26) one would obtain

$$\Gamma_{\text{eff}} \propto N^\nu, \quad (2.68)$$

where the scaling exponent $\nu \approx 0.6$ for long chains. This prediction derived from asymptotic scaling, however, does not seem to be applicable in the local picture, as will be shown now.

In the steady state, both forces have to be equal and one obtains:

$$Q_{\text{eff}}E = \Gamma_{\text{eff}}v, \quad (2.69)$$

from which immediately follows

$$\mu = \frac{v}{E} = \frac{Q_{\text{eff}}}{\Gamma_{\text{eff}}}. \quad (2.70)$$

This equation, together with the predictions in Equation 2.66 and 2.68, are not in agreement with the experimental observation of a constant mobility for long chains.

Free-draining picture

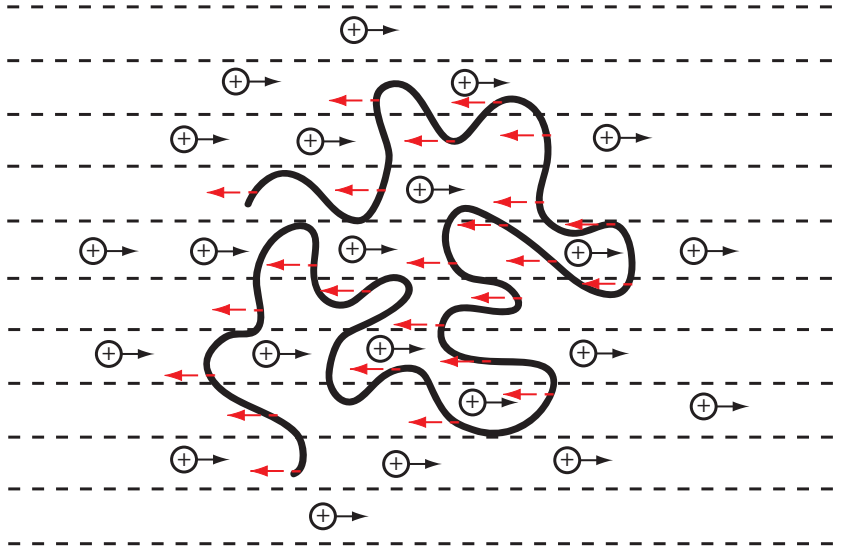


Figure 2.11: During electrophoresis, the polyelectrolyte coil is penetrated by oppositely charged counterions, thereby canceling out all long-range hydrodynamic interactions. The polyelectrolyte becomes “free-draining”.

For this reason, prediction 2.68 has been discarded and replaced by a new theory schematically displayed in Figure 2.11. The polyelectrolyte coil is no longer assumed

to travel as a compact spherical object with a given hydrodynamic radius. Instead it is penetrated by the counterions that, due to their opposite electrical charge, move into the opposite direction. Thereby, they drag along the surrounding solvent, allowing it to “drain” through the polyelectrolyte coil. Therefore, this picture is called the *free-draining picture*.

The counter-moving ions are assumed to destroy the long-range hydrodynamic interactions otherwise persistent in the polyelectrolyte coil. The interaction of the monomer with the solvent becomes a local interaction, much like in the Rouse regime for polymers (Section 2.3.2). The associated effective friction coefficient for long chains is estimated to be linearly dependent on the chain length

$$\Gamma_{\text{eff}} = \Gamma N, \quad (2.71)$$

which explains the constant mobility for long polyelectrolyte chains.

In Chapter 6, the effective friction of polyelectrolytes will be analysed in detail on the basis of the simulations of this thesis.

2.5.3. Short chain behaviour

The behaviour of short chains, exhibiting not only length dependence but a non-monotonic behaviour in the transition from oligomers to long flexible chains, is not adequately described by current theoretical approaches. To some extent this can be attributed to the simplifying assumptions made in those models regarding the interplay of the various interactions: the Coulomb interaction between the charged polyelectrolyte monomers and its counterions, the external electric field likewise acting on the charges, and the hydrodynamic interactions with the solvent.

To provide a fundamental understanding of the involved dynamics, the effects of these forces will be studied on a microscopic level, thereby taking into account full electrostatic as well as hydrodynamic interactions. By switching the hydrodynamic interactions “on” and “off” in different simulations, their role can be assessed in detail.

This thesis is dedicated to the in-depth study of this interesting aspect of soft matter physics.

2.6. Model requirements

Knowing the theoretical framework, the following model requirements can be formulated:

- Polyelectrolyte chains consists of charged monomers that are flexibly linked together by bonds;
- The solvation of polyelectrolytes releases oppositely charged counterions into the solvent that interact with the polyelectrolyte;

2. *Theoretical background on polyelectrolytes in free-solution*

- Without external forces, polyelectrolytes and ions diffuse freely through the system following the main conservation laws for momentum and energy;
- Electrostatic interactions between all charged particles in the system, including additional salt ions, have to be accounted for;
- All particles interact with the fluid and with each other via long-range hydrodynamic interactions.

In the following chapter, these requirements are translated to a coarse-grained polyelectrolyte model.

3. A coarse-grained model for polyelectrolytes

This chapter outlines the mesoscale simulation model employed to describe the behaviour of polyelectrolytes during free-solution electrophoresis. In order to be capable of dealing with experimentally relevant length scales, physical and chemical details have to be abstracted without losing focus on the important interplay of the relevant interactions. This work uses a coarse-grained molecular dynamics model to simulate the polyelectrolytes and surrounding ions. Furthermore, it emphasises the importance of the electrostatic interaction and the hydrodynamic interaction within a solvent by accounting for them explicitly on a mesoscopic level.

3.1. On physical and computational complexity

The accuracy with which a certain physical system is described is directly related to the complexity of the chosen theoretical model. The inclusion of further relevant features usually leads to a better agreement between model and real-world process.¹ On the other hand, each additional detail to be modelled increases the computational complexity and thus limits the system size that can be studied by the chosen method. This trade-off between accuracy and complexity is clearly seen in Figure 3.1.

The best model for a given problem includes all *relevant* physical processes to be as accurate as possible, but neglects *non-relevant* properties to be computational efficient. The differentiation between *relevant* and *non-relevant* properties is the stumbling block in developing of a realistic model.

In Section 2.6, it was pointed out that a realistic description of polyelectrolyte electrophoresis demands for taking into account the nature of discrete charges flexibly connected by the polyelectrolyte backbone, the electrostatic interactions with the freely moving counterions, and full hydrodynamic interactions with the surrounding solvent. This rules out continuum approaches as well as Brownian dynamics simulations, in which the solvent is only treated implicitly. For a good approximation, quantum mechanical and chemical details can safely be neglected. The system size requirements render fully atomistic molecular dynamic approaches infeasible, so that a mesoscopic approach is chosen in which the atomistic degrees of freedom of solute and solvent are coarse-grained as shown in Figure 3.2. The

¹However, not all physical interactions are relevant on all length-scales, *i.e.*, the model for a moving car can usually just do fine without quantum mechanics or electrostatics.

3. A coarse-grained model for polyelectrolytes

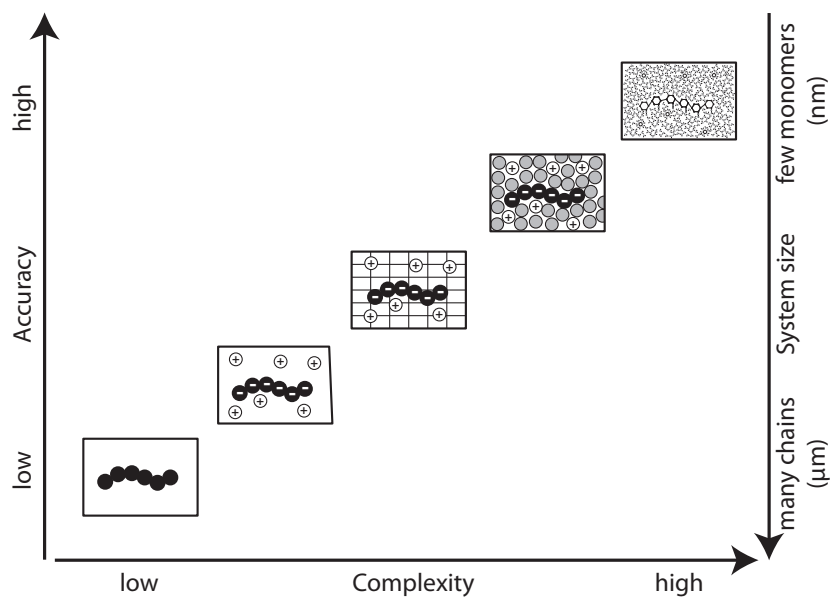


Figure 3.1: Increasing detail in the computational model increases the accuracy of the description but, at the same time, limits the system size tractable with available computation power.

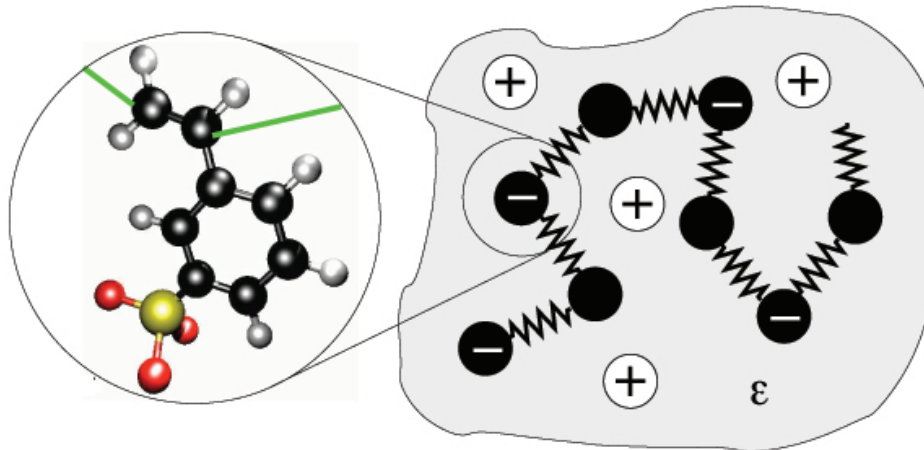


Figure 3.2: Example of the coarse-graining procedure used in this thesis: The chemical details of the monomer, in this example sulfonated polystyrene, are summarised by a single particle, carrying the electric charge, and the connectivity of the polyelectrolyte molecule is reflected in the links between the charged particles.

chemical details of the monomer, in this example sulfonated polystyrene, are summarised by a single particle, carrying the electric charge, and the connectivity of the polyelectrolyte molecule is reflected in the links between the charged particles. In the following sections, this coarse-grained model will be described in detail.

3.2. The model at a glance

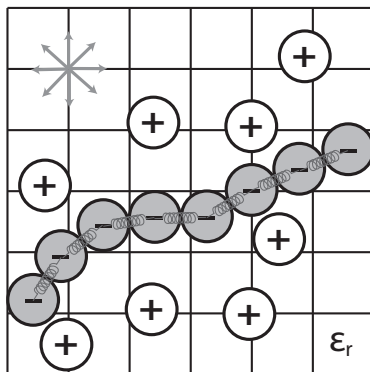


Figure 3.3: Scheme of the coarse-grained model to simulate polyelectrolyte electrophoresis. It is comprised of a bead-spring model for the polyelectrolyte and the counterions (Section 3.3), the handling of full electrostatic interactions within a dielectric continuum model (Section 3.4), and the treatment of hydrodynamic interactions with a mesoscopic fluid (Section 3.5).

The model features can be represented by the scheme in Figure 3.3. The polyelectrolyte is modelled by a set of impenetrable spheres, each of which represents an individual monomers, and that are connected to each other by springs. Likewise the dissociated counterions are modelled as impenetrable spheres. In this representation, atomistic degrees of freedom are combined into the microscopic degrees of freedom of the spheres. This approach is called *coarse-grained molecular dynamics* (Section 3.3). Monomers and ions carry electric charges by which they interact. The electrostatic interactions are influenced by the dielectric nature of the surrounding solvent. As the solvent particles are not explicitly included, a *continuum model* is used to allow for full electrostatics (Section 3.4). For the same reason, hydrodynamic interactions between the solute particles and the solvent are not described on a particle level. Instead a *mesoscopic fluid model* is applied that restores hydrodynamic interactions without having to track individual solvent particles (Section 3.5). All interactions are calculated in a periodic simulation box to recover bulk behaviour.

3. A coarse-grained model for polyelectrolytes

See Section 3.6 for an exhaustive list of parameters used to adapt this model to the physical systems studied in this work.

3.3. Coarse-grained molecular dynamics

The basic idea of (coarse-grained) molecular dynamics is straightforward and described in detail in standard text books on simulation methods, such as [75, 76]. Only the central aspects relevant to this work are reviewed in the following section.

3.3.1. Interaction potentials

All particles interact with one another via potentials that describe their physical nature.

The polyelectrolyte is comprised of N particles representing the individual monomers. A truncated, purely repulsive, Lennard-Jones or Weeks-Chandler-Anderson potential [77]

$$U_{\text{WCA}}(r_{ij}) = \begin{cases} 4\epsilon_{ij} \left[\left(\frac{\sigma_{ij}}{r_{ij}} \right)^{12} - \left(\frac{\sigma_{ij}}{r_{ij}} \right)^6 + \frac{1}{4} \right] & \text{for } r_{ij} < r_{\text{cut}} \\ 0 & \text{for } r_{ij} \geq r_{\text{cut}} \end{cases} \quad (3.1)$$

is acting between all particles in the system determining their size. Here, r_{ij} is the distance between two interacting particles i and j , σ_{ij} sets the length scale, and ϵ_{ij} the energy scale of the interaction. The physical particle size is directly related to the parameter σ_{ij} , which is therefore also seen as the effective size of the particles. In this study, the cutoff $r_{\text{cut}} = \sqrt[6]{2}\sigma_{ij}$ ensures a purely soft repulsive interaction.

The N monomers are connected to a chain by finitely extensible nonlinear elastic (FENE) bonds [78]

$$U_{\text{FENE}}(r_{ij}) = \frac{1}{2}kR^2 \ln \left(1 - \left(\frac{r_{ij}}{R} \right)^2 \right), \quad (3.2)$$

with stiffness k , maximum extension R , and r_{ij} again being the distance between the interacting monomers.

Together, these two potentials create a fully flexible self-avoiding polymer composed by N units. Stiff polymers with higher persistence length are modelled by including a bond angle potential

$$U_{\text{BA}}(\phi) = \frac{K}{2}(\phi - \phi_0)^2, \quad (3.3)$$

where the angle ϕ created by three connected particles is harmonically restored to the equilibrium angle ϕ_0 via an elastic constant K .

Unbound ions interact via a WCA potential, Eq. 3.1, that defines their physical size.

3.3.2. Velocity Verlet integration scheme

By taking the derivative of the potentials one obtains the forces between the particles. The sum of all the forces \vec{F}_T acting on a single particle from the interaction with the other particles and from external sources is calculated. Specifically, the contributions from electrostatic (Section 3.4) and hydrodynamic interactions (Section 3.5) are added to the total force \vec{F}_T prior to the integration of Newton's equation of motion:

$$\vec{F}_T = m\vec{a}. \quad (3.4)$$

Here, the *velocity Verlet scheme* is used to integrate Equation 3.4 and determine the particles' movement [79]. The time is discretised with a time step Δt and the following equations are used to update the particles' positions and velocities:

$$\vec{r}(t + \Delta t) = \vec{r}(t) + \vec{v}(t)\Delta t + \frac{1}{2}\vec{a}(t)\Delta t^2 \quad (3.5)$$

$$\vec{v}(t + \Delta t) = \vec{v}(t) + \frac{1}{2}[\vec{a}(t) + \vec{a}(t + \Delta t)] \quad (3.6)$$

The velocity Verlet algorithm is time-reversible and, more importantly, it conserves the size of any volume element in phase space. Also, it was shown that the algorithm shows no long time energy drift, which is especially important for simulating constant energy ensembles. Finally, the formulation in Equation 3.5 and 3.6 is exact up to $\mathcal{O}(\Delta t^4)$ in the positions and $\mathcal{O}(\Delta t^3)$ in the velocities.

Note that in the presented formulation all particles have the same unit mass, $m = 1$, which allows use of reduced forces. This is done without loss of generality, as, due to Newton's third law of action and reaction, the mass term cancels out if all particles have the same mass.

3.4. Continuum electrostatics

All particles in the system, *i.e.*, all N monomers and all ions, carry an electrical charge q_i that creates a non-bonded long-range interaction given by the Coulombic potential

$$U_C(r_{ij}) = \frac{1}{4\pi\epsilon_0} \frac{q_i q_j}{\epsilon_r r_{ij}}. \quad (3.7)$$

Here, q_i and q_j are the effective charges on each particle, ϵ_0 is the permittivity of free space, and ϵ_r is the dielectric constant of the medium. When an explicit polar solvent is used, including ϵ_r is not necessary. However, for simulations with either implicit or non-polar solvent models, as the ones used in this study, ϵ_r is an effective dielectric constant that includes the screening effects due to the medium (*e.g.*, $\epsilon_r = 80$ for water).

When the system is simulated at a certain temperature T by using a thermostat (see Section 3.5.1), Equation 3.7 is commonly reformulated as

$$\frac{1}{k_B T} U_C(r_{ij}) = l_B \frac{\hat{q}_i \hat{q}_j}{r_{ij}}, \quad (3.8)$$

3. A coarse-grained model for polyelectrolytes

using the Bjerrum length l_B as defined by Equation 2.49.

3.4.1. Electrostatics in periodic boundary conditions

In this study, as well as in many others, *periodic boundary conditions* are used to approach bulk system behaviour within the limit of currently available computer systems. The main simulation cell is extended infinitely in all dimensions via copies of itself. In this way, it can be avoided that particles which are close to the boundary of the simulation cell, “feel” a different environment than particles in the center of the cell.

Unfortunately, the calculation of the electrostatic interaction is complicated by the periodic boundary conditions as not only the contribution of the real charges but also of the periodically repeated images has to be taken into account. Therefore, equation 3.7 has to be rewritten as follows:

$$U_{\text{C,PBC}}(\vec{r}) = \frac{1}{4\pi\epsilon} \frac{1}{2} \sum_{i=1}^N \sum_{j=1}^N \sum_{\vec{n} \in \mathbb{Z}^3}^{\dagger} \frac{q_i q_j}{|\vec{r}_{ij} + \vec{n}L|}, \quad (3.9)$$

where $\vec{r}_{ij} = \vec{r}_i - \vec{r}_j$, the difference between the position of the charges. The sum over \vec{n} is taken over all simple cubic lattice points, $\vec{n} = (n_x L, n_y L, n_z L)$ with n_x , n_y , and n_z being integers. The \dagger indicates that the $i = j$ term must be omitted for $\vec{n} = 0$ to avoid to take into account the interaction of a particle with itself.²

The use of Eq. 3.9 in order to compute electrostatic interactions is known as *direct sum method*, which, although simple to implement, suffers from a major drawback: the sum over \vec{n} is an infinite series. This entails that when we want to evaluate the sum numerically we must perform a cutoff, *i.e.*, we assume that the contributions arising from larger \vec{n} values can be neglected. Unlike the WCA interaction (Eq. 3.1), which is extremely short ranged, the Coulombic interaction is long ranged and only decays very slowly ($\propto \frac{1}{r}$). While a cutoff value is appropriate in one dimension [75], the long-ranged contributions are important in two or three dimensions and a too low cutoff value incurs large numerical errors. For this reason, inclusion of electrostatic effects can be computationally expensive and many sophisticated techniques have been developed to address this particular problem (see [80] and the references therein).

3.4.2. Ewald sum

The electrostatic force in a periodic system can be more efficiently calculated using an *Ewald sum*, which involves calculating the short range interactions in real space and the long range contributions in Fourier space [81, 82].

²Equation 3.9 is only conditionally convergent in 3D. In other words, the value of the sum is not well defined unless one specifies the way we are going to sum up the terms (spheric, cubic, cylindric, etc.).

The algorithm is based on splitting the slowly convergent equation 3.9 into two series which can be computed much faster at a given accuracy by expressing $1/r$ as

$$\frac{1}{r} = \frac{f(r)}{r} - \frac{1-f(r)}{r}. \quad (3.10)$$

An usual choice is $f(r) = \operatorname{erfc}(\alpha r)$, where α is called the *Ewald splitting parameter*, which result in the *Ewald formula* for the energy of the main cell

$$U = U^{(r)} + U^{(k)} + U^{(\text{self})} + U^{(\text{dipolar})} \quad (3.11)$$

where $U^{(r)}$ is called the real space contribution, $U^{(k)}$ is the reciprocal space contribution, $U^{(\text{self})}$ is the self-energy, and $U^{(\text{dipolar})}$ accounts for the dipolar correction.

In the case of performing a spherical sum over the lattice vectors \vec{n} , the expressions for these contributions are given by

$$U^{(r)} = \frac{1}{2} \sum_i^N \sum_j^N \sum_{\vec{n} \in \mathbb{Z}^3} q_i q_j \frac{\operatorname{erfc}(\alpha |\vec{r}_{ij} + \vec{n}L|)}{|\vec{r}_{ij} + \vec{n}L|} \quad (3.12)$$

$$U^{(k)} = \frac{1}{2L^3} \sum_{\vec{k} \in \mathbb{K}^3, \vec{k} \neq 0} \frac{4\pi}{k^2} \exp(-k^2/4\alpha^2) \sum_i^N \sum_j^N q_i q_j \exp(-i\vec{k} \cdot \vec{r}_{ij}) \quad (3.13)$$

$$U^{(\text{self})} = -\frac{\alpha}{\sqrt{\pi}} \sum_i^N q_i^2 \quad (3.14)$$

$$U^{(\text{dipolar})} = \frac{2\pi}{(1+2\epsilon)L^3} \left(\sum_i^N q_i r_i \right)^2 \quad (3.15)$$

where $\mathbb{K}^3 = \{2\pi\vec{n}/L : \vec{n} \in \mathbb{Z}^3\}$.

In practice the sums for $U^{(r)}$ and $U^{(k)}$ are evaluated performing cutoffs given by r_{cut} and k_{cut} . Typical implementations, as the one we are going to use, assume the *minimum image convention*, i.e., $r_{\text{cut}} < L/2$ and therefore $\vec{n} = 0$ in the expression for $U^{(r)}$.

The advantage of the Ewald sum is two-fold. On the one hand, the convergence of Equations 3.12 and 3.13 is faster than the Equation 3.9 making it possible to define a more efficient cutoff for a given accuracy. On the other hand, it is possible to derive exact estimates for the error incurred by applying a certain cutoff.

3.4.3. Fast calculation of electrostatics

Although the Ewald sum method represents a substantial improvement with respect to the direct sum, in many cases it is not as fast as one would desire. This drawback is specially notorious when we are dealing with systems containing a large number of charged particles and is mainly due to the fact that the computer time in Ewald sums scales with the number of particles as $\mathcal{O}(N^2)$, or in the best versions as

3. A coarse-grained model for polyelectrolytes

$\mathcal{O}(N^{3/2})$. These scalings entail that the computer time grows very quickly with the number of particles.

The approach is efficiently sped up by the use of fast Fourier transformation (FFT) in commonly used algorithms: the so-called particle-particle-particle mesh (P3M) [83, 84], particle mesh Ewald (PME) [85], and smooth PME (SPME) [86] methods. See [87] for a review of the individual methods and a detailed comparison. Further interesting approaches to solve this problem are the (fast) multipole methods [88] and the local reaction field (LRF) method [89].

In this study, the P3M algorithm is used that scales like $\mathcal{O}(N \log(N)) \sim \mathcal{O}(N)$. Deserno *et al.* [90] derived error estimates that predict the achieved accuracy of the method based on the parameters chosen. This error estimates are used in an automated tuning routine that checks all parameter combinations that yield the desired accuracy α for the given system and selects the set that uses the least computation time.

3.5. Modelling the fluid

The potentials defined in Section 3.3.1 neglect any influence of the solvent in which the polyelectrolyte and the ions move. In the previous section, the dielectric constant ϵ_r was introduced to account for the polar characteristics of the solvent. In the following section, we will look at other system properties related to the immersion in a fluid and describe their realisation in simulations. Firstly, the thermalising properties of an *implicit fluid* are considered (Section 3.5.1), secondly, the *mesoscopic fluid model* is introduced, which is used in this study to account for long-range hydrodynamic interactions between the particles in solution (Section 3.5.2).

3.5.1. Implicit fluid model

In general, a fluid has two main effects on the solute: i) a frictional force opposing the particles' motion and ii) random kicks arising from collision with the individual solvent molecules. The later phenomenon is known as *Brownian motion*. Whereas the friction with the solvent dissipates energy from the particles, the kicks add energy to them.

A simple model that treats the fluid interactions implicitly is the *Langevin thermostat* [91]. Here, a modified version of the equation of motion (Eq. 3.4) is used, that contains two additional forces, a dissipative and a random one:

$$\vec{F}_T + \vec{F}_D + \vec{F}_R = m\vec{a}. \quad (3.16)$$

The dissipative force is defined similarly to the Stokes' friction an object immersed in a fluid experiences:

$$\vec{F}_D = -\Gamma_0 \vec{v}_i, \quad (3.17)$$

with \vec{v}_i being the particle velocity and Γ_0 the appropriately chosen friction coefficient. For example, for a sphere with radius R in a medium with viscosity η the friction coefficient would be equal to $\Gamma_0 = 6\pi\eta R$.

The random force

$$\vec{F}_R = \vec{\zeta}_i(t) \quad (3.18)$$

is taken as a Gaussian random variable $\vec{\zeta}_i(t)$ with

$$\langle \vec{\zeta}_i(t) \rangle = 0 \quad \text{and} \quad \langle \vec{\zeta}_i(t) \cdot \vec{\zeta}_j(t') \rangle = 6\Gamma_0 k_B T \delta_{ij} \delta(t - t'), \quad (3.19)$$

i.e., it is not correlated between the particles or in time.

The random noise defined in this way acts as heat bath that keeps the simulated system at a constant temperature T . Note that the variance of the random noise is correlated to the friction coefficient Γ_0 in order to fulfil *fluctuation-dissipation theorem* [92].

Both forces of the Langevin thermostat, \vec{F}_D and \vec{F}_R , are included in the the total force acting on each particle, \vec{F}_T , in the integration of Equation 3.4. As a technical point, it is to be remarked that the combination of the Langevin thermostat with the velocity Verlet integration introduces an error of order $\mathcal{O}(\Delta t)$ in the forces, and so the total error in the velocities and the positions are of order $\mathcal{O}(\Delta t^2)$ and $\mathcal{O}(\Delta t^3)$ respectively [93].

As the random noise is not correlated between particles (see Eq. 3.19), the relative momentum between solute particles is not conserved. This leads to a cancellation of all long-range hydrodynamic interactions mediated by the fluid. As such, one has to use another fluid model to study hydrodynamic effects on polyelectrolytes.

3.5.2. Mesoscopic fluid models

An alternative approach to include hydrodynamic interactions is to model an *explicit fluid* where fluid particles are interacting via a WCA potential (Eq. 3.1). This conceptually obvious approach is easy to implement and preserves long-range hydrodynamic interactions. In practise, however, as the trajectory of every fluid particle has to be calculated explicitly, much computing time is spent on details of the fluid which are often not of interest. For this reason, several modelling techniques to maintain the hydrodynamic interactions within the fluid while neglecting the costly computational details of the fluid motion have been developed. The description of the hydrodynamic effects in these approaches lies in between the use of an explicit description of fluid molecules and the solution to the continuous Navier-Stokes equations (Eq. 2.1). In particular, a clever use of conservation laws allows these methods to employ local algorithms to recover the solution to the hydrodynamic equations in the large-scale/long-time limit, bypassing at the same time the molecular detail of the fluid and thus reducing dramatically the computational cost of the simulation.

Nowadays, the most commonly used methods are Multiparticle Collision Dynamics (MPC) – also called Stochastic Rotation Dynamics (SRD) – [94–100], Dissipative Particle Dynamics (DPD) [101–105], and Lattice Boltzmann (LB) [106–110]. There are several recent publications reviewing the different mesoscopic fluid models: [111–113].

3. A coarse-grained model for polyelectrolytes

Comparison of mesoscopic fluid models

All of the above methods use a simple (but sufficient) model to describe fluid dynamics, and can also act as thermostats that define the local temperature when coupled to MD particles. As such, they are well suited to study the polyelectrolyte electrophoresis as they can dissipate the energy transferred to the system by the applied electric field.

Due to their conceptual differences, these methods use different types of parameters to describe the fluid, which results in a different suitability for specific problems. For example, while the fluid viscosity is directly accessible in LB methods, it becomes a combination of different parameters and can only be controlled indirectly in DPD [114, 115]. Similarly, while DPD and LB can only approximate the continuous-time dynamics of the fluid when the discrete time step is small, SRD is proven to yield correct long-time hydrodynamic interactions for any step size. However, SRD's transport properties depend explicitly on the chosen time step [116]. More differences between the methods arise if confined fluids or interactions with large obstacles or particles are studied. Here, the ability to treat different boundary conditions becomes important, which is covered in detail in the literature [95, 96, 117–121].

All three methods share a similar computational efficiency, and computation times depend mainly on the implementation, on the computer system, and also on the investigated system. However, the speedup over explicit fluid simulations can be a factor 20 or higher [122, 123].

This study uses the Lattice Boltzmann method that is briefly reviewed in the following section.

3.5.3. The Lattice Boltzmann method

The Lattice Boltzmann (LB) method is based on a solution of the discretised Boltzmann transport equation, which by means of a Chapman-Enskog expansion leads to the Navier-Stokes equation (Eq. 2.1) in the incompressible limit [107, 110].

The main quantities in the LB approach are the particle densities $n_i(\vec{r}, t)$ at each point \vec{r} on a spatially discrete grid at time t , rather than the fluid particles in the volume. It is an inherently statistical approach, where discrete velocities $\vec{c}_i(a/\tau)$ ($i = 1, \dots, b$) are associated to the particle densities $n_i(\vec{r}, t)$, with a being the grid spacing, τ the time step of the discretisation, and the \vec{c}_i vectors pointing towards the i th of b next neighbours on the grid. Each of the $n_i(\vec{r}, t)$ can be interpreted as the fraction of fluid that will move with the i -th discretised velocity at time t and position \vec{r} .

In this study the LB method was implemented on a D3Q18 lattice, *i.e.*, the particle distributions with velocity vectors \vec{c}_i pointing to the the 18th nearest neighbours on a cubic lattice in three dimensions are considered as illustrated in Figure 3.4.³

³The system described in Chapter 7 was also used to test a newer implementation using a D3Q19 lattice. No differences have been observed.

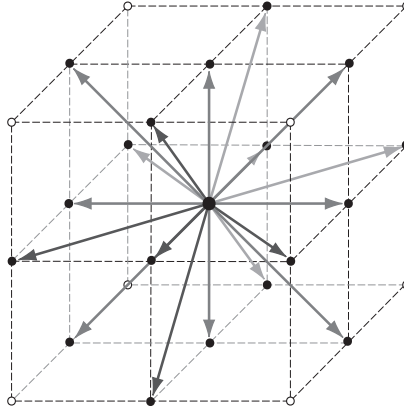


Figure 3.4: The 18 velocity vectors \vec{c}_i for a D3Q18 lattice. From the central grid point, the velocity vectors point towards all 18 nearest neighbours marked by filled circles.

The particle densities $n_i(\vec{r}, t)$ define the hydrodynamic quantities of interest, the mass density $\rho(\vec{r}, t)$, the fluid momentum $\vec{j}(\vec{r}, t)$, and the fluid velocity $\vec{u}(\vec{r}, t)$, as given by the following equations:

$$\rho(\vec{r}, t) = \sum_i n_i(\vec{r}, t) \quad (3.20)$$

$$\vec{j}(\vec{r}, t) = \sum_i n_i(\vec{r}, t) \vec{c}_i \quad (3.21)$$

$$\vec{u}(\vec{r}, t) = \vec{j}(\vec{r}, t) / \rho(\vec{r}, t). \quad (3.22)$$

The LB method consists of two steps, a *collision step* and a *streaming step*. During the collision step the particle densities at each lattice site are updated. In the streaming step, the updated particle densities are propagated over the grid according to the associated velocity vectors.

The evolution of $n_i(\vec{r}, t)$ in the collision step is described by the lattice Boltzmann equation:

$$n_i(\vec{r} + \vec{c}_i a, t + \tau) = n_i(\vec{r}, t) + \sum_{j=1}^b L_{ij} (n_j(\vec{r}, t) - n_i^{eq}(\rho, \vec{u})), \quad (3.23)$$

where the last term expresses the relaxation towards a local pseudo-equilibrium. The discretised Boltzmann equation provides a generic description for the time evolution of the particle densities, but there is freedom in the choice for the actual form of the collision integral L_{ij} . A common formulation is the Bhatnagar-Gross-Krook

3. A coarse-grained model for polyelectrolytes

approximation [124] with a diagonal $L_{ii} = \tau/\tau_r$, where τ_r is a phenomenological relaxation time. It prescribes the timescale for the relaxation towards the equilibrium density $n_i^{eq}(\rho, \vec{u})$, which can be written as

$$n_i^{eq}(\rho, \vec{u}) = \rho a^{c_i} \left(1 + \frac{\vec{u} \cdot \vec{c}_i}{c_s^2} + \frac{(\vec{u} \cdot \vec{c}_i)^2}{2c_s^4} - \frac{u^2}{2c_s^2} \right) \quad (3.24)$$

with c_s being the speed of sound.

However, in this study, following [108, 122], a general form for L_{ij} was used, where the matrix structure is derived from physical and numerical arguments. This entails a local pseudo-equilibrium density distribution $n_i^{eq}(\rho, \vec{u})$ of the following functional form:

$$n_i^{eq}(\rho, \vec{u}) = \rho(A_q + B_q(\vec{c}_i \cdot \vec{u}) + C_q u^2 + D_q(\vec{c}_i \cdot \vec{u})^2). \quad (3.25)$$

The coefficients A_q , B_q , C_q , and D_q depend on the chosen lattice and are determined in order to recover correct macroscopic hydrodynamic behaviour. One can show via Chapman-Enskog expansion⁴ that this model leads to the Navier-Stokes equations in the limit of small Knudsen and Mach numbers. From this, the relation between the non-trivial eigenvalue λ of L_{ij} and the kinematic viscosity ν follows:

$$\nu = -\frac{1}{6} \left(\frac{2}{\lambda} + 1 \right) \frac{a^2}{\tau}, \quad (3.26)$$

which can be used to specify the viscosity as an explicit input parameter for the LB method.

In order to thermalise the fluid under electrophoretic conditions, a stochastic term

$$n'_i(\vec{r}, t) = -D_q \sum_{\alpha\beta} \sigma'_{\alpha\beta} c_{i\alpha} c_{i\beta} \quad (3.27)$$

fulfilling fluctuation-dissipation relation is added to the lattice Boltzmann equation (3.23) [108]. It has recently been shown that this noise has to be applied to all non-conserved modes of the collision operator to prevent poor thermalisation on smaller length scales, and not only to the elements of the viscous stress tensor [125, 126].

Coupling LB to coarse-grained molecular dynamics

On the length and time scales important in polyelectrolyte electrophoresis, the physical observables do not depend on the microscopic details of the coupling between the LB fluid and the coarse-grained molecular dynamics particles, as long as it is assured that the hydrodynamic interactions within the fluid evolve on time scales

⁴The Chapman-Enskog expansion is essentially an asymptotic analysis in time and space with $t_1 = \epsilon t$ and $r_1 = \epsilon r$ followed by a Taylor expansion of n_i to second order in ϵ . Using that the conservation laws for mass and momentum must hold at every order in ϵ together with the substitution of the expansion of n_i into the Boltzmann equation 3.23 leads to the hydrodynamic equations when collecting terms in orders of ϵ .

faster than the diffusion time scale of the monomers. Therefore, it is not necessary to resolve the shape of the particles for the fluid, but they can instead be treated as point particles. This approach was originally suggested by Ahlrichs *et al.* [122].

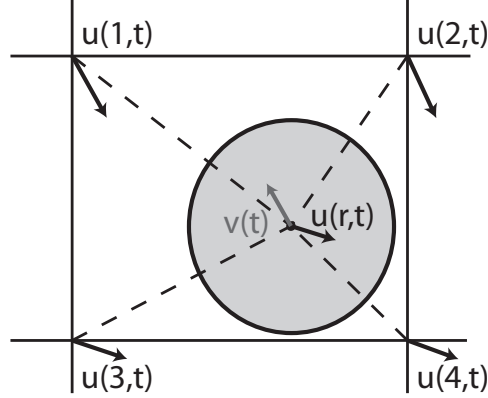


Figure 3.5: The coupling scheme between fluid and particles is based on the interpolation of the fluid velocity \vec{u} from the grid nodes marking the cell the particle is in to the actual position \vec{r} of the particle. This is done by linear interpolation. The difference between the actual particle velocity $\vec{v}(t)$ and the interpolated velocity $\vec{u}(\vec{r}, t)$ is used in the momentum exchange of Equations 3.28 and 3.29.

In analogy to the Stokes friction for a sphere in viscous fluid, *cf.* Section 3.5.1, the force on a particle exerted by the fluid is assumed to be proportional to the difference between the monomer velocity \vec{v} and the fluid velocity \vec{u} at the monomer's position

$$\vec{F}_D = -\Gamma_{\text{bare}} (\vec{v}(t) - \vec{u}(\vec{r}, t)). \quad (3.28)$$

Here, the friction coefficient Γ_{bare} determines the strength of the interaction between fluid and particles. In order to conserve total momentum of fluid and monomers, the opposite force has to be assigned to the fluid in the particles' cell fulfilling

$$-\vec{F}_D/a^3 = \frac{\Delta \vec{j}}{\Delta t} = \sum_i \Delta n_i(\vec{r}, t) \vec{c}_i \frac{\rho}{a^2 \tau \Delta t}. \quad (3.29)$$

As the fluid velocity \vec{u} is only defined at the grid sites, $\vec{u}(\vec{r}, t)$ has to be interpolated to the particle position. This is done by a simple linear interpolation with the neighbouring grid nodes, as indicated in Figure 3.5.

Additionally to the dissipative coupling, a stochastic random force is added to model the thermalising properties of the fluid:

$$\vec{F}_R = \vec{\zeta}_i(t). \quad (3.30)$$

3. A coarse-grained model for polyelectrolytes

As for the implicit fluid model, *cf.* Section 3.5.1, $\vec{\zeta}_i(t)$ has to fulfill the following equations:

$$\langle \vec{\zeta}_i(t) \rangle = 0 \quad \text{and} \quad \langle \vec{\zeta}_i(t) \cdot \vec{\zeta}_j(t') \rangle = 6\Gamma_{\text{bare}}k_{\text{B}}T\delta_{ij}\delta(t-t'). \quad (3.31)$$

Again, the added momentum has to be transferred to the fluid following Eq. 3.29.

Both \vec{F}_{D} and \vec{F}_{R} are added to the total force \vec{F}_{T} before integrating Eq. 3.4 for the particles. At the same time, the fluid is updated according to the LB method. The momentum exchange between particles and fluid correctly reproduces long-range hydrodynamic interactions at relatively low computation costs compared to an explicit fluid. In fact, as mentioned before, it has been shown that the relative speedup can be a factor 20 or higher [122, 123].

Technical remarks on LB

The implementation used in this study allows to specify the fluid and the coupling via five parameters:

- the average fluid mass density ρ ,
- the kinematic viscosity ν ,
- the grid spacing a ,
- the time step τ used for the fluid evolution,
- and the coupling parameter Γ_{bare} .

Whereas the first two parameters define the physical properties of the fluid, and the following two parameters detail the numerical discretisation, the coupling parameter has no predefined meaning. However, it can be related to the single particle friction coefficient Γ_0 of the implicit fluid model (Section 3.5.1) via

$$\frac{1}{\Gamma_0} = \frac{1}{\Gamma_{\text{bare}}} + \frac{1}{g\nu\rho a}, \quad (3.32)$$

where g is numeric constant depending on the details of the lattice geometry and of the averaging procedure. Here, $g \approx 25$.

As the value of Γ_{bare} is a priori not defined by the physical nature of the problem, it was chosen in such a way that the single particle diffusion coefficient D_0 (Section 2.3.1) within the LB fluid corresponds to that obtained in simulations using an explicit fluid consisting of soft WCA spheres [56].

Finally, it remains to be pointed out that the parameters specifying the length and time scales of the molecular dynamics simulation, σ_{ij} and Δt , and of the LB fluid, a and τ , can be chosen independently of one another. However, as the grid spacing a defines the length scale on which hydrodynamic interactions are correctly resolved, it should be similar or smaller than σ_{ij} . On the other hand, one can confirm easily that τ can be chosen up to 5-times larger than Δt without a significant loss in

accuracy for the systems investigated in this work. As the updating of fluid is the most time-consuming step during simulation, this provides a significant speed-up in computation time.

3.6. System parameters

The generic model for polyelectrolytes in solution outlined above can be specialised to match the physical properties of a target system via the parameters listed in Table 3.1.

Unless indicated, all simulation parameters are given in reduced units in the energy scale $k_B T$, the mass scale m_0 and the relevant length scale σ_0 that is used to match the model to a specific polyelectrolyte. If not specified differently in the following chapters, the values indicated in this table were used throughout this study.

Note that the size L of the periodic simulation box is indirectly defined by the total number of polyelectrolyte monomers in the system and their concentration. In this way the properties of chains of different length N can be compared at the same monomer concentration c_M since this is the situation encountered in the experiments.

3.6.1. Data sampling

In order to obtain data with a sufficient accuracy, all averaging has to be done over large enough sample sizes. In order to reduce statistical errors but at the same time keeping the computational effort at a minimum, several approaches are combined in this study.

The focus of this study are equilibrium properties. To ensure that the system has relaxed from the random initial position to the equilibrium, a sufficient number of equilibration time steps (ET) are executed before the sampling process begins. It has been identified, that 10^6 MD steps are guaranteeing a well relaxed system state.

To eliminate possible finite size effects, the number of chains of the same length, n_c , is varied from 1 to 8. In the latter case, 8 chains (and the associated counterions) are simulated at the same time in a box with a doubled box length to keep the monomer concentration at the chosen value. In addition to reducing the finite size effects, this approach also increases the sample size available for averaging.

The data is sampled from trajectories of 10^7 sampling time steps (ST). To increase the number of statistically independent samples, up to 10 separate runs for the same parameter set are simulated and combined during the averaging procedure.

The obtained time-series are analysed using auto-correlation functions to estimate the statistical errors as detailed in Reference 127.

3. A coarse-grained model for polyelectrolytes

		Description	Used values
General	N	length of the PE in monomers	1 ... 256
	n_c	number of chains	1 or 8
	c_M	concentration of the PE monomers	1 ... 100mM
	c_{CI}	concentration of the counterions	1 ... 100mM
	c_S	concentration of additional salt	0 ... 1M
	σ_0	length scale of the system	2.5 ... 4.2Å
	$k_B T$	energy scale of the system	1.0
	m_0	mass scale of the system	1.0
Interaction potentials (Section 3.3.1)	σ_{ij}	length scale of the WCA potential	1.0
	ϵ_{ij}	energy scale of the WCA potential	0.25
	k	spring constant for the FENE springs connecting the PE monomers	30.0
	R	maximal extension of the FENE springs	1.5
	K	harmonic constant of the bond potential to increase the persistence length	0 ... 30.0
	ϕ_0	equilibrium angle of the bond potential	0°
	Δt	time step for the integration of motion	0.01
Electrostatics (Section 3.4)	q_i	charges of the particles	1.0
	l_B	Bjerrum length ($\approx 7.1\text{Å}/\sigma_0$)	1.7 ... 3.4
	α	accuracy requirement for electrostatics	$1e^{-4}$
Hydro- dynamics (Section 3.5)	ρ	density of the mesoscopic LB fluid	0.864
	ν	kinematic viscosity	3.0
	a	grid spacing of the lattice	1.0
	Γ_{bare}	coupling constant for the particles	20.0
	τ	time step for the update of the fluid	0.01 ... 0.05
Sampling (Section 3.6.1)	ET	equilibration time steps	10^6
	ST	sampling time steps	10^7
	IS	independent sample runs	up to 10

Table 3.1: Summary of the parameters employed to adapt the generic polyelectrolyte model to a specific system, including the range of values used in this study. Parameters without physical units are specified in reduced units.

3.6.2. Mapping between reduced and real-world units

The mapping between reduced simulation units and real-world units often is a source of confusion for people not familiar with coarse-grained simulation techniques. The following three questions and their answers explain the most significant relations.

What is the real-world temperature of the system?

As specified in Table 3.1 the system is simulated at a thermal energy of $k_B T = 1.0$. But this only defines the energy scale and not a real-world temperature. For all purposes of this study, the temperature is *chosen* to be room temperature, *i.e.*, 300K. As the interaction potentials between the particles are artificial, no real world matching exists for these parameters and it is sufficient to express them in multiples of the thermal energy $k_B T$, distinguishing between easily excitable and hard excitable modes.

What is the size of the polyelectrolyte monomers?

The relative sizes of all particles are given by the interaction potentials. We find the average distance between two neighbouring chain monomers in this model to be approximately 0.9, whereas the distance of closest approach between two not connected monomers is 1.0. The length-scale σ_0 relates the system dimensions to the real-world. *e.g.*, for modelling polystyrene sulfonate (PSS) with a monomer distance of 2.5Å in real-world units σ_0 is chosen to be 2.78Å.

The parameter σ_0 is furthermore important in mapping the particle densities in the simulation box to the concentrations c_M , c_{CI} and c_S , as well as for the electrostatic interactions by entering the rescaled Bjerrum length $l_B = 7.1\text{Å}/\sigma_0$.

How large is the applied electric field?

Physical quantities with non-trivial dependence on the system parameter can be transformed from reduced units to real-world units and back by dimensional analysis. As an example, we look at the electric field strength \hat{E} of an external field applied during electrophoresis⁵. The field strength is measured in V/m:

$$\left[\hat{E} \right] = \frac{\text{V}}{\text{m}} = \frac{\text{VC}}{\text{mC}} = \frac{\text{J}}{\text{mC}}. \quad (3.33)$$

From this it becomes apparent that the electric field can be expressed in units of energy (J), distance (m) and charge (C). When using reduced units, *i.e.*, all scales are represented in terms of the corresponding parameter, just a dimensionless electric field E remains:

$$\hat{E} = E \frac{k_B T}{\sigma_0 e_0}. \quad (3.34)$$

⁵Here, the hat denotes real-world units.

3. A coarse-grained model for polyelectrolytes

The conversion factor can be calculated by substituting the real-world values for the simulated system, *e.g.*, for $T = 300\text{K}$, $\sigma_0 = 2.78\text{\AA}$, and $e_0 = 1.6 \cdot 10^{-19}\text{C}$:

$$\hat{E} \approx E \cdot 10^8 \text{V/m.} \quad (3.35)$$

Commonly used fields in electrophoresis are of the order of 1 kV/cm or 10^5V/m corresponding to a simulation field of $E = 0.001$.

3.7. Implementation

The model was implemented and simulated using the ESPResSo software package [128], which was specifically designed with the flexibility in mind to be applicable to different soft matter systems. Details about ESPResSo and the implementation can be found in the program's documentation and on the corresponding website⁶.

In ESPResSo every system to be simulated is defined by a script using predefined additional commands within the scripting language *tcl*⁷. The script also controls the actual simulation flow as well as the analysis of the output data. A detailed annotated sample script used in this work can be found in the appendix.

All simulations were carried out on the computing clusters of the Center for Scientific Computing⁸. The CPU time for the simulations varied between a few hours and 4 weeks. In total, more than 50 CPU years were used for this scientific investigation.⁹

The visualisation was done using the Visual Molecular Dynamics (VMD) software¹⁰.

⁶<http://www.espresso.mpg.de/>

⁷<http://www.tcl.tk/>

⁸<http://www.csc.uni-frankfurt.de/>

⁹The carbon footprint of this work is approximately 50t CO₂, not including any conference travel.

¹⁰<http://www.ks.uiuc.edu/Research/vmd/>, *cf.* Reference 129

4. Static properties of polyelectrolytes in electric fields

In this chapter, the proposed coarse-grained model is used to quantify the static properties of the polyelectrolyte chain and the surrounding counterions. The influence of the individual concentrations of the monomers c_{PE} and the counterions c_{CI} as well as the dependence on the strength of the external electric field E are investigated.

4.1. Introduction

The results in this chapter were obtained for polystyrene sulfonate (PSS) chains using the model described in the previous chapter with a length scale of $\sigma_0 = 2.75\text{\AA}$. The individual charges along the backbone of the polyelectrolyte have an average distance $b = 0.91\sigma_0 = 2.5\text{\AA}$, which is the charge spacing along a fully charged polystyrene sulfonate chain. The Bjerrum length is set to its value for water at room temperature $l_{\text{B}} = 2.58\sigma_0 = 7.1\text{\AA}$. The monomer concentration is systematically varied between $c_{\text{PE}} = 1\text{mM}$ and 100mM . Additional salt is added up to a concentration of $c_{\text{s}} = 1\text{M}$.

Two types of MD simulations are compared: Langevin type simulations as described in Section 3.5.1 with a friction parameter $\Gamma_0 = 15.34$ and simulations using the coupling to a Lattice Boltzmann fluid with a kinematic viscosity $\nu = 3.0$, a fluid density $\rho = 0.864$, and a bare friction parameter $\Gamma_{\text{bare}} = 20.0$ (see Section 3.5.3). The Langevin friction parameter Γ_0 and the bare friction parameter Γ_{bare} are linked to one another via Equation 3.32 and yield matching single particle mobilities. By comparing both types of MD simulations, the impact of HI on the dynamics of the system can be characterised.

The simulations are carried out with a MD time step $\tau_{\text{MD}} = 0.01$ and LB time step $\tau_{\text{LB}} = 0.05$. After equilibration of 10^6 steps, 10^7 steps are used for generating the data. The time-series are analysed using auto-correlation functions to estimate the statistical errors as detailed in Reference 127. Error bars of the order of the symbol size or smaller are omitted in the figures. Up to ten independent simulations are carried out for each data point, taking between one day and three weeks on a single standard CPU depending on the chain length N and the monomer concentration c_{PE} .

4.2. Visualisation

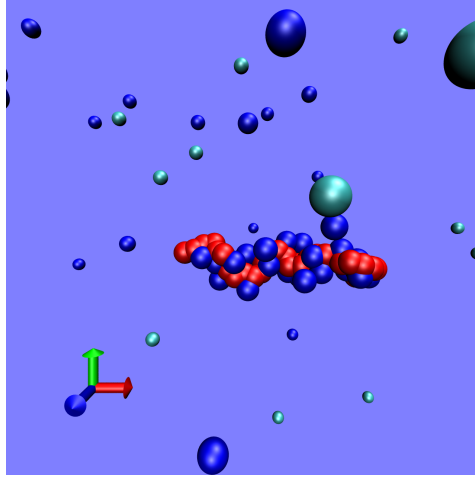


Figure 4.1: A visualisation snapshot of a system with a polyelectrolyte chain of length $N = 32$ (red beads) and the surrounding counter- and salt ions (blue and cyan).

Figure 4.1 shows a snapshot of a system of a polyelectrolyte chain of length $N = 32$ (in red) with its counterions (in blue) surrounding the chain. The simulation box also contains the same number of salt ions (in cyan). During the simulation, the monomers and the counterions move according to the acting force and fluctuate due to thermal noise. The excluded-volume effect prevents all particles in the system from overlapping, but one can see that the electrostatic interaction attracts a number of counterions to be very close to the chain. A second point to note is the extended conformation of the polyelectrolyte chain. In the following section, the chain behaviour will be investigated in detail in order to show that the charged nature of polyelectrolytes indeed gives rise to more extended conformations compared to uncharged polymers. Furthermore, the role of counterions and salt will be analysed rigorously in Section 4.4.

4.3. Chain scaling

The polyelectrolyte chain conformations can be characterised by the average square end-to-end distance

$$R_e^2 = \left\langle (\vec{r}_1 - \vec{r}_N)^2 \right\rangle, \quad (2.10)$$

the square radius of gyration

$$R_g^2 = \left\langle \frac{1}{N} \sum_i (\vec{r}_i - \vec{r}_{\text{cm}})^2 \right\rangle, \quad (2.13)$$

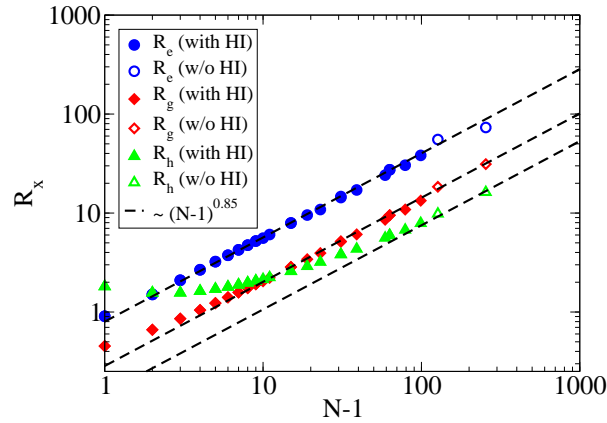


Figure 4.2: Both the end-to-end distance R_e and the radius of gyration R_g at vanishing external field for a monomer concentration of $c_{\text{PE}} = c_{\text{CI}} = 10$ mM exhibit an effective scaling exponent $\nu = 0.85$. The hydrodynamic radius R_h shows a different behaviour for short chains and only slowly reaches the asymptotic scaling. The static chain properties are not influenced by hydrodynamic interactions (HI) and fully agree with the ones obtained without HI.

and by the hydrodynamic radius

$$\left\langle \frac{1}{R_h} \right\rangle = \frac{1}{N} \sum_{i \neq j} \left\langle \frac{1}{\|\vec{r}_i - \vec{r}_j\|} \right\rangle. \quad (2.37)$$

Here N is the number of chain monomers, \vec{r}_i the position of the i -th monomer, and \vec{r}_{cm} the center of mass of the polyelectrolyte chain. The angular brackets $\langle \dots \rangle$ indicate an ensemble average. All three quantities are expected to exhibit a power law scaling $R_{e,g,h} \sim (N-1)^\nu$, where the scaling exponent ν depends on the system. For an uncharged polymer with ideal chain behaviour $\nu \approx 0.588$ (Flory exponent) [53], whereas for a fully charged polyelectrolyte without electrostatic screening $\nu = 1$.

Figure 4.2 shows $R_{e,g,h}$ for polyelectrolyte chains of different length in the presence of the neutralizing counterions at a concentration for monomers and counterions of $c_{\text{PE}} = c_{\text{CI}} = 10$ mM and in the absence of an external field. An effective scaling exponent $\nu \approx 0.85$ for R_e and R_g for chains up to $N = 256$ is obtained, which is an indication of the electrostatic screening and the counterion influence on the chain conformations. The hydrodynamic radius R_h exhibits a very slow asymptotic behaviour which leads to a lower apparent scaling exponent for short and intermediate chains. In Chapter 5, it will be shown that this is in perfect agreement with the measured diffusion coefficients. Figure 4.2 shows no influence of hydrodynamic interactions on static chain properties.

4. Static properties of polyelectrolytes in electric fields

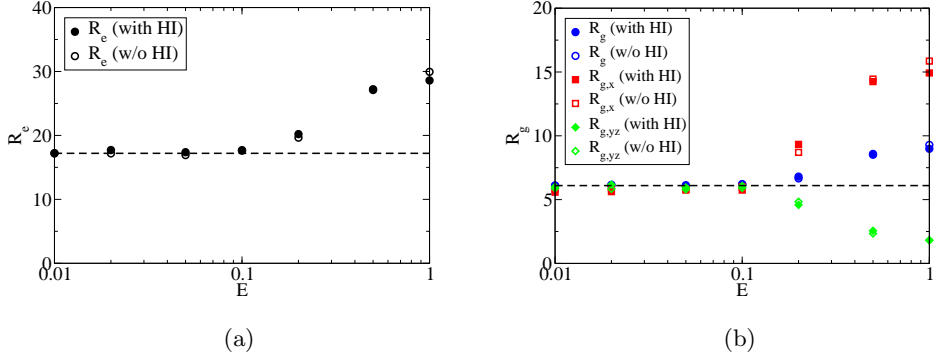


Figure 4.3: The end-to-end distance R_e (a) and the radius of gyration radius R_g (b) for a chain of $N = 40$ monomers differ from the value at zero external field E (dashed line), if a critical value is reached. Beyond this threshold, the polyelectrolyte chain is extended (increased R_e and R_g) and starts to align with the field directed in x-direction as indicated by the quantities $R_{g,x}$ and $R_{g,yz}$. This effect is independent of hydrodynamic interactions (HI).

If the polyelectrolyte chain is subjected to a strong external electric field E , depending on the magnitude of E , conformational changes might be induced [130].

Figure 4.3 shows that the model polyelectrolyte of length $N = 40$ experiences conformational changes if the external electric field is $E_{\text{crit}} \geq 0.2$. According to [130, 131], E_{crit} is depending on the strength of the electrostatic coupling and on the length N . The approximation calculates the critical field strength that polarizes the polyelectrolyte chain sufficiently to make the transition from a coil like structure to an extended structure energetically favourable. It yields $E_{\text{crit}} \approx \sqrt{l_b/N} \approx 0.25$, a value comparable to the one obtained in this study.

The increased end-to-end distance (Figure 4.3a) indicates that the polyelectrolyte chain conformation is extended. This can also be seen by looking at R_g in Figure 4.3b. Additionally, two new observables

$$R_{g,x}^2 = \left\langle \frac{3}{N} \sum_i (\vec{r}_{i,x} - \vec{r}_{\text{cm},x})^2 \right\rangle \quad (4.1)$$

and

$$R_{g,yz}^2 = \left\langle \frac{3}{2N} \sum_{i,\alpha=y,z} (\vec{r}_{i,\alpha} - \vec{r}_{\text{cm},\alpha})^2 \right\rangle, \quad (4.2)$$

are introduced, where $r_{i,\alpha}$ is the position component in α -direction of the i -th particle. For an isotropic chain, $R_g = R_{g,x} = R_{g,yz}$, which is shown in Figure 4.3b for $E \leq 0.1$. For electric fields beyond the threshold, an increase of $R_{g,x}$ and a decrease of $R_{g,yz}$ is observed. This can be understood as an extension of the polyelectrolyte

conformation in x-direction (into the direction of the external field) and a compression perpendicular to it. This alignment in high electric fields has also been studied in Reference 132. There it was shown that for even higher fields and stiff polymers, the phase of alignment along the electric field is followed by an alignment perpendicular to it. This transition has also been recently observed by [133]. Figure 4.3 also shows that this effect is independent of long range hydrodynamic interactions, which is consistent with the initial observations by Netz that were obtained without the inclusion of hydrodynamic interactions [130, 131].

For the purpose of this thesis, it is noted that for electrical fields of $E = 0.1$ or lower, no conformational change and orientation are induced.

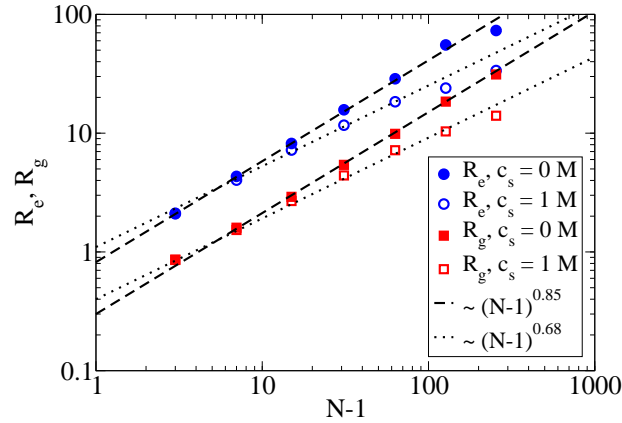


Figure 4.4: The end-to-end distance R_e and the radius of gyration R_g at zero external field, monomer concentration $c_{PE} = 10$ mM, and no added salt ($c_s = 0$ M) exhibit an effective scaling exponent $\nu = 0.85$ (dashed line). With $c_s = 1$ M monovalent salt added, the scaling exponent drops down to $\nu = 0.68$ (dotted line).

Adding salt to a polyelectrolyte solution screens electrostatic interactions on a length scale known as Debye length l_D . Following from Equations 2.59 and 2.61, l_D is inversely proportional to the square root of the concentration of the added monovalent salt:

$$l_D^{-1} = \sqrt{4\pi l_B (2c_s + c_{CI}) N_A}, \quad (4.3)$$

where c_s is the concentration of the monovalent salt, c_{CI} is the concentration of the polyelectrolyte's counterions and N_A is the Avogadro number. In Figure 4.4, the screening effect of added salt can be seen. The scaling of R_e and R_g for the salt-free case ($l_D \approx 16.7$) is compared to a solution with $c_s = 1$ M of added salt ($l_D \approx 1.2$). The additional salt screens the electrostatic interactions between the polyelectrolyte monomers and reduces the scaling coefficient to $\nu = 0.68$, which is close to the scaling for an uncharged polymer with the Flory exponent. It remains to be pointed out that the measured scaling exponent is only an effective value for

4. Static properties of polyelectrolytes in electric fields

the length range investigated. For chains with a contour length much larger than the finite electrostatic screening length l_D , the scaling is expected to be equal to the scaling of an uncharged polymer, $\nu = 0.588$.

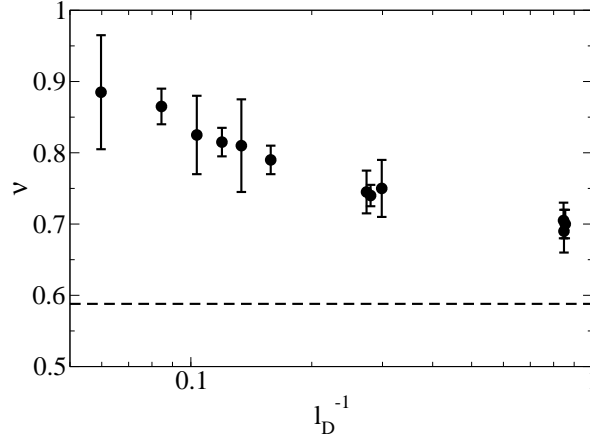


Figure 4.5: The effective scaling factor ν shows strong dependence of the Debye length. Without added salt (*i.e.*, large Debye lengths) ν is close to 1, whereas for high salt concentrations (*i.e.*, small Debye lengths) approaches the Flory number $\nu \approx 0.588$ (dashed line), the value for an uncharged polymer.

By adding salt, the polyelectrolyte conformations become less extended. The effective scaling exponent ν depends on the inverse Debye length in the system. This is illustrated in Figure 4.5: for no additional salt (small inverse Debye lengths) the observed scaling exponent is close to 1 as it is expected for an unscreened polyelectrolyte chain. As additional salt is added and thereby the inverse Debye length is increased, the scaling exponent decreases and approaches the Flory number indicated by the dashed line. The additional salt screens the electrostatic interactions along the polyelectrolyte chain, which starts to assume configurations close to those of an uncharged polymer in ideal solvent.

Note that adding monovalent salt to the solution decreases the spatial extension of the polyelectrolyte chain and makes the conformations more compact.

4.4. Counterions

After looking at the chain conformations, now the counterion distribution around the polyelectrolyte chain is investigated. The model results for counterion condensation are then compared to the predictions from Section 2.4.2.

4.4.1. Counterion condensation

Strongly charged polyelectrolytes attract some of the released counterions and effectively reduce their line charge density. This phenomenon was described by Manning and Oosawa under the term counterion condensation [59, 60] and has been discussed from varying viewpoints (see [61, 62] and the references therein).

According to Manning's theory, the distribution of counterions around highly charged rod-like polyelectrolytes can be described in terms of the Manning parameter $\xi = l_B/b$, where $l_B = 2.58$ is the Bjerrum length and $b = 0.91$ is distance between charges along the backbone of the polyelectrolyte (inverse line charge density), thus $\xi = 2.84$.

Here, highly charged polyelectrolytes with $\xi > 1$ are investigated, for which a finite number of counterions is always found in close vicinity of the polyelectrolyte chain, thus reducing the effective charge of the created polyelectrolyte-counterion compound. The theory predicts the fraction of those condensed counterions to be $f_{\text{CI}} = 1 - 1/\xi$, albeit without specifying the actual distance to the chain in which those counterions are to be found. Following the prediction, the total number is

$$N_{\text{CI}} = (1 - 1/\xi) N, \quad (2.51)$$

where N is the length of the polyelectrolyte. This leads to a predicted effective charge $Q_{\text{eff}}(N) = (1/\xi) N$.

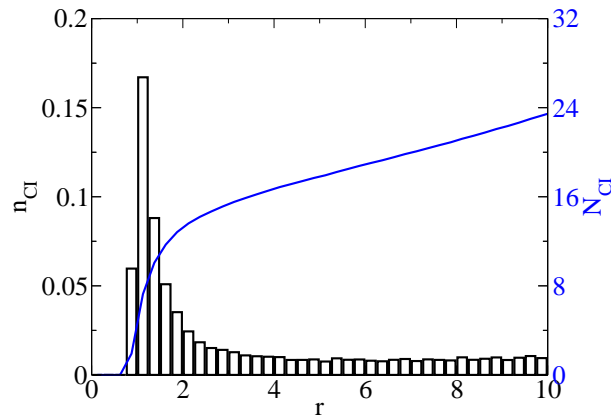


Figure 4.6: The histogram of the fraction of counterions, n_{CI} , for a chain of $N = 32$ monomers found at a distance r to the closest chain monomer and the integrated number of counterions N_{CI} found up to this distance are a measure of the distribution of counterions around the chain.

Several observations can be made when looking at the fraction of counterions n_{CI} found at a given distance r from the closest chain monomer, as plotted in Figure 4.6 for a chain of $N = 32$ monomers. Due to the excluded volume effect,

4. Static properties of polyelectrolytes in electric fields

no counterions are found at small distances, but then many counterions are found around the distance $r \approx 1$. Here, the histogram shows a “binning effect”, *i.e.*, these first counterions are split into two bins from 0.75 to 1.0 and from 1.0 to 1.25. A more accurate binning should catch all those ions within one bin with a value of $n_{\text{CI}} \approx 0.21$. The fraction then decreases as d grows and seems to level off at a value of $n_{\text{CI}} \approx 0.9$ which is the average number expected for the chosen monomer and counterion density.

The second curve in Figure 4.6 shows the integrated number of counterions N_{CI} found up to the distance r of the closest chain monomer. Again, one can see that the majority of counterions are within close distance to the chain, *i.e.*, $N \approx 16$ for $r \approx 3.5$.

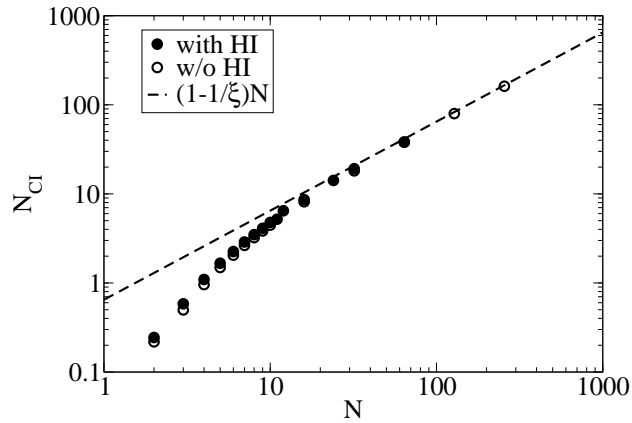


Figure 4.7: As a simple estimate of the number of condensed counterions N_{CI} all ions within a distance of $2\sigma_0$ around the polyelectrolyte chain are summed up. For long polyelectrolyte chains, the value predicted by Equation 2.51 is approached. The static counterion distributions are not influenced by hydrodynamic interactions (HI).

As the simple Manning condensation theory is not specifying a distance criterion, but instead only predicts the existence of such a finite value, a threshold has to be chosen based on other assumptions to actually estimate the number of condensed counterions. In Figure 4.7, the prediction of Equation 2.51 is compared to the number of counterions that are found within a distance of $r \leq 2$ to the closest polyelectrolyte monomer. For long polyelectrolyte chains ($N > 100$), the measured number of condensed counterions approaches the predicted value. It is noteworthy that the distribution of counterions around the chain is not influenced by hydrodynamic interactions.

Using Poisson-Boltzmann theory, it is possible to derive a distance criterion without a free cut-off parameter [63–65]. Based on the exact solution for an infinitely long

stiff rod, the cut-off is determined by the inflection point of the integrated number of counterions, N_{CI} in Figure 4.6, versus the logarithmic distance to the chain. This level of detail, however, is not needed for the investigations in this chapter.

Several ways to estimate the effective charge will be discussed and analysed in Chapter 6. In this context, the estimate based on the fixed cut-off and the one using the inflection point criterion will be revisited.

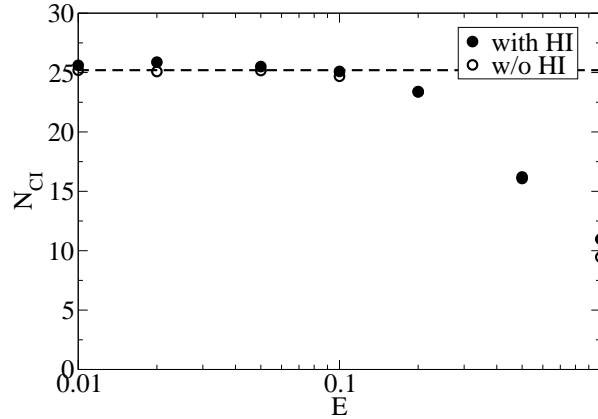


Figure 4.8: The number of condensed counterions N_{CI} for a polyelectrolyte chain of $N = 40$ depends on the applied external electrical field. Above a threshold of $E = 0.1$, counterions start to be stripped from the polyelectrolyte chain and N_{CI} differs from the value at zero field (dashed line). This effect is independent of hydrodynamic interactions (HI).

An external electric field not only couples to the polyelectrolyte monomers, but also acts on the oppositely charged counterions. Strong electric fields are known to reduce the number of condensed counterions in the vicinity of the chain [130, 131]. In Figure 4.8, the number of counterions within $2\sigma_0$ around a polyelectrolyte chain with $N = 40$ monomers is determined for different values of the applied electric field. Beyond a critical threshold of $E \approx 0.2$, counterions are stripped away from the polyelectrolyte chain. The onset of this effect coincides with the observed extension and alignment of the chain (Figure 4.3).

Again, it is noted that for electrical fields of $E = 0.1$ or lower, no change to the counterion distribution around the polyelectrolyte chain is found.

4.4.2. Radial distribution functions

In addition to the absolute quantities for the size of the polyelectrolyte, R_e and R_g and the number of counterions, the structure of the polyelectrolyte-counterion complex can be described by radial density distributions. In Figure 4.9, the radial

4. Static properties of polyelectrolytes in electric fields

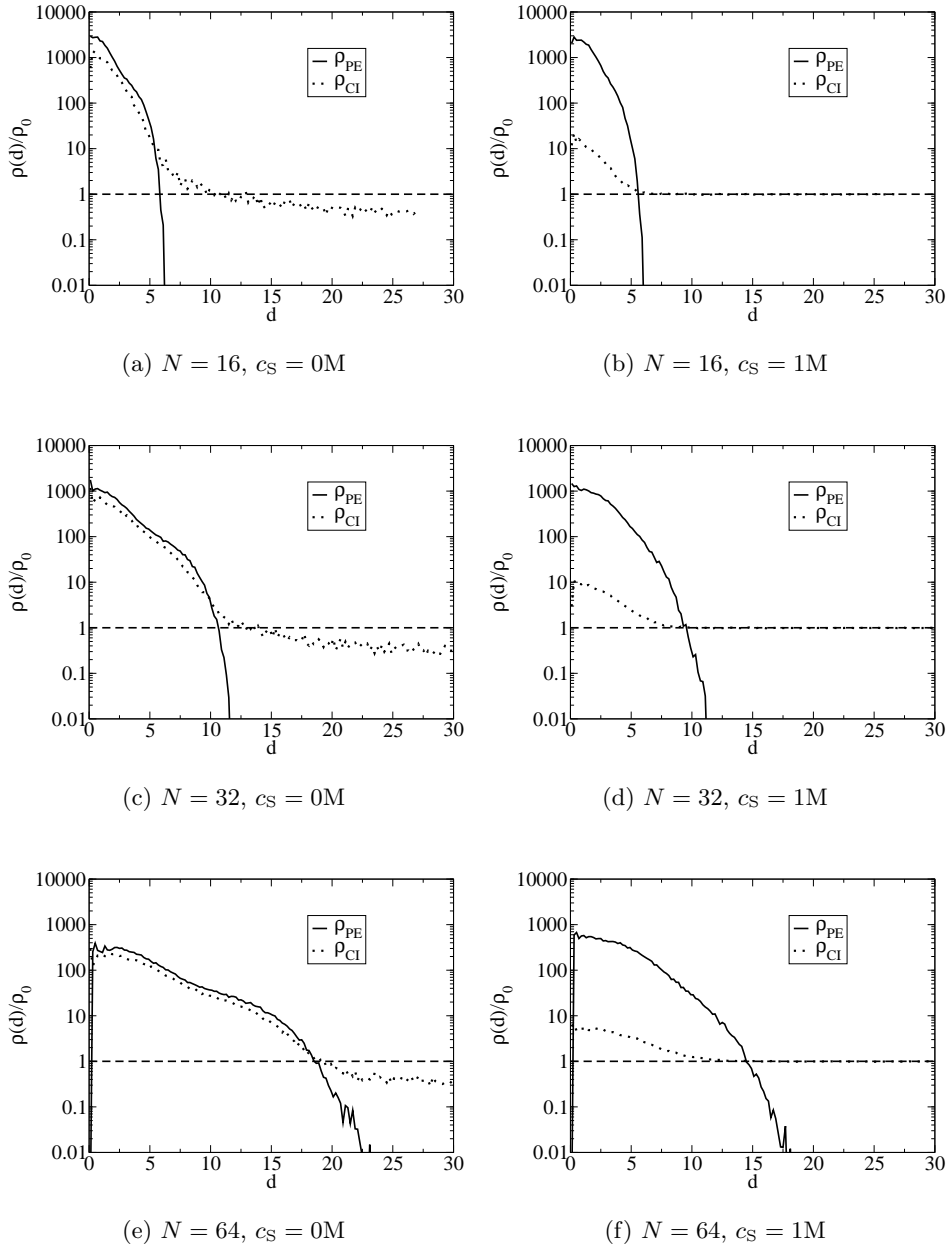


Figure 4.9: Radial density distribution functions for polyelectrolyte monomers ρ_{PE} and its counterions ρ_{CI} with (a, c, e) and without additional salt (b, d, f). Here $d = \|\vec{r}_i - \vec{r}_{cm}\|$ is the distance to the center of mass of the polyelectrolyte, and N is the length of the polyelectrolyte. It can be seen that the counterion density is increased significantly above the average value ρ_0 within the polyelectrolyte coil, indicating the strong attraction of counterions.

density distribution functions for polyelectrolyte monomers ρ_{PE} and their counterions ρ_{CI} are compared in the salt-free case and the added salt case. In Figure 4.9 shows chains of different lengths from $N = 16$ to 32 . Note that here, unlike in Figure 4.6, the radial distance d is determined to the center of mass of the polyelectrolyte: $d = \|\vec{r}_i - \vec{r}_{\text{CM}}\|$. The decay of ρ_{PE} defines the boundary of the polyelectrolyte. It is clearly seen that ρ_{CI} is increased beyond the average value ρ_0 within the polyelectrolyte coil, which is a clear indication of a strong counterion attraction.

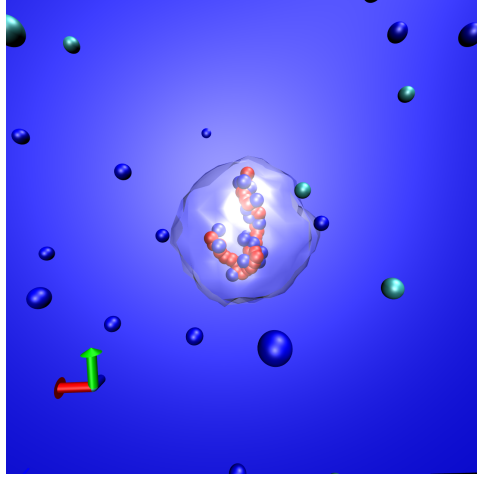


Figure 4.10: A simulation snapshot for a polyelectrolyte chain of length $N = 32$ with surrounding ions. The translucent sphere represents the boundary of the radial distribution function for the chain monomers in the center of mass frame of the polyelectrolyte. The polyelectrolyte conformation and its fluctuations give rise to roughly spherical shape when averaged over time.

The sharp decrease of the radial distribution function for the chain monomers ρ_{PE} in the chain's center of mass reference frame can be used to determine the relative size of the polyelectrolytes. Figure 4.10 shows a simulation snapshot of a chain of length $N = 32$ and its surrounding ions including a visualisation of the boundary of ρ_{PE} in three dimensions. The polyelectrolyte conformations, when averaged over time, give rise to a spherical shape. However, it is important to note that this “sphere” is not a solid object but can be penetrated by the fluid. This can also be seen when comparing the apparent sizes, *i.e.*, $R_g \approx 6, 12, 22$ for $N = 16, 32, 64$ respectively, to the hydrodynamic radius R_h shown in Figure 4.2, *i.e.*, $R_h \approx 2.6, 3.9, 6.1$. Even though the real hydrodynamic size of the object is significantly smaller, the density distribution functions support the idea that, when averaged over time, the shape of the polyelectrolyte, as seen by the fluid, is a spherical object with a well-defined size.

4.5. Summary

The static chain properties have been tested under variation of the external electric field and the concentration of additional salt. The static properties are not influenced by the presence of hydrodynamic interactions, which also serves as a testing ground for the model. The results show the expected behaviour of polyelectrolyte chains: the scaling of $R_{e,g,h}$ for short chains exhibits an effective exponent that lies between the infinite dilution exponent, $\nu = 1$, and the Flory exponent for uncharged chains, $\nu = 0.588$. The effective exponent ν decreases with increased salt concentration due to electrostatic screening.

Furthermore, the influence of the strength of an applied external electric field on the chain conformations and the counterion cloud was tested. Below a critical value E_{crit} , no dependence on the field strength is observed, which is in agreement with linear response theory. The application of field strengths above E_{crit} changes the static and dynamic properties of the polyelectrolyte. The threshold identified in this study is in agreement with theoretical predictions by Netz [130, 131].

5. Dynamic properties

In the previous chapter, the static properties of polyelectrolyte chains were investigated and characterised. A particular focus was put on the role of counterions and the influence of the electric field. In this chapter, the dynamic properties as measured in electrophoretic experiments will be investigated.

After a brief introduction, the theoretical and experimental background on free-solution electrophoresis will be reviewed. Then, the transport coefficients of polystyrene sulfonate (PSS) will be determined and compared to the available experimental data. Additionally, the role of the counterions and the influence of the electric field is analysed, but the key point of this chapter is the study of the importance of hydrodynamic interactions.

5.1. Introduction

Electrophoresis methods are widely used to separate (macro)biomolecules [72, 134] such as peptides, proteins, and DNA, as well as synthetic polymers [135, 136]. Short polyelectrolytes can conveniently be separated in free solution without the aid of a gel by capillary electrophoresis (CE). Additionally, CE is employed to characterise the hydrodynamic properties of charged biomolecules, in particular the electrophoretic mobility, μ , the diffusion coefficient, and the hydrodynamic radius [28, 32].

Alternatively, these properties can be determined by pulsed field gradient (PFG) NMR [137, 138]. With a combination of diffusion NMR and electrophoretic NMR, the charge of macromolecules [139], the influence of ionic strength and the dielectric constant of the solution have been investigated [140–142].

Several studies of polyelectrolytes of well defined length in the short chain regime have shown that the free-solution mobility μ exhibits a characteristic behaviour [32, 33, 73, 74] (see Figure 2.9 on page 27): from the monomer mobility, μ_0 , onwards, μ increases towards a maximum, μ_{\max} that occurs for chains of a specific degree of polymerisation N_{\max} . After this maximum, μ decreases slightly to reach a constant value, μ_{FD} , the so-called free draining mobility. Very little is known about the origin of the maximum, yet the knowledge of the precise dynamic behaviour of a polyelectrolyte is a prerequisite for designing possible applications in microfluidic devices, such as electrophoretic separation or gene sequencing.

Whether or not a mobility maximum appears and the precise value of N_{\max} seems to depend on the flexibility of the chain. While a maximum has been observed for flexible polyelectrolytes, such as single stranded DNA or sulfonated polystyrene

5. Dynamic properties

(PSS) with $N_{\max} \approx 10$ for the latter [33, 73, 74], semi-flexible double-stranded DNA does not exhibit it. The small number for N_{\max} and the strong influence of the persistence length show that a short chain behaviour must be responsible for this. Furthermore, it has been shown that the μ_{\max} is diminished under elevated salt conditions.

Existing theories [33, 37–39, 73] have been successful in describing the qualitative behaviour of an initially rising mobility as well as the constant long-chain limit, but they have not been able to reproduce this maximum or explain its origin. As discussed in Chapter 2, this can be attributed to some extent to the simplifying assumptions made in those models regarding the interplay of the various interactions.

To provide a fundamental understanding of the involved dynamics, it is mandatory to study the effects of these forces on a microscopic level, thereby taking into account full electrostatic as well as hydrodynamic interactions. In the following, the coarse-grained Molecular Dynamics model presented in this thesis is used to determine the dynamic transport coefficients of strong polyelectrolytes in free-solution electrophoresis and demonstrate that the chosen model *quantitatively* reproduces experimental results obtained by two completely different experimental techniques. The results of this chapter will be used in the following chapters to characterise the hydrodynamic interactions between solvent and solute on a microscopic level, and determine the relevant length scale for these interactions.

5.2. Experimental techniques

The simulation results are compared to two different experimental techniques used to measure transport coefficients of the standard polyelectrolyte polystyrene sulfonates. The capillary electrophoresis experiments were carried out by Hervé Cottet¹ and the electrophoresis NMR experiments were done out by Ulrich Scheler and Ute Böhme².

5.2.1. Capillary Electrophoresis

Capillary electrophoresis (CE) is an analytical separation technique based on the differential migration of ionic species under electric field [72, 143]. Separation occurs in a narrow bore capillary (25–100 μm diameter) using high electric field (100–1000 V/cm) (*cf.* Figure 2.8 on page 25). In Capillary Zone Electrophoresis (CZE), the capillary is filled with an electrolyte and both ends of the capillary are dipped in reservoirs filled with the same electrolyte. Samples are injected in the capillary, whereas electrolyte conditions and electric field are kept constant. The apparent

¹Institut des Biomolécules Max Mousseron, (UMR 5247 CNRS - Université de Montpellier 1 - Université de Montpellier 2), 2, place Eugène Bataillon CC 017, 34095 Montpellier Cedex 5, France

²Leibniz Institute of Polymer Research, Hohe Str. 6, D-01069 Dresden, Germany

electrophoretic mobility μ_{app} of the solute is determined according to equation 5.1:

$$\mu_{\text{app}} = \frac{v_{\text{app}}}{E} = \frac{Ll}{Vt_{\text{app}}} \quad (5.1)$$

where v_{app} is the apparent velocity, E is the electric field, V is the applied voltage, L is the total length of the capillary, l is the migration (or effective) length up to the detector and t_{app} is the apparent detection time of the solute. The apparent mobility is the sum of two distinctive contributions. One comes directly from the effective electrophoretic mobility of the solute (μ_{ep}), the other is due to the mobility of the electroosmotic flow (μ_{eo}). The electroosmotic flow (EOF) refers to the movement of the solvent in a capillary under the influence of an electric field. Indeed, under neutral or basic conditions, the negatively charged wall of the fused silica capillary attracts the cations of the electrolyte generating the so-called electrical double layer. When a voltage is applied across the capillary, cations of the double layer migrate in the direction of the cathode, dragging water molecules with them and generating this EOF. Anionic solutes (like the polystyrene sulfonates) migrate in counter-electroosmotic mode (*i.e.*, against the electroosmotic flow). Thus, the effective electrophoretic mobility is related to the apparent electroosmotic (μ_{eo}) mobilities according to equation 5.2:

$$\mu_{\text{ep}} = \mu_{\text{app}} - \mu_{\text{eo}} = \frac{Ll}{Vt_{\text{app}}} - \frac{Ll}{Vt_{\text{eo}}}, \quad (5.2)$$

where t_{eo} is the migration time of a neutral molecule. Cations have positive μ_{ep} values while anions have negative μ_{ep} values.

Experimental setup

The CE experiments considered here were performed using an Agilent technologies capillary electrophoresis system (Agilent, Waldbronn, Germany). Capillaries of 33.5 cm (25 cm to the detector) length, and 50 μm diameter were prepared from bare silica tubing purchased from Supelco (Bellefonte, PA, USA). New capillaries were conditioned by performing the following flushes: 1M NaOH for 30 min, 0.1 M NaOH for 10 min, and water for 5 min. Samples were introduced hydrodynamically (~ 4 nl) at 0.5 g/l concentration ($\sim 2.5\text{mMol/l}$ monomer concentration). The electrolyte was pure water. Solutes were detected at 225 nm. The electric field was kept constant at 224 V/cm ($V=+7.5$ kV). The polarity of the applied voltage on the inlet side of the capillaries was positive. All the experiments were performed at 27 °C. Electroosmotic mobilities were determined from the migration time of a neutral marker (mesityl oxide, $\sim 0.1\%$ (v/v) in the electrolyte).

The sodium polystyrene sulfonate standards ($M_w 1.430 \times 10^3, 5 \times 10^3, 8 \times 10^3, 16 \times 10^3, 31 \times 10^3, 41 \times 10^3, 88 \times 10^3, 177 \times 10^3, 350 \times 10^3$; M_w/M_n ca 1.1) were purchased from American Polymer Standards Corp. (Mentor, OH, USA). Borax (disodium tetraborate decahydrate) was from Prolabo (Paris, France). Mesityl oxide used as

5. Dynamic properties

neutral marker was obtained from Aldrich. Purified water delivered by an Alpha-Q system (Millipore, Molsheim, France) was used to prepare all electrolytes and sample solutions.

5.2.2. Electrophoresis NMR

In *electrophoresis NMR*, diffusion and electrophoretic motion are separated by the design of the experiment [144]. No gel has been used, so that self diffusion and free electrophoresis are measured. The PSS samples have been obtained from Fluka. To minimise the effects of variations of the ionic strength [140], samples have been dialysed against water (cutoff volume 0.5 kDA), and subsequently dried under vacuum. For all experiments a concentration of 5 mMol/l (monomer) in deuterated water has been used. The system temperature is kept at ambient level, *i.e.*, $T \approx 21^\circ$. The diffusion experiments have been performed on a Bruker Avance 500 NMR spectrometer operating at a Larmor frequency of 500 MHz for protons equipped with a DIF 30 probe head generating a maximum pulsed field gradient strength of 12 T/m. The gradient pulse duration δ and diffusion times Δ have been adjusted between 0.8 to 2 ms for δ and 8 to 20 ms for Δ respectively for optimal resolution for each molecular weight resulting in different diffusion coefficients. Because of their narrow molecular weight distribution, diffusion coefficients have been determined by a linear fit to the Stejskal-Tanner equation [137]. Electrophoresis NMR experiments have been performed on a Bruker Avance 300 NMR spectrometer operating at a Larmor frequency of 300 MHz for protons with an in-house-built electrophoresis probe head utilizing a Bruker micro2.5 imaging gradient system generating magnetic field gradient strength of up to 1 T/m. The electrophoretic mobility is a model-free read out from the two-dimensional electrophoresis NMR spectrum [139]. Data processing has been performed in MatNMR [145]. The resolution of the electrophoretic mobility is determined by the limited electric field strength, which is limited mostly by Joule heating of the sample. Since in the electrophoresis NMR experiment the only incremented variable is the electric field strength, diffusion does not influence the resolution.

5.3. Determining transport coefficients in simulations

The simulation model is used to determine two different transport coefficients for the model polyelectrolyte that are likewise determined in the associated experiments.

5.3.1. Diffusion

The diffusion coefficient D characterises the thermal motion of the polyelectrolyte. It is obtainable from the simulation trajectory of the polyelectrolyte chain, by measuring the slope of the center of mass' mean-square displacement

$$D = \frac{\left\langle [\vec{r}_{\text{cm}}(t) - \vec{r}_{\text{cm}}(0)]^2 \right\rangle}{6t}, \quad (2.25)$$

5.3. Determining transport coefficients in simulations

where \vec{r}_{cm} is the position of the center of mass, and t is the time. The angular brackets $\langle \dots \rangle$ indicate the averaging over many configurations.

Alternatively, the diffusion coefficient D can be obtained from the integration of the velocity auto-correlation function of the center of mass

$$D = \frac{1}{3} \int_0^{\infty} \langle \vec{v}_{\text{cm}}(t) \cdot \vec{v}_{\text{cm}}(0) \rangle dt. \quad (5.3)$$

Here, \vec{v}_{cm} is the center of mass velocity of the polyelectrolyte at a given time. Again, the angular brackets $\langle \dots \rangle$ indicate the averaging over many configurations.

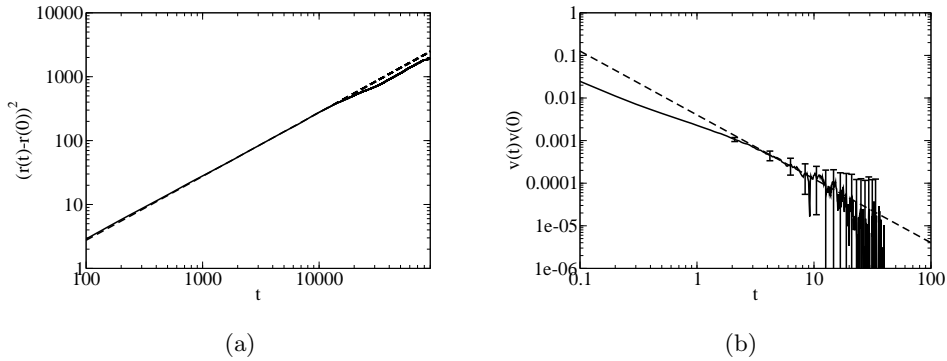


Figure 5.1: The diffusion coefficient D of a polyelectrolyte chain of length $N = 32$ is determined (a) via a fit (dashed line) to the linear part of the mean square displacement, which yields a diffusion coefficient of $D = 0.0045 \pm 0.0002$ via Equation 2.25, (b) and via fitting a $t^{-3/2}$ power law to the long-time tail of the center of mass auto-correlation function and using Equation 5.3, which results in $D = 0.0041 \pm 0.0005$.

The accuracy of both methods depends on the number of statistically independent data samples. In Figure 5.1, sample graphs to determine the diffusion of a polyelectrolyte chain of length $N = 32$ using Equations 2.25 and 5.3 are presented. Since simulations with hydrodynamic interactions are computationally very demanding, the achievable accuracy is limited. The errors are determined from the statistical fluctuations of the data and the uncertainty in the fit parameter.

In Figure 5.1a, the diffusion is obtained from a fit to the linear part of the mean square displacement. This yields a diffusion coefficient of $D = 0.0045 \pm 0.0002$ in simulation units. To calculate the integral in Equation 5.3, a fit to the slowly decaying long-time tail of the center of mass' velocity auto-correlation function has to be obtained as shown in Figure 5.1b. Here, the theoretical predicted functions are used to match the long-time tail: without hydrodynamic interactions, an exponential decay of the velocity correlations is expected, whereas with hydrodynamic interactions the correlation function decays with $t^{-3/2}$. The figure shows the more interesting

5. Dynamic properties

case with hydrodynamic interactions. The combined results of simulation data and long-time fit are integrated and a diffusion coefficient of $D = 0.0041 \pm 0.0005$ is obtained, which is in agreement with the corresponding value obtained from the mean square displacement.

Both methods are strictly equivalent for classical systems, but for the remainder of this thesis, the integral method is used to obtain the diffusion coefficient as one can use a similar formulation to obtain the mobility of the polyelectrolyte (see Equation 5.4), and thus can determine both quantities without additional computational effort. Specifically, both auto-correlation functions have to be determined accurately on the interval $t = [0, 100]$, whereas the root mean square displacement has to be determined on the interval $t = [100, 100000]$, as shown in Figure 5.1. The chosen sampling procedure, *cf.* Section 3.6.1, has been optimised for the calculation of the auto-correlation functions.

5.3.2. Electrophoretic mobility

The second transport coefficient of interest is the electrophoretic mobility μ . It characterises the motion of the polyelectrolyte in an external electric field.

In capillary electrophoresis experiments [72], the electrophoretic mobility of the solute is determined by Equation 5.1. This method can be directly transferred and applied to computer simulations. The external electric field E is modelled by a constant force proportional to the electric charge acting on the particles in the solution. This causes a directed motion with a certain velocity v . From this one can obtain the electrophoretic mobility

$$\mu = \frac{v}{E}. \quad (2.64)$$

Transforming this in a straightforward way to simulations is not always advantageous. Polyelectrolyte mobilities in free solution are of the order of $4 \cdot 10^{-8} \text{ m}^2/\text{Vs}$ [74, 140, 146, 147]; under experimentally used electric fields of up to 1000 V/cm, this leads to a velocity of about 100 nm/s. Having in mind the natural diffusive motion with a diffusion constant of $D \approx 10^{-10} \text{ m}^2/\text{s}$ [140, 148], this directed electrophoretic motion is difficult to separate from the underlying fluctuations within the accessible time frame of simulations that usually is limited to microseconds.

This problem can be overcome by simulating long trajectories at the expense of computing time. Applying an artificially high external field also reduces the computational effort, but may induce a conformational change of the polyelectrolyte and its surrounding counterions, which leads to significant discrepancies between experimentally observed results and simulations as shown in the case of static properties in the previous chapter. According to Netz *et al.* this effect is attributed to the polarisation and the following removal of the counterion cloud surrounding the polyelectrolyte [130, 131]. Below a critical value, the mobility is not affected by the electric field, and the system is in the linear response regime.

Experimentally used electric fields are usually below 1 kV/cm, which corresponds to a reduced field strength of $E = 0.001$, and as such are far below the critical

threshold. This study focuses on the behaviour of polyelectrolytes in weak electric fields below the threshold of $E \approx 0.2$ identified in Chapter 4. For simulations, the usage of a weak electrical driving force requires long simulation times, in order to be able to accurately separate the directed motion from the thermal fluctuations.

Alternatively, the electrophoretic mobility can be calculated from the following Green-Kubo relation

$$\mu = \frac{1}{3k_B T} \sum_i q_i \int_0^\infty \langle \vec{v}_i(0) \cdot \vec{v}_{\text{cm}}(\tau) \rangle d\tau, \quad (5.4)$$

where the summation is over all charged particles (monomers, counterions, and salt ions) in the system, and the \vec{v}_i are their individual velocities and the q_i their charges. Here, \vec{v}_{cm} is the velocity of the center of mass of the polyelectrolyte. This approach has been successfully applied in simulations of charged colloids [149, 150]. Please refer to Appendix A for a detailed derivation of Equation 5.4.

This method guarantees that no conformational changes of the chain structure or the ion distribution are induced by an artificially high external field. Another beneficial side effect of this method is that both transport properties can be obtained from the same simulation trajectories in the absence of an applied field without additional computational effort.

5.4. Results

The following results were obtained by adapting the generic model to match the properties of polystyrene sulfonate (PSS) as described in the previous chapter in Section 4.1. For the direct comparison to experimental results, the simulations were carried out under periodic boundary conditions in a rectangular simulation box of size $L = 34$ (for $N = 2$) to $L = 89$ for ($N = 32$) resulting in constant monomer concentration of approximately 1 g/l or 5 mM.

It is important to note that the two different experimental setups used different buffer solutions, aqueous borate buffer versus deuterated water, at different temperature, $T = 27^\circ$ versus $T \approx 21^\circ$, which leads to significant deviations in the absolute value of the electrophoretic mobility measured. Therefore, when comparing to the simulation data, normalised transport coefficients have to be used.

5.4.1. Diffusion

The diffusion of polymers in the presence or absence of hydrodynamic interactions is very well studied from a theoretical point of view. In general, the following Einstein equation is valid

$$D = \frac{k_B T}{\Gamma}, \quad (2.29)$$

where Γ is the so-called friction coefficient of the studied object, k_B is the Boltzmann factor and T is the temperature.

5. Dynamic properties

Without hydrodynamic interactions, one expects Rouse behaviour, *i.e.*, a friction coefficient Γ that linearly depends on the chain length N :

$$D = \frac{k_B T}{\Gamma_0 N}. \quad (2.31)$$

Here, Γ_0 is the friction coefficient of a single monomer of the polymer chain.

With hydrodynamic interactions, Zimm behaviour is expected. The scaling of D with the chain length is no longer proportional to N^{-1} , but can be described by the Kirkwood-Zimm theory [55, 57]. Within this theory, the diffusion coefficient is expected to be

$$D = \frac{D_0}{N} + \frac{k_b T}{6\pi\eta R_h}, \quad (2.36)$$

where D_0 is the diffusion coefficient of a single monomer of the polymer chain, N is the chain length, η is the viscosity of the solvent, and R_h is the hydrodynamic radius of the polymer. In general, as pointed out in Chapter 4, R_h is not linear in N , resulting in a scaling different from N^{-1} for the diffusion coefficient of a polyelectrolyte in the presence of hydrodynamic interactions.

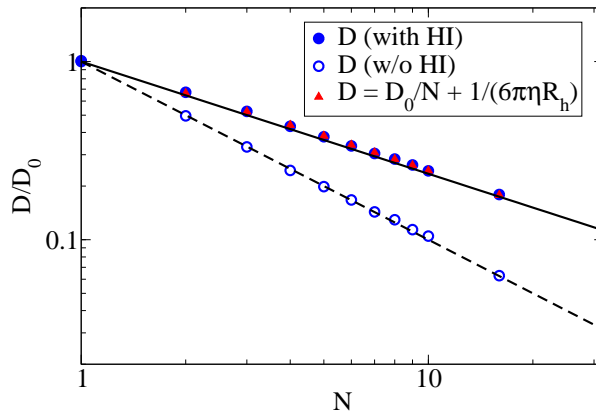


Figure 5.2: The diffusion of a polyelectrolyte chain of length N at a monomer concentration $c_m = 10\text{mM}$, normalised by the monomer diffusion D_0 , shows the influence of hydrodynamic interactions (HI). With HI a scaling exponent of $m = 0.63 \pm 0.01$ is obtained (solid line), whereas without HI, the slope is $m = 1.02 \pm 0.02$ (dashed line). The diffusion in presence of HI agrees with the values obtained from Equation 2.36, where R_h is determined from the simulation (triangles).

Figure 5.2 shows the normalised diffusion coefficient for polyelectrolyte chains of varying length with and without hydrodynamic interactions. When hydrodynamic interactions are present, the polyelectrolyte diffusion shows a behaviour which can be described by a power law scaling $D = D_0 N^{-m}$, where D_0 is the monomer

diffusion coefficient. For the model polyelectrolyte, a scaling exponent of $m = 0.63 \pm 0.01$ is observed. In order to check the validity of Equation 2.36 the hydrodynamic radius is also calculated. The data is in perfect agreement with Zimm theory. This is especially remarkable, as it shows that the presence of counterions, which are not considered in Equation 2.36, does not directly influence the diffusion of polyelectrolytes. Instead, only the conformations of the polyelectrolyte itself are determining the diffusive behaviour. The observed scaling exponent is in good agreement with experimental results for the diffusion coefficient of polyelectrolytes, as will be shown in Section 5.4.1.

When hydrodynamic interactions are switched off, the polyelectrolyte chain exhibits Rouse behaviour with a scaling of $m = 1.02 \pm 0.02$, demonstrating the importance of hydrodynamic interactions for the observed diffusion scaling with chain length.

However, as shown in the previous chapter, the static chain properties, including the hydrodynamic radius R_h do not depend on the presence of hydrodynamic interactions. This allows for the correct calculation of the diffusion coefficient even in the absence of hydrodynamic interactions by means of Equation 2.36. Having said that, the direct measurement of D is only possible when hydrodynamic interactions are included in the simulation model.

In the course of this study, the monomer concentration of the polyelectrolyte was furthermore varied from $c_m = 100$ mM up to 1 mM. Within this range, no change of diffusion coefficients was observed.

Influence of the electric field

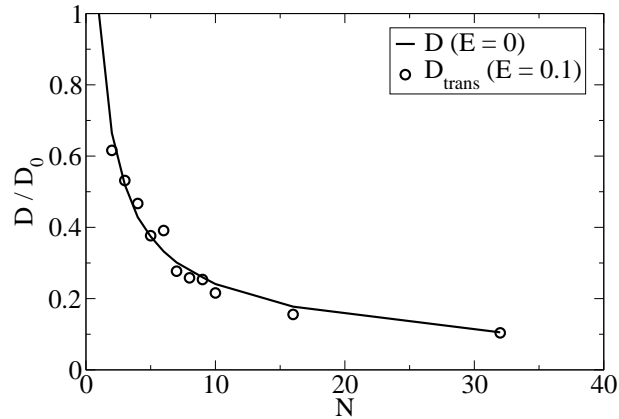


Figure 5.3: The translational diffusion coefficient measured at a reduced electric field $E = 0.1$ (circles) is in agreement with the measurements at zero electric field (solid line).

5. Dynamic properties

When an external electric field is applied to the polyelectrolyte solution the diffusive motion in the direction of the electric field is mixed with the induced directed motion. However, it is possible to determine the translational diffusion coefficient D_{trans} perpendicular to the electric field. Figure 5.3 shows that for a reduced electric field of $E = 0.1$ no deviation from the diffusive behaviour at vanishing electric field is found. This is in-line with the findings of Chapter 4, *i.e.*, that for small enough electric fields, the conformation of the polyelectrolyte chains and the surrounding counterions are unchanged, such that the measured quantities do not depend on the applied electric field.

Experimentally [140], it is also possible to determine the diffusion coefficient in the direction of the field by separating the diffusive from the directed motion. The electric field showed no influence on the diffusion coefficient.

Comparison to experimental data

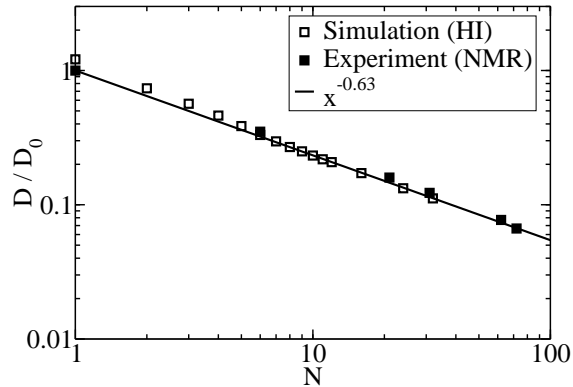


Figure 5.4: The normalised diffusion coefficient D/D_0 for PSS of different lengths N as obtained by electrophoresis NMR agrees with the simulation results with full hydrodynamic interactions (HI).

Figure 5.4 compares the diffusion coefficient D determined by simulations to the experimental results. Here, the simulated data is normalised by $D_0 = 0.052$, the monomer diffusion as obtained by a power law fit, and the experimental data by the monomer diffusion coefficient of $D_0 = 5.7 \cdot 10^{-10} \text{ m}^2/\text{s}$. The simulation data exhibit a power law scaling $D = D_0 N^m$, with a scaling exponent $m = 0.63 \pm 0.01$, which agrees with previous results. For the standard polyelectrolyte PSS (polystyrene sulfonate), Böhme and Scheler [141] obtained $m = 0.64$, whereas Stellwagen et. al. [33] reported a scaling with $m = 0.617$. It is worth mentioning that the latter value was obtained in the presence of 50 to 100 mM additional salt and for PSS chains

of up to 20000 repeat units, therefore a smaller scaling exponent can be expected as shown in Chapter 4.

Only for very short chains, ($N < 5$), is a deviation from the prediction is observed and a higher diffusion coefficient is found in the simulations. For intermediate chain length, the coarse-grained simulation model with HI, reproduces the experimentally observed behaviour.

As shown in Figure 5.2, without hydrodynamic interactions, the chains show the expected Rouse diffusion with an exponent of $m \approx 1$. From this, it can be seen that the Langevin model without hydrodynamic interactions is clearly not applicable to mimic the experimental behaviour of short polyelectrolyte chains.

5.4.2. Electrophoretic mobility

While there are several theories [36–39] that have been successfully used to describe qualitatively the experimentally observed electrophoretic behaviour of various polyelectrolytes, there are still some open questions to address. Recent experiments on strongly charged flexible polyelectrolytes, such as polystyrene sulfonate (PSS) and single-stranded DNA (ssDNA) of well defined length, have shown a characteristic behaviour for the short chain free-solution mobility μ [32, 33, 73, 74]: after an initial increase of the mobility with increasing length, μ passes through a maximum, and then decreases towards a constant mobility for long chains.

As mentioned earlier, the increase for short chains and the long-chain limit can be explained within the theoretical approaches, but the origins of the maximum for intermediate chains are not accounted for. This chapter will show that the experimentally observed behaviour can be simulated using a coarse-grained model. In Chapter 6, it will be shown that the maximum appears due to the hydrodynamic interactions between the polyelectrolyte, its counterions, and the solvent.

Figure 5.5 illustrates that the maximum in the electrophoretic mobility can only be reproduced when hydrodynamic interactions are properly accounted for. The neglect of hydrodynamic interactions leads to a decreasing electrophoretic mobility for short chains. This observation was also made in a recent publication by Frank and Winkler [133].

In addition to the measured mobilities, Figure 5.5 includes a prediction for the mobility without hydrodynamic interactions based on local force balance: without hydrodynamic interactions, every particle of the polyelectrolyte-counterion compound is subject to the same frictional force $F_{\text{Solvent}} = -\Gamma_0 v$ counterbalancing the electric driving force $F_{\text{Field}} = q_i E$. From this one can obtain the following expression for the electrophoretic mobility in the absence of hydrodynamic interactions, where $\mu_0 = 1/\Gamma_0$ is the mobility of a single monomer, N is the length of the polyelectrolyte, and N_{CI} is the number of condensed counterions that move with the polyelectrolyte:

$$\frac{\mu}{\mu_0} = \frac{N - N_{\text{CI}}}{N + N_{\text{CI}}}. \quad (5.5)$$

5. Dynamic properties

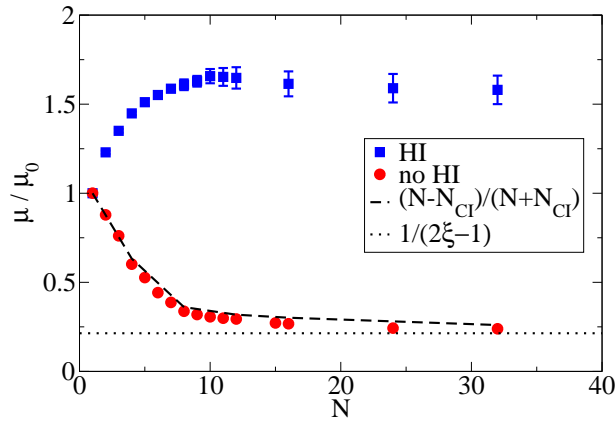


Figure 5.5: The normalised electrophoretic mobility at a monomer concentration of $c_m = 5$ mM with hydrodynamic interactions (HI) reproduces the experimentally observed behaviour and shows a maximum for intermediate chains. Without HI the measures mobility strongly deviates from this, showing a decrease with increasing chain length N . This behaviour can be explained by Equation 5.5 in the local force picture (dashed line) and approaches the limiting value of the Manning prediction (Eq. 5.6).

For plotting Equation 5.5 in Figure 5.5, N_{Cl} is obtained by counting the average number of counterions found within $2\sigma_0$ of the chain as done in Section 4.4.1. Additionally, one can substitute N_{Cl} from Eq. 2.51 and obtain the Manning prediction for the mobility

$$\frac{\mu}{\mu_0} = \frac{1}{2\xi - 1} \approx 0.2, \quad (5.6)$$

that is approached nicely for long chains.

The local force picture successfully describes the observed behaviour in the absence of hydrodynamic interactions, but qualitatively fails to describe the mobility for short chains in any real experiment, where hydrodynamic interactions are obviously present.

Influence of the electric field

The effect of strong electric fields on the mobility of polyelectrolytes has been investigated theoretically before. Below the critical field strength, *i.e.*, in the linear response regime, the electrophoretic mobility μ is independent of the applied electric field. Figure 5.6 compares μ for a polyelectrolyte chain at c_m obtained at zero field via Equation 5.4 to the mobility at finite fields, $E = 0.05$ and 0.1 , via Equation 2.64. The measured values agree within their displayed precision. For comparison, all data series were obtained using the same computational effort (same

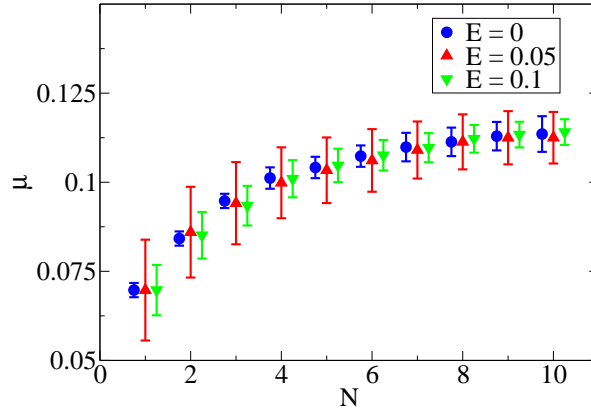


Figure 5.6: Electrophoretic mobility μ of polyelectrolyte chains at monomer concentration $c_m = 5$ mM measured without electric field (circles) and with field at $E = 0.05$ and 0.1 (triangles) with the corresponding error bar. (Data sets have been shifted to increase readability.)

number of simulation steps). For short chains, the Green-Kubo based method yields more accurate results, whereas longer chains can be simulated at equal accuracy by an external applied field. For short chains and weak fields, the thermal (Brownian) motion dominates the directed electrophoretic motion, which decreases the accuracy of the obtained values.

Based on this observation, it is concluded that the Green-Kubo method to measure the electrophoretic mobility of polyelectrolytes in solution has several advantages. Firstly and most importantly, it guarantees the measurement of free-solution mobilities in the linear regime, which are comparable to experimental measurements at standard field strengths. The alternative method uses fields that are about a factor 100 higher than the experimentally used ones and are close to the critical value at which static and dynamic properties of the polyelectrolyte are significantly changed. In the case of the electrophoretic mobility, a high electric field leads to an increased mobility due to the stripping of counterions. Secondly, the computational effort needed to achieve a given accuracy for short polyelectrolyte chains ($N < 10$) is up to 50% smaller than with the direct method. And lastly, the trajectories simulated at zero field can be used to determine the electrophoretic mobility and the diffusion (using Equation 5.3) at the same time, additionally reducing the computational cost of such a study.

Influence of the monomer concentration

It is well known that the free-solution mobility of polyelectrolytes depends on the salt concentration of the solution [73]. With increasing additional salt, the maximal

5. Dynamic properties

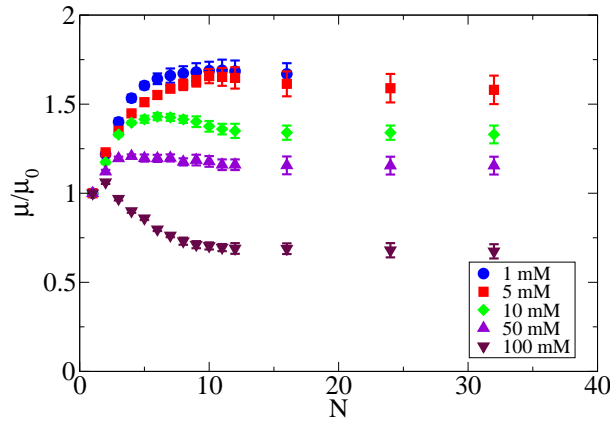


Figure 5.7: The normalised electrophoretic mobility μ/μ_0 shows a strong dependence on the monomer concentration c_m . For dilute systems the experimental behaviour is recovered, while at high monomer concentrations the shape is significantly altered.

free-solution mobility decreases due to the increased counterion condensation. The author would like to point out that the long chain mobility also shows a dependence on the monomer concentration in the absence of additional salt. This effect can be mainly attributed to the changed electrostatic screening.

Figure 5.7 shows that not only the long chain limit is influenced by increased electrostatic screening, but also the short chain behaviour. The maximum is significantly reduced for higher monomer concentrations. For $c_m = 100$ mM it is completely reduced, and the behaviour in the presence of hydrodynamic interactions is similar to the one without hydrodynamic interactions, as seen in Figure 5.5. The increased electrostatic screening caused by a higher concentration (resulting in a shorter Debye length) suppresses the short-range hydrodynamic interactions that are essential for the formation of the maximum.

This is reflected in Figure 5.8, which shows the degree of polymerisation with the maximum mobility N_{\max} versus the Debye length λ_D . The lower the Debye length, *i.e.*, the higher the electrostatic screening, the more the maximum is shifted towards short chains. This correlation has not been investigated previously. In Chapter 6, the importance of the interplay of the electrostatic screening with the hydrodynamic interactions will be analysed and found to explain this observation.

Comparison to experimental data

Figure 5.9 shows the electrophoretic mobility μ in pure water without additional salt normalised by μ_{FD} , the constant (not length-dependent) value for long chains. The simulation results are compared to two different experimental data sets. To

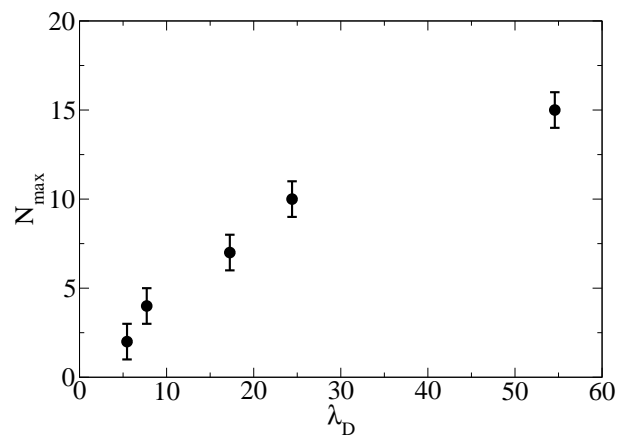


Figure 5.8: The approximate position of the maximum N_{\max} changes with the Debye length λ_D .

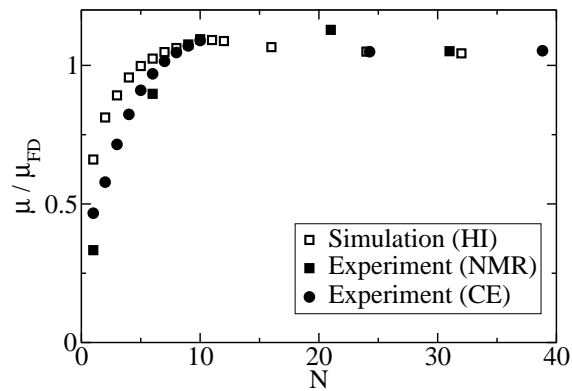


Figure 5.9: Including hydrodynamic interactions (HI), the normalised electrophoretic mobility μ/μ_{FD} as a function of the number of repeat units N obtained in simulations reproduces a maximum for intermediate chains, as well as the long-chain behaviour observed in experiments.

5. *Dynamic properties*

account for the different viscosities of the solvents, the mobilities are rescaled by the free-draining mobility μ_{FD} as obtained for long chains. The simulation results reproduce a maximum for intermediate chains as well as the long-chain behaviour (the constant mobility for long chains) observed in experiments if the hydrodynamic interactions are properly accounted for.

The experimental data sets agree within the accuracies of the individual methods and show the characteristic behaviour of the mobility in dependence to chain length. A mobility maximum for $N = 10$ is observed with capillary electrophoresis. This maximum for intermediate chains as well as the long chain behaviour is successfully reproduced in simulations with hydrodynamic interactions. For the first few oligomers, a small difference is observed, which is in line with the deviation for the diffusion. Therefore, it is inferred that the mobility maximum can only be explained when taking into account hydrodynamic interactions between the polyelectrolyte and the surrounding solvent. Similar effects were found by R. Winkler using SRD to model hydrodynamics [133].

5.5. Summary

In this chapter, the transport properties of short PSS chains were investigated via coarse-grained MD simulations, and the data was compared to two different experimental approaches. The results of experiments and simulations can be quantitatively matched and agree with the existing theoretical predictions, as long as the simulation model includes long-range hydrodynamic interactions. A simulation model that neglects hydrodynamic interactions fails to reproduce the short-length scale behaviour of the PSS diffusion coefficient and of the electrophoretic mobility.

To the author's knowledge, it has been demonstrated for the first time that the transport coefficient of short polyelectrolytes can be quantitatively modeled by coarse-grained simulation techniques. No chemical details are needed to explain the experimental results. The salient feature of our model is that it allows to simulate time scales otherwise out of reach for atomistic simulations. The short chain behaviour, as observed in experiments, is accurately reproduced when hydrodynamic interactions are included. From this observation it is concluded that hydrodynamic interactions between the chain monomers are the major reason for the existence of the maximum at intermediate length.

Having a simulation model at hand which confirms the experimental data opens new possibilities of investigating the electrophoretic behaviour of short polyelectrolytes, which so far has not been fully explained by the existing theories.

When simulating the dynamic transport properties, such as diffusion coefficient and electrophoretic mobility, the role of long-range hydrodynamic interactions becomes crucial. Only with their correct inclusion the experimentally observed behaviour is reproduced and excellent agreement between experiments and simulations is found. The presented findings demonstrate convincingly that it is possible to model the dynamic behaviour of polyelectrolytes using coarse-grained models.

6. Effective charge and effective friction

This chapter offers a detailed analysis of the electrophoretic mobility of a polyelectrolyte, especially with regards to length dependence. The observed behaviour will be explained by determining the effective friction of the polyelectrolyte chain and its surrounding counterions with the solvent. It will also be shown that the screening of hydrodynamic interactions by the counterions is essential in the explanation of the process.

6.1. Introduction

In order to quantify the hydrodynamic friction, one can start out with Equation 2.70

$$\mu = \frac{v}{E} = \frac{Q_{\text{eff}}}{\Gamma_{\text{eff}}},$$

and solve it for the effective friction Γ_{eff} :

$$\Gamma_{\text{eff}} = \frac{Q_{\text{eff}}}{\mu}. \quad (6.1)$$

The electrophoretic mobility μ as a function of the chain length N was studied in the previous chapter. Therefore, in the first section of this chapter, five different estimators to measure the effective charge Q_{eff} of polyelectrolytes in simulations and experiments are introduced. The results for μ and Q_{eff} are then combined to obtain quantitative values for the effective friction coefficient and provide interpretations of the physical processes during electrophoresis based on these observations.

6.2. Charge estimators

This section introduces five different estimators to measure the effective charge Q_{eff} of the polyelectrolyte counterion compound. The practicability and accuracy of the estimators are compared, and the obtained results are discussed in the context of polyelectrolyte electrophoresis. They will be compared to the Manning condensation theory (Equation 2.51) to check their validity. Here, retardation or polarisation effects are not taken into account, as they are negligible at the field strength usually used in electrophoresis [130, 131].

6. Effective charge and effective friction

6.2.1. Primitive estimate

A simple method of estimating the effective charge has been used in Figure 4.7 for describing the static properties of the polyelectrolyte counterion complex:

$$Q_{\text{eff}}^{(1)} = N_{\text{PE}} - N_{\text{CI}}(d < d_0), \quad (6.2)$$

where $N_{\text{CI}}(d < d_0)$ is the average number of counterions that can be found in a distance d around the polyelectrolyte, and d is the distance to the closest monomer. The threshold d_0 is usually chosen to be $d_0 = 2\sigma_0$. This method counts all counterions that are found in a flexible tube with radius d_0 around the polyelectrolyte as shown in Figure 6.1.

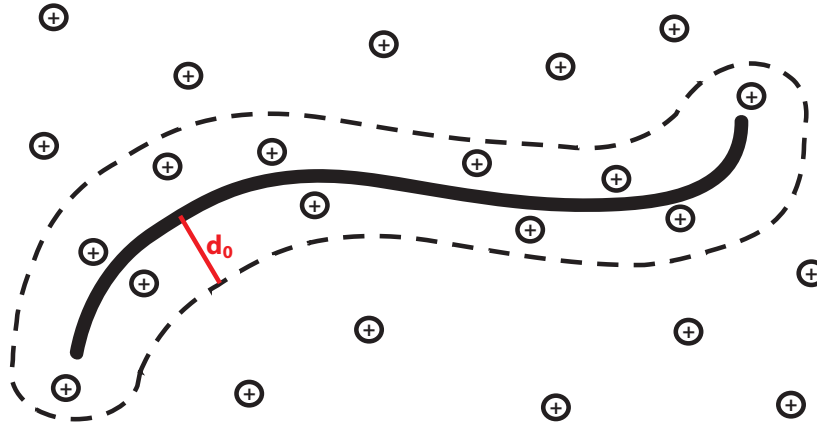


Figure 6.1: For the charge estimator $Q_{\text{eff}}^{(1)}$ all counterions are counted towards N_{CI} if they are closer to any chain monomer than d_0 . All ions within this tube are considered to be condensed.

In Section 4.4.1, it was shown that the effective charge is not affected by hydrodynamic interactions. This method is computationally inexpensive and it yields a reasonable estimate for the effective charge, as seen in Figure 4.7. The drawback is that the threshold d_0 is arbitrarily defined, which limits the accuracy of this estimator.

6.2.2. Inflection criterion

A more advanced method uses the inflection criterion to estimate the threshold of counterion condensation [63–65]. It has been shown that the position d_c of the inflection point (zero of the second derivative) for the integrated ion distribution with respect to the logarithmic distance from the closest chain monomer yields a cutoff that accurately separates free from bound counterions in the case of a rod-like

polyelectrolyte in cylindrical geometry. The applicability to polyelectrolytes will be shown here.

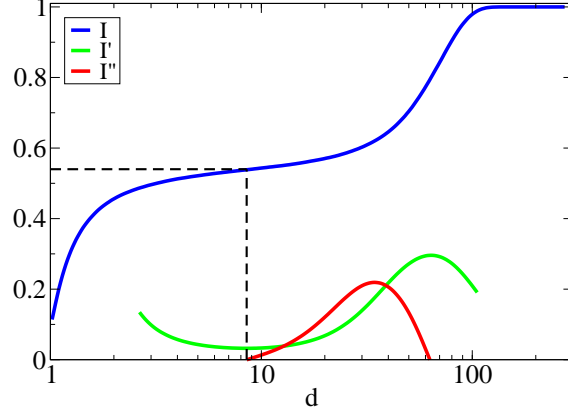


Figure 6.2: The integrated ion distribution $I(d)$ for a chain of $N = 32$ monomers shows a clear inflection point identified by the zero of the second derivative with respect to $\ln(d)$. The value of $I(d)$ at the inflection point specifies the fraction of condensed counterions f_{CI} .

The integrated ion distribution is defined as

$$I(d) = \int_0^d \rho_{\text{CI}}(r) dr = f_{\text{CI}}(r < d), \quad (6.3)$$

where ρ_{CI} is the normalised density of counterions at a distance r to the closest chain monomer, and $f_{\text{CI}}(r < d)$ is the fraction of counterions found at a distance closer than d . The total number of condensed counterions up to this distance given by the multiplication with N_{CI} .

In order to apply the inflection point criterion to the polyelectrolyte model, the integrated ion distribution has to be measured and plotted logarithmically. Figure 6.2 shows the result for a chain of $N = 32$ monomers. Additionally, the first and second derivative obtained numerically are plotted.¹ The cutoff value d_c indicated by the inflection point and the associated fraction of condensed counterions f_{CI} can be directly seen from the figure.

The effective charge of the polyelectrolyte using the inflection criterion is then given by

$$Q_{\text{eff}}^{(2)} = N_{\text{PE}} - N_{\text{CI}}(d < d_c). \quad (6.4)$$

¹Note that there is a difference between the linear (normal) derivative and the logarithmic derivative, *i.e.*, the inflection point criterion is only correct when applied to the ion distribution versus the logarithmic distance.

6. Effective charge and effective friction

N	d_c	f_{CI}	$Q_{\text{eff}}^{(2)}$
2-4	n/a	n/a	n/a
5	3.75	0.09	4.56
6	4.23	0.14	5.16
7	4.59	0.18	5.73
8	4.81	0.23	6.19
9	5.04	0.26	6.68
10	5.47	0.29	7.14
16	6.51	0.40	9.60
32	8.52	0.53	15.52
64	10.87	0.61	26.81

Table 6.1: The cutoff value d_c as obtain from the inflection point criterion in dependence of the length N of the polyelectrolyte, as well as the fraction of condensed ions f_{CI} and the resulting effective charge $Q_{\text{eff}}^{(2)}$.

The cutoff d_c is not a fixed parameter anymore, but has to be determined for every chain length. Table 6.1 shows the values used in this study and the associated values for the counterion condensation. Please note that the logarithmic inflection point criterion is not applicable to short chains, therefore no effective charge can be estimated for chains of length $N \leq 4$.

6.2.3. Langevin model

In Section 5.4.2, the local force picture was used to derive Equation 5.5 for the electrophoretic mobility in the absence of hydrodynamic interactions. Similarly, one can derive an expression for the effective charge of the polyelectrolyte in the absence of hydrodynamic interactions based on the measured mobility μ of the compound.

Starting with Equation 5.5,

$$\mu = \frac{Q_{\text{eff}}}{\Gamma_{\text{eff}}} = \frac{N - N_{\text{CI}}}{\Gamma_0 (N + N_{\text{CI}})}, \quad (5.5)$$

and solving it for N_{CI} , one obtains

$$N_{\text{CI}} = N \frac{1 - \mu\Gamma_0}{1 + \mu\Gamma_0}. \quad (6.5)$$

As before the effective charge is defined as

$$Q_{\text{eff}} = N - N_{\text{CI}}, \quad (6.6)$$

which leads to a charge estimator based on the measured mobilities in the Langevin model:

$$Q_{\text{eff}}^{(3)} = N_{\text{PE}} \left(1 - \frac{1 - \mu\Gamma_0}{1 + \mu\Gamma_0} \right). \quad (6.7)$$

Equation 6.7 offers a way to determine the effective charge of the polyelectrolyte counterion complex based on the measured mobility in the absence of hydrodynamic interactions without the need of free parameter and at reasonable computational costs. The accuracy of this estimator is limited by the accuracy of the measured electrophoretic mobility μ .

6.2.4. Ion diffusion

The local force picture used for the Langevin model assumes that a finite amount of counterions is bound to the polyelectrolyte, while the remaining ions can move freely. The N_{CI} bound counterions are expected to diffuse together with the polyelectrolyte with a diffusion coefficient D_{PE} as determined in Section 5.4.1. Likewise, the $N - N_{\text{CI}}$ free counterions will diffuse with a different diffusion coefficient D_0 . If one measures the ion diffusion coefficient D_{CI} for all N ions in such a system, the measured quantity will be the weighted average of the bound and the free diffusion coefficients:

$$D_{\text{CI}} = \frac{N_{\text{CI}}D_{\text{PE}} + (N - N_{\text{CI}})D_0}{N}. \quad (6.8)$$

From this, a novel estimator for the effective charge is derived that has the advantage of only including quantities which are experimentally accessible. As such, the estimator can be used in experiments, for example the described NMR setup, to directly measure the effective charge:

$$Q_{\text{eff}}^{(4)} = N \left(1 - \frac{D_0 - D_{\text{CI}}}{D_0 - D_{\text{PE}}} \right). \quad (6.9)$$

Figure 6.3 compares the results of estimator $Q_{\text{eff}}^{(4)}$ with and without hydrodynamic interactions and shows that, within the accuracy of the method, no difference can be observed. This indicates that the effective charge, like the static chain properties, is not affected by the presence of hydrodynamic interactions. The charge estimator presented in the following section supports this important observation.

Equation 6.9 is valid for simulations independent of the presence or absence of hydrodynamic interactions and has the computational complexity of determining the diffusion coefficients (see Section 5.4.1).

The derivation of equation 6.9 assumes the absence of additional salt, *i.e.*, $c_{\text{S}} = 0$, but it can be modified to account for a finite amount of salt. In this case, the average diffusion coefficient can be written as:

$$D_{\text{CI}} = \frac{c_{\text{M}}N_{\text{CI}}D_{\text{PE}} + (c_{\text{M}}(N - N_{\text{CI}}) + c_{\text{S}})D_0}{c_{\text{M}}N + c_{\text{S}}}, \quad (6.10)$$

which now also depends on the monomer and the salt concentration, c_{M} and c_{S} .

Solving this equation for N_{CI} yields a modified version of the charge estimator:

$$Q_{\text{eff}}^{(4')} = N \left(1 - \frac{D_0 - D_{\text{CI}}}{D_0 - D_{\text{PE}}} \right) - \frac{D_0 - D_{\text{CI}}}{D_0 - D_{\text{PE}}} \frac{c_{\text{S}}}{c_{\text{M}}}. \quad (6.11)$$

6. Effective charge and effective friction

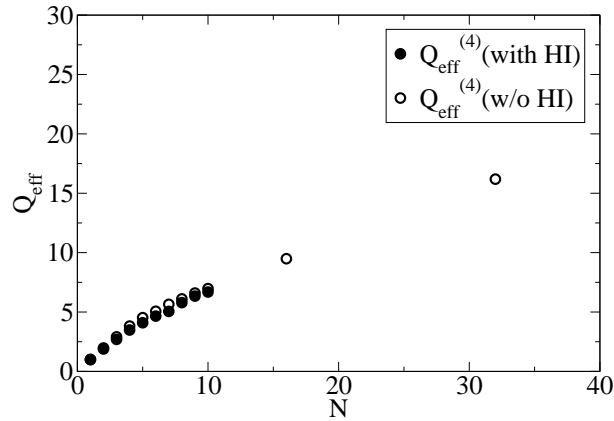


Figure 6.3: Estimated charge $Q_{\text{eff}}^{(4)}$ (Equation 6.9) of polyelectrolyte chains of varying length N with and without hydrodynamic interactions (HI).

The additional term vanishes for $c_S = 0$ and the Equation 6.9 is recovered.

The ratio between c_M and c_S strongly influences the achievable resolution. The higher the salt concentration is with respect to the monomer concentration, the smaller the difference between the free and the bound ion diffusion coefficient is. Ultimately, both diffusion coefficients become indistinguishable, which prohibits the application of this charge estimator.

A similar analysis may be performed using the free and the bound mobility, but these quantities are experimentally more difficult to obtain.

6.2.5. Co-moving counterions

The last estimator for the effective charge introduced in this thesis is based on directly determining the counterions that are co-moving with the polyelectrolyte during free-solution electrophoresis, similarly to the method used in Reference 151.

When applying an external electric field E , the polyelectrolyte moves with a velocity $v_{\text{PE}} = \mu_{\text{PE}}E$ in the direction of the electric field. Co-moving counterions move with the same velocity in the same direction, whereas free counterions move with a velocity $v_{\text{CI},0} = \mu_0E$ into the opposite direction. Here, μ_0 is the mobility of free counterions. To guarantee a linear response of the system to the electric field, a value of $E = 0.1$ has been chosen, which is well above the estimated critical field strength of $E \approx 0.25$.²

The velocity v_{CI} of the ions versus the distance d to the center of mass of the polyelectrolyte is shown in Figure 6.4. It can be seen that ions close to the center

²In principle, the relative velocity can also be calculated in the absence of an electric field leading to a similar results[152].

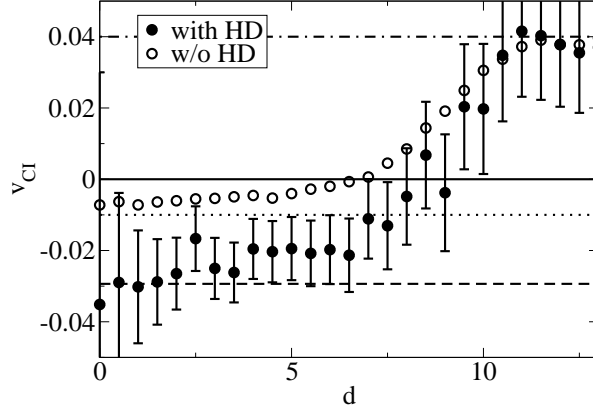


Figure 6.4: The ion velocity distribution $v_{\text{CI}}(d)$ for a polyelectrolyte chain of length $N = 32$ shows the transition from co-moving counterions with a velocity similar to v_{PE} (dashed line and dotted line indicate v_{PE} with and without hydrodynamic interactions (HI)) to the free ion velocity $v_{\text{CI},0}$ (dash-dot line). $v_{\text{CI}}(d = d_0) = 0$ defines the threshold between co- and counter-moving ions, and is used to determine the effective charge of the polyelectrolyte counterion complex in Equation 6.12.

of mass are co-moving, *i.e.*, $v_{\text{CI}} = v_{\text{PE}}$, and ions far away from the chain are indeed freely moving with a velocity $v_{\text{CI}} = v_{\text{CI},0}$. For an intermediate value of d_0 , the ion velocity v_{CI} is zero, *i.e.*, the ions are not moving in the electric field due to the interaction with the polyelectrolyte. This distance d_0 separates the co-moving counterions from the free-moving ones. Similar to $Q_{\text{eff}}^{(1)}$ (Eq. 6.2), the effective charge is obtained by averaging the number of counterions found within a distance d_0 of the center of mass of the chain.

$$Q_{\text{eff}}^{(5)} = N_{\text{PE}} - N_{\text{CI}}(d < d_0), \quad (6.12)$$

Note that for this estimator, d is the distance from the counterion to the center of mass of the polyelectrolyte, not to the closest polyelectrolyte monomer.

The results shown in Figure 6.4 indicate a small influence of the hydrodynamic interactions on the value of d_0 , but it is important to note that the ion density in this region is very low, resulting in almost identical values of the $Q_{\text{eff}}^{(5)}$ in both cases (*cf.* Figure 4.6 on page 55).

The threshold used for this estimator is not predefined, but has to be determined from the simulation and generally is a function of the chain length. Since v_{CI} has to be determined for each distance d to the center of mass of the polyelectrolyte, this estimator is computationally expensive, as a high number of statistically independent samples are required.

6.2.6. Comparison

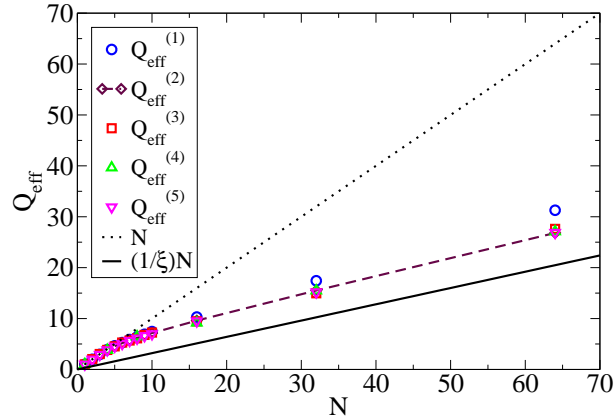


Figure 6.5: The effective charge of polyelectrolyte chains of length N using the estimators $Q_{\text{eff}}^{(1)}$ to $Q_{\text{eff}}^{(5)}$. The dotted line indicates the bare, unscreened charge of the polyelectrolyte, whereas the solid line shows a prediction based on counterion condensation theory, with $\xi = 2.84$ being the condensation parameter. Whereas estimators $Q_{\text{eff}}^{(3)}$ to $Q_{\text{eff}}^{(5)}$ agree over the range of lengths N tested, $Q_{\text{eff}}^{(1)}$ overestimates the effective charge of the polyelectrolyte counterion complex.

Figure 6.5 compares the results of all presented charge estimators $Q_{\text{eff}}^{(1)}$ to $Q_{\text{eff}}^{(5)}$. For short chains ($N < 4$), the estimators agree and coincide with the bare, unscreened charge of the polyelectrolyte. In this regime, no counterion condensation is observed.

For intermediate and long chains ($N > 4$), the effective charge is reduced as it deviates from the bare charge and tends towards the Manning prediction but does not reach it completely as the polyelectrolyte starts to assume a coiled conformation that is not accounted for in condensation theory. Here, the condensation parameter for the polyelectrolyte system is $\xi = 2.84$. In this regime, the simple estimator $Q_{\text{eff}}^{(1)}$ measures a higher effective charge, *i.e.*, not all condensed counterions that are correctly included in the other estimators are taken into account. This effect is not observed if the cutoff value is chosen using the inflection criterion.

All estimators show no or little influence of the hydrodynamic interactions on the effective charge of the polyelectrolyte counterion complex. This independence on the hydrodynamic interactions has been recently observed for highly charged colloid using a similar simulation approach [151].

Furthermore, no difference between the static estimate, $Q_{\text{eff}}^{(2)}$ and the dynamic estimates $Q_{\text{eff}}^{(3-5)}$ for the effective charge are observed. This is especially remarkable as it is an open question if there is a difference between the static and the dynamic

charge. For the case of charged colloids this seems to be the case [149, 153], but the results of this work show that for strongly charged linear polyelectrolytes both quantities are identical and one does not have to differentiate between static and dynamic charge.

6.3. Effective friction

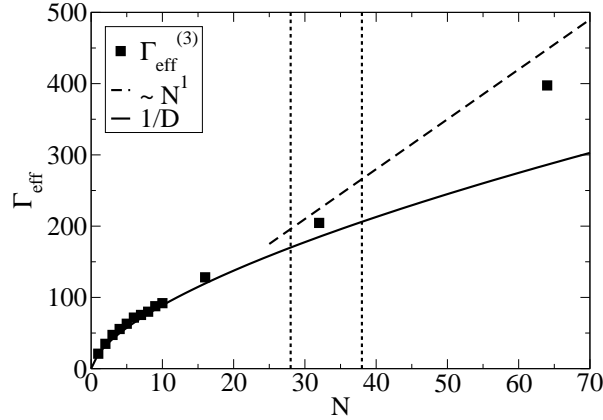


Figure 6.6: The effective friction of the polyelectrolyte counterion complex is in agreement with the hydrodynamic friction ($\Gamma = 1/D$) for short chains only. For longer chains beyond the Debye length in the system (indicated by the dashed lines) the effective friction deviates and seems to approach a linear behaviour.

Now the effective charge will be used to quantify the effective friction of the polyelectrolyte-counterion compound. As shown in Figure 6.5, the estimators $Q_{\text{eff}}^{(2)}$ to $Q_{\text{eff}}^{(5)}$ yield the same effective charge, thus only $Q_{\text{eff}}^{(3)}$ is used to determine the effective friction in the following equation:

$$\Gamma_{\text{eff}} = \frac{Q_{\text{eff}}}{\mu}. \quad (6.13)$$

Here the electrophoretic mobility μ obtained in Section 5.4.2 is used.

The result is shown in Figure 6.6. One can see that, for short chains, the effective friction determined by Equation 6.13 is in agreement with the hydrodynamic friction $\Gamma = 1/D$ following the Einstein relation (*cf.* Equation 2.29). For longer chains, on the other hand, a significant deviation is observed. The effective friction no longer follows the N^{-m} behaviour of the Einstein relation (with $m \approx 0.63$), but instead tends towards a linear increase in N . The length scale separating both regimes is of the order of the Debye length in the system.

6. Effective charge and effective friction

From this, it is inferred that the effective friction increases due to the counterions close to the chain, which destroy long-range hydrodynamic interactions between distant parts of the polyelectrolyte and thus reduce the shielding effect. Effectively, different chain segments are decoupled. As this effect is strongly related to the counterion density in the vicinity of the chain, it is likewise depending on the Debye length in the system.

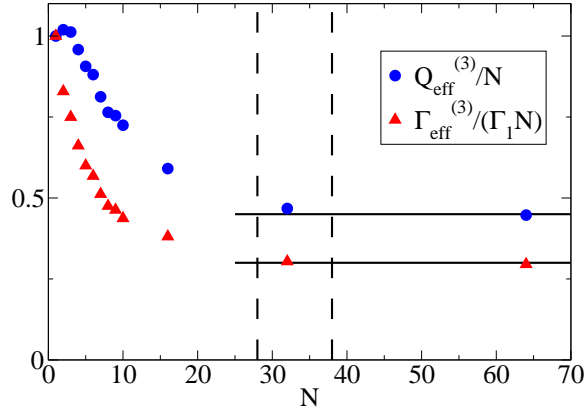


Figure 6.7: The effective charge Q_{eff} and the effective friction Γ_{eff} per monomer show a strong dependence on the chain length N for short chains. For long chains, both values are constant. The transition occurs on a length-scale similar to the Debye length (dashed lines).

This effect becomes more evident when looking at the effective friction per monomer, Figure 6.7. Initially, for short chains, the effective friction decreases strongly with increasing chain length N . The monomers move together through the solvent and can shield each other from the flow, in this way reducing the effective friction they experience with the solvent. For longer chains, this reduction of the effective friction becomes less pronounced.

The effective charge per monomer shows a different behaviour. Short chains do not have any bound counterions and show their bare charge of $1e$ per monomer. With increasing length, they can attract counterions which are then co-moving with the polyelectrolyte and reducing its effective charge.

The combined behaviour of effective friction and effective charge leads to the observed length dependent mobility for short chains and the constant mobility for long chains. The mobility maximum which is observed for flexible polyelectrolytes appears due to the efficient shielding between monomers for short chains, which reduces the effective friction. Stiffer polyelectrolytes experience a stronger friction, since the monomers in rod-like conformations can not shield each other that efficiently. This is the reason why the maximum in the mobility for intermediate

chains is only observable for flexible or semi-flexible polyelectrolytes, such as PSS or single-stranded DNA, but not for the more rigid double-stranded DNA. Moreover, the decrease of the effective charge by counterion attraction depends on the linear charge density of the polyelectrolyte. The higher the polyelectrolyte's charge is, the more the effective charge is reduced by co-moving counterions. Additionally, it is shown that the counterions also increase the effective friction. Both effects work in the same direction and cause the maximum to be shifted to shorter chains (in case of PSS) or disappear completely (for double-stranded DNA).

This study has shown that the concentration of counterions and salt around the polyelectrolyte plays an important role on the electrophoretic behaviour of polyelectrolytes in free-solution. It was illustrated that the relevant length-scale for the hydrodynamic screening is comparable to the Debye length. This effect is explained in detail in the next section.

6.4. Counterion induced hydrodynamic screening

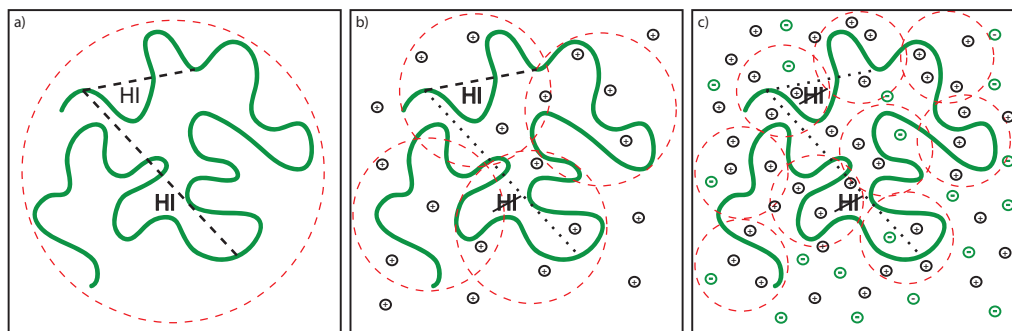


Figure 6.8: The Figure schematically illustrates the influence of surrounding ions on to the long-range hydrodynamic interactions between different parts of a polyelectrolyte chain. a) For an uncharged polymer, the hydrodynamic interactions are unscreened and all chain monomers can interact with each other. This is the basis of the Zimm model (*cf.* Section 2.3.2). b) The anti-correlated movement of the counterions during electrophoresis of polyelectrolytes limits the hydrodynamic interaction. c) The more salt is added to the system, the higher is the ion density in the vicinity of the chain, which reduces the hydrodynamic interaction range even further, so that most parts of the chain appear to be hydrodynamically decoupled.

Figure 6.8 illustrates how counterions and salt in the vicinity of polyelectrolyte chains influence the hydrodynamic interactions during electrophoresis. As explained in the Zimm model (*cf.* Section 2.3.2), the hydrodynamic interactions between different parts of an uncharged polymer chain are unscreened and essentially have an infinite interaction range.

6. Effective charge and effective friction

Figure 6.8a indicates this regime, where all parts of the chain can interact via hydrodynamic interactions. The individual chain segments provide hydrodynamic shielding to each other, so that the fluid feels a combined spherical object (*cf.* Figure 2.6). For polyelectrolytes this picture holds during electrophoresis, as proven by the comparison between Kirkwood-Zimm formula, Eq. 2.36, and the measured diffusion coefficient D in Figure 5.2.

When measuring the electrophoretic mobility, a different phenomenon can be observed: the effective hydrodynamic friction of the polyelectrolyte chain is not directly related to its hydrodynamic size as measured in diffusion experiments anymore, see Figure 6.6. The reason for this is illustrated in Figure 6.8b: during electrophoresis, the counterions within the polyelectrolyte coil move – due to their opposite charge – anti-correlated to the polyelectrolyte. This movement allows the fluid molecules to penetrate into the polyelectrolyte coil. As a consequence, the range of the hydrodynamic interaction gets limited. Like the Debye length for electrostatic screening, the hydrodynamic screening length depends on the ion concentration in the vicinity of the chain. This relation between the electrostatic screening and the hydrodynamic screening length was previously suggested by different authors [154, 155].

The connection between electrostatic screening and hydrodynamic screening can be easily motivated by the following reasoning: the Debye length is the length-scale on which the charge of the polyelectrolyte is screened by the surrounding ions. When looking at this object from the outside, the total force exerted by the applied electric field is zero, *i.e.*, no momentum is transferred to the polyelectrolyte-ion complex. Due to momentum conservation, the interaction with the fluid has to result in a vanishing total force.

The counterions that associate with the polyelectrolyte influence the solvent flow around it, effectively canceling the beneficial shielding effects. When additional salt is added to the system, the like charged salt ions likewise contribute to this effect as shown in Figure 6.8c. The higher the ion concentration is, *i.e.*, the shorter the Debye length is, the shorter is the length scale on which different polyelectrolyte monomers can interact hydrodynamically. On a length scale comparable to the Debye length in the system, different parts of the polyelectrolyte become decoupled. For longer chains, the effective friction per segment does not depend on the length of the polyelectrolyte anymore. Consequently, the effective friction per monomer becomes independent of the length of the polyelectrolyte chain, as seen in Figure 6.7.

6.5. Summary

This chapter provides a microscopic understanding of the effects that lead to the experimentally observed length independent mobility of long flexible polyelectrolytes, which is in agreement with the free-draining picture illustrated in Section 2.5.2. To investigate the dynamic behaviour quantified in Chapter 5, five different approaches

to estimate the dynamic effective charge of the polyelectrolyte-counterion complex during free-solution electrophoresis were introduced.

Two of these estimators are particularly promising. For the charge estimator based on the Langevin model, $Q_{\text{eff}}^{(3)}$, it is only necessary to determine one dynamic quantity, namely the electrophoretic mobility. All other parameters are directly given by the model. In this way one can obtain an accurate estimate without too much computational effort. The ion-diffusion estimator $Q_{\text{eff}}^{(4)}$, on the other hand, requires the calculation of three dynamic quantities, which is slightly more costly in simulation but has the great advantage of being directly transferable to experiments, since all needed quantities, *i.e.*, the free ion diffusion, the bound ion diffusion, and the chain diffusion can be measured by standard techniques. To the author's knowledge, this is the first time this method is proposed to determine the effective charge of polyelectrolytes during electrophoresis.

All estimators show that the effective charge is not influenced by hydrodynamic interactions. Thus, it is possible to use these estimators in simulations without hydrodynamic interactions that are computationally inexpensive.

With these estimators, the length dependence of the effective charge is determined and, combined with the measurements of the electrophoretic mobility, the effective friction of the polyelectrolyte chain is obtained. The results indicate that the effective friction during electrophoresis is different from the hydrodynamic friction for a single polyelectrolyte chain obtained from diffusion measurements. This difference is attributed to the contribution of the co-moving counterions, which influences the hydrodynamic interactions between different chain monomers. On short length scales, the hydrodynamic interactions create a hydrodynamic shielding effect for the polyelectrolyte molecules. On larger length scales, the hydrodynamic interactions between different parts of the polyelectrolyte chain are destroyed. Thus, for compounds of longer chains, the hydrodynamic interactions are screened and the friction becomes linear in terms of the chain length. For these chains, the effective friction per monomer approaches a constant value, which – together with the constant value per monomer of the effective charge – leads to the well-known and observed constant electrophoretic mobility for long polyelectrolyte chains.

It is shown that the length scale of this effect, namely the hydrodynamic screening length, is comparable to the Debye length for electrostatic screening in the system.

7. Size-separation by end-labeled free-solution electrophoresis

The final chapter of this thesis is dedicated to the the electrophoretic separation of polyelectrolytes of varying length in free-solution by means of end-labeled free-solution electrophoresis (ELFSE). The coarse-grained simulation model is used to characterize the drag coefficients of different label types: linear and branched polymeric labels, as well as transiently bound micelles.

After introducing the history and the background of the ELFSE method, it is specifically shown that the label's drag coefficient is determined by its hydrodynamic size, and that the drag per label monomer is largest for linear labels. However, the addition of side chains to a linear label offers the possibility to increase the hydrodynamic size, and therefore the label efficiency, without having to increase the linear length of the label, thereby simplifying synthesis. The third class of labels investigated, transiently bound micelles, seems very promising for the usage in ELFSE, as they provide a significant higher hydrodynamic drag than the other label types.

The results are compared to theoretical predictions, and it is analysed how the efficiency of the ELFSE method can be improved by using smartly designed drag-tags.

7.1. Introduction

As shown in Chapters 5 and 6, the free-solution mobility of a flexible polyelectrolyte chain does not depend on the chain length N anymore if the chain is longer than a certain length N_{FD} . The regime where $N > N_{\text{FD}}$ is called free-draining regime. In this regime, the counterions influence the inter-monomer hydrodynamic interactions and allow the fluid to drain through the polyelectrolyte coil. The effective friction Γ_{eff} becomes linear in the chain length, as does the effective charge Q_{eff} for longer chains, which leads to a constant, length-independent mobility

$$\mu_0 = \frac{\Gamma_{\text{eff}}}{Q_{\text{eff}}}. \quad (7.1)$$

It was shown that attaching a suitable uncharged molecule to an electrophoresis target can restore the size-dependent mobility and overcome the free-draining property of long polyelectrolyte chains [2, 3, 18]. This method, which is known as *end-labeled free-solution electrophoresis* (ELFSE), is based on the alteration of the charge-to-friction ratio of the polyelectrolyte molecules by an uncharged drag label.

7. Size-separation by end-labeled free-solution electrophoresis

The effect of the label can be compared to that of a parachute attached to a moving object. The additional friction provided by the parachute slows the object down. This effect is stronger for smaller molecules with a lower effective friction, as the ratio between charge and friction is changed more drastically than for larger molecules with a naturally higher effective friction.

Since the method's introduction, finding suitable labels that provide a high hydrodynamic drag has been a major concern in this field [156–158]. A larger hydrodynamic drag enables the separation of longer chain fragments, as the length-dependence of the electrophoretic mobility decreases with increasing polyelectrolyte length. When the additional friction provided by the drag-tag becomes negligible against the intrinsic effective friction of the polyelectrolyte, the chain becomes essentially free-draining again. Experimentally relevant is that the mobility of long polyelectrolyte chains should differ by a factor large enough to allow for accurately separating them, although their lengths only vary by a single monomer. The maximum chain length resolvable in this way is called the *read length*.

In general, the drag labels can be chosen from a wide range of molecules but they have to fulfill certain requirements, such as being water-soluble at experimental conditions, having a unique attachment mechanism to the polyelectrolyte and showing minimal interaction with the walls of the capillary. The read length is optimised by choosing a large molecule that imposes a high frictional drag. However, to fulfill resolution requirements, the labels must remain perfectly monodisperse.

As it poses an experimental challenge to produce large, monodisperse linear polymer labels, two recently proposed alternatives seem promising. Haynes et. al. [159] proposed to use branched polymers with well-defined architecture. A first theoretical study on this method [160] verified the approach and concluded that, even though a branched polymer is more compact and thus provides a smaller hydrodynamic friction for a given molecular weight than a linear polymer, this drawback is offset by the monodispersity of the branched labels created by assembling shorter linear chains. Grosser et. al. [161–163] introduced nonionic surfactant micelles as drag labels with very large hydrodynamic friction. The inherent polydispersity of the micelles is overcome by using a PNA amphiphile that only provides a transient binding between the DNA fragments to be separated and the micelles. Each fragment attaches to a different micelle every couple of seconds, which results in an averaging procedure over the course of the elution time that remedies the need for perfect monodispersity. Both methods discussed above can benefit significantly from supporting computer simulations that include hydrodynamic interactions between polyelectrolyte, label and solvent, as well as account for the influence of the electrostatic interaction between the polyelectrolytes and its surrounding counterions.

Since the ELFSE method overcomes the main drawback of ordinary gel electrophoresis, the long separation time due to the slow down by the applied gel matrix, it is a promising method on the way to faster sequencing methods and, as such, of especial interest to the community.

7.2. Theory

The theory for end-labeled free-solution electrophoresis is based on the interplay between the hydrodynamic and the electrostatic forces. In general, only hydrodynamic interactions with the solvent are taken into account, but the ones between the attached drag-tag and the polyelectrolyte are neglected. The coupled electrohydrodynamic interactions are linearised based on the assumption that the conformations and counterion clouds are not deformed. This is valid for small velocities and small electric fields (*cf.* [130, 131], also see Chapter 4).

Neglecting molecular end-effects, the electrophoretic mobility $\mu = v/E$ of the polyelectrolyte with an attached linear drag-tag can be described in terms of the effective friction of the polyelectrolyte Γ_{PE} , its effective charge Q_{PE} and the hydrodynamic friction of the attached label Γ_{L} :

$$\mu = \frac{Q_{\text{PE}}}{\Gamma_{\text{PE}} + \Gamma_{\text{L}}} = \mu_0 \frac{1}{1 + \Gamma_{\text{L}}/\Gamma_{\text{PE}}}, \quad (7.2)$$

where μ_0 is the length independent free solution mobility without drag-tag.

Equation 7.2 shows the importance of the ratio between Γ_{PE} and Γ_{L} . The electrophoretic mobility μ is a function of N for a fixed Γ_{L} as long as Γ_{PE} changes with N and the ratio between Γ_{L} and Γ_{PE} remains non-negligible.

Since Γ_{PE} grows linear with the length of the polyelectrolyte for long chains, as shown in Chapter 6, Equation 7.2 can be reformulated as follows:

$$\mu = \mu_0 \frac{1}{1 + \alpha_{\text{L}}/N}, \quad (7.3)$$

with a constant drag coefficient

$$\alpha_{\text{L}} = \frac{\Gamma_{\text{L}}}{\Gamma_{\text{PE}}/N}. \quad (7.4)$$

The chemistry and temperature dependent α_{L} is a measure for the difference in hydrodynamic properties between the polyelectrolyte and the label [3, 158, 164–166].

In order to characterize the effectiveness of an arbitrary (not necessarily linear) label for size-separation, Equation 7.3 has been used to define this specific label property from the measured mobilities:

$$\alpha_{\text{L}} = N \left(\frac{\mu_0}{\mu} - 1 \right), \quad (7.5)$$

where α_{L} is conveniently determined as the slope when plotting μ_0/μ versus $1/N_{\text{PE}}$:

$$\frac{\mu_0}{\mu} = 1 + \alpha_{\text{L}}/N. \quad (7.6)$$

7. Size-separation by end-labeled free-solution electrophoresis

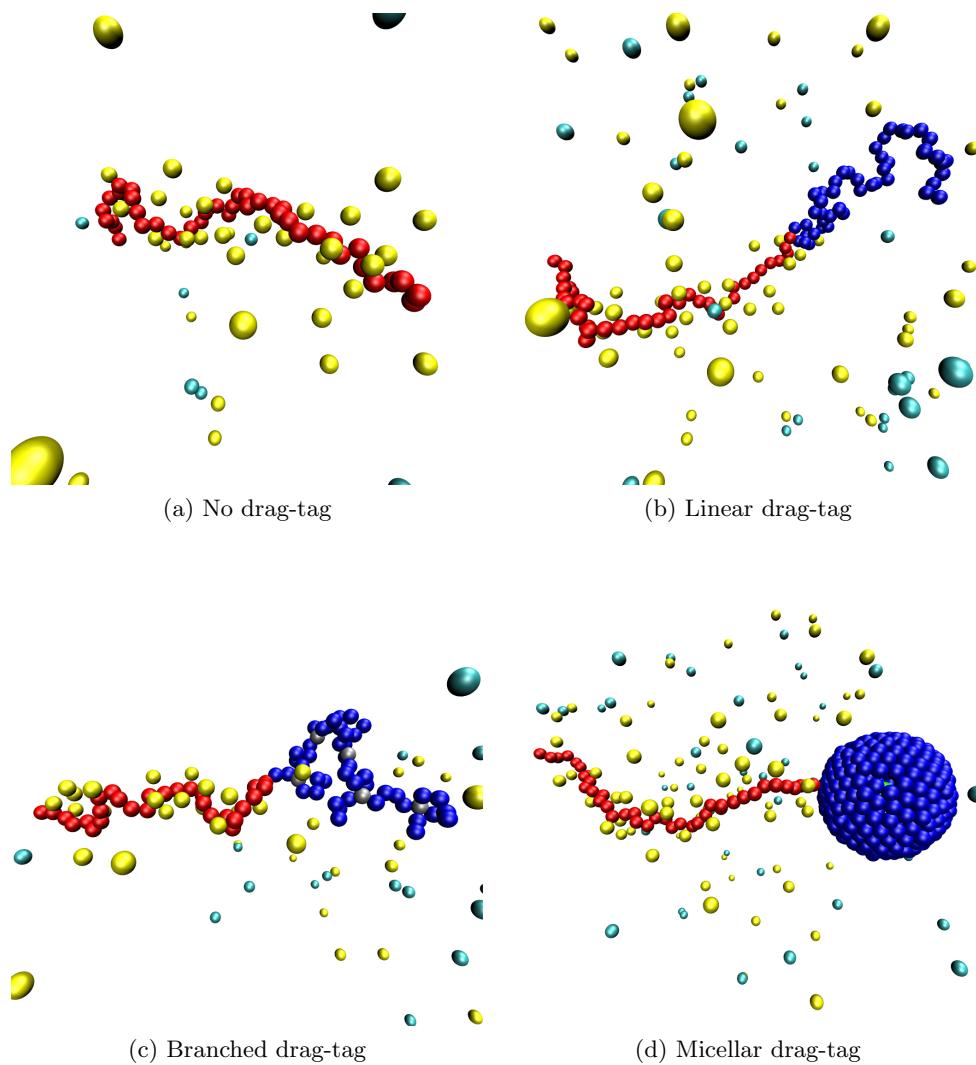


Figure 7.1: (a) Polyelectrolyte with surrounding counter- and co-ions. (b) with linear drag-tag, (c) with branched polymeric drag-tag, and (d) with micellar drag-tag.

7.3. Modelling drag-tags

The coarse-grained molecular dynamics model used in this thesis is extended by the inclusion of the three labels investigated, as shown in Figure 7.1. The linear labels use the same flexible bead-spring model as the polyelectrolytes, but are uncharged. For the study of branched labels, flexible side chains of well-defined length are added to the linear label. The third kind of label, micellar drag-tags, is represented by a sphere of given radius whose surface is modelled by many small WCA spheres that are connected with each other by a network of FENE springs. The number of small spheres is defined by the radius of the large sphere to be modelled. This model has been successfully used to study colloidal electrophoresis [149, 152, 167].

For this study, the length scale is set to $\sigma_0 = 4.7\text{\AA}$, which, with the average bond length along the polyelectrolyte chain of $0.91\sigma_0$, represents a linear monomer distance of approximately 4.3\AA , the distance between two bases of single-stranded DNA [166]. The Bjerrum length is changed to $l_B = e_0^2/4\pi\epsilon k_B T = 1.5$ in simulation units to preserve correspondence to 7.1\AA , the Bjerrum length in water at room temperature.

The electrophoretic mobility is obtained by applying a constant electric field of reduced field strength $E = 0.1$ that acts on all charged particles. The mobility is then given by direct measurement of the center of mass velocity v of the chain:

$$\mu = \frac{v}{E}. \quad (7.7)$$

This approach is different from the method used in the previous chapters on the free-solution mobility of polyelectrolytes, where the Green-Kubo formulation to determine the electrophoretic mobility at zero electric field was used. As this chapter is dedicated to study the behaviour of longer polyelectrolyte chains, the direct measurement of the velocity offers the better trade-off between computational effort and accuracy of the results.

Before applying this method, it was ensured that the applied electric field strength E is small enough not to distort chain conformations or counterion distributions. Therefore, the system is in the linear response regime, *i.e.*, the measured mobility does not depend on the magnitude of the electric field.

The mesoscopic LB fluid uses a kinematic viscosity $\nu = 1.0$ and a fluid density $\rho = 1.0$. The simulations are carried out under periodic boundary conditions in a cubic simulation box. The behaviour of polyelectrolyte chains varying from $N = 20$ to $N = 60$ monomers is investigated. The size L of the box is varied in order to maintain a constant monomer density of $n_{PE} = 10^{-3}$, which corresponds to a concentration $c_{PE} = 16\text{mM}$. The same concentration is used for the additional salt, resulting in a Debye length of $\lambda_D \approx 4.2$.

Up to ten independent simulations are carried out for each data point, taking between one day and two weeks on a single standard CPU¹ depending on the chain length N and the type of label investigated.

¹Dual Core AMD Opteron(tm) Processor 270

7.4. Linear drag tags

In this section, the simulation model is applied to the electrophoresis of polyelectrolyte chains with an attached linear polymeric drag-tag. The electrophoretic mobility for polyelectrolyte chains is determined with and without different labels, and the results are compared to the theoretical predictions.

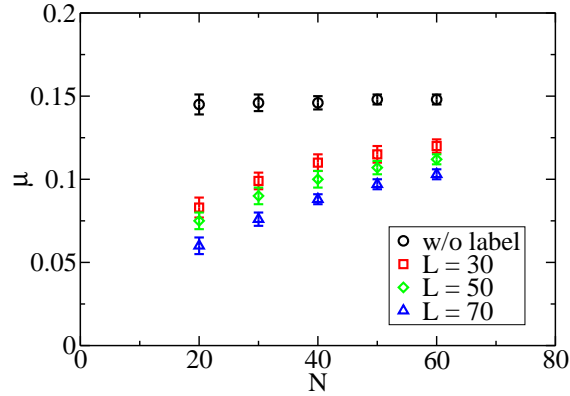


Figure 7.2: The free-solution electrophoretic mobility without label (black circles) shows no dependence on the chain length N . The free-draining mobility is $\mu_0 = 0.147 \pm 0.002$. The attachment of linear drag-tags to the end of the polyelectrolyte chains reduces the mobility and restore a N -dependent behaviour. The label length L is varied from 30 to 70 monomers, with the largest label resulting in the strongest slowdown.

First, the free-solution electrophoretic mobility without an attached drag-tag, μ_0 , is determined, as shown in Figure 7.2. The measured mobility does not depend on the chain length, as expected for longer free-draining polyelectrolyte chains. The average mobility is determined to be

$$\mu_0 = 0.147 \pm 0.002. \quad (7.8)$$

Additionally, in Figure 7.2, the mobilities with attached drag-tags ranging from $L = 30$ to $L = 70$ monomers are measured, and it is confirmed that a length-dependence is achieved and that the difference in mobilities, *i.e.*, the resolution of the separation, is bigger the longer the attached label is. Equation 7.6 is used to calculate the hydrodynamic drag coefficients as shown in Figure 7.3, resulting in values from $\alpha_L = 13.5 \pm 0.4$ for $L = 30$ to $\alpha_L = 25.7 \pm 0.6$ for $L = 70$.

In the following, an expression for α_L based on the hydrodynamic size and shape of the label is developed. The hydrodynamic friction Γ_L of the uncharged label is related to the hydrodynamic radius R_h by means of the Stokes relation:

$$\Gamma_L = 6\pi\eta R_{h,L}. \quad (7.9)$$

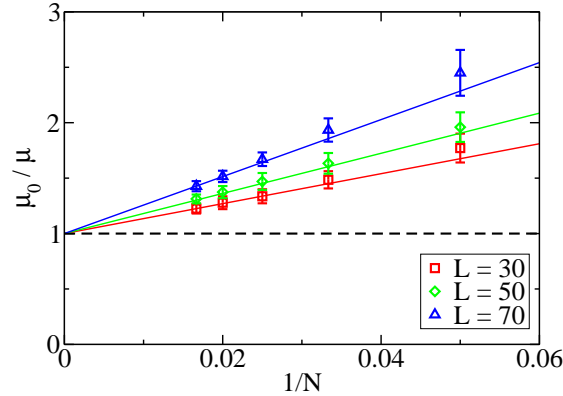


Figure 7.3: The hydrodynamic drag coefficient α_L is given by the slope of the curve. For the linear labels, α_L ranges from 13.5 to 25.7.

As in the previous chapter, the effective friction of the polyelectrolyte is expressed in terms of the free-solution mobility μ_0 and the effective charge Q_{eff} :

$$\Gamma_{\text{PE}} = Q_{\text{eff}}/\mu_0. \quad (7.10)$$

Using the Manning prediction $Q_{\text{eff}} = 1/\xi N$ for the effective charge finally yields

$$\alpha_L = \mu_0 \xi 6\pi\eta R_{\text{h,L}}. \quad (7.11)$$

With the system parameter used here, $\xi = l_{\text{B}}/b = 1.63$, one obtains

$$\alpha_L = (4.5 \pm 0.1) R_{\text{h,L}}. \quad (7.12)$$

Equation 7.11 will be shown to be valid for linear labels whose size is not exceeding the Debye length λ_{D} . When the label size becomes larger, the friction of the label is not anymore directly related to the hydrodynamic radius, as the salt ions that penetrate the polymer coil influence the intermonomer hydrodynamic interactions and limit them to the hydrodynamic screening length. As for the polyelectrolyte itself, this screening length is of the order of the Debye length.

For linear labels larger than the Debye length, McCormick *et al.* introduced a relation for the hydrodynamic drag coefficient, with which α_L can be determined from the size of the polyelectrolyte and label monomers, b_{PE} and b_{L} , and the corresponding Kuhn lengths, $b_{\text{k,PE}}$ and $b_{\text{k,L}}$, which describe the stiffness of the chains [165]:

$$\alpha_L = \frac{b_{\text{L}} b_{\text{k,L}}}{b_{\text{PE}} b_{\text{k,PE}}} L. \quad (7.13)$$

The derivation of Equation 7.13 assumes that the polyelectrolyte and the label can be represented by a series of hydrodynamically equivalent entities, called “blobs”

7. Size-separation by end-labeled free-solution electrophoresis

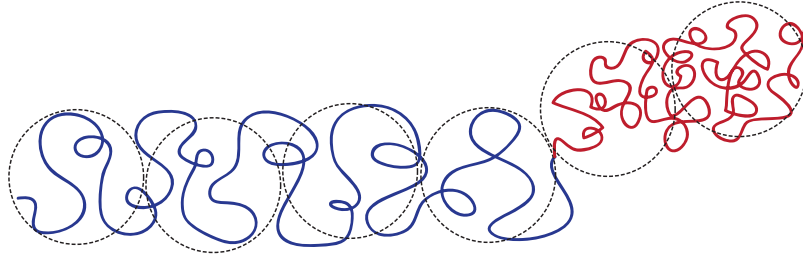


Figure 7.4: Scheme of the “blob” picture used to derive Equation 7.13. The circles represent the blobs with a size comparable to the Debye length λ_D . Hydrodynamic interactions are screened beyond the size of the blobs.

as shown in Figure 7.4. The number and the size of these blobs depend on the bond length and flexibility of the chain, resulting in the presented relation for α_L .

The total effective friction of the polyelectrolyte-label compound with the surrounding solvent is linear in the total number of hydrodynamically equivalent blobs given by

$$N = N_{\text{PE}} + \alpha N_L. \quad (7.14)$$

This is true for long polyelectrolytes in the free-draining regime, where the size of the compound is larger than the Debye length λ_D , since the hydrodynamic interactions between the individual monomers are screened on this length scale, as shown in Chapter 6.

Thus, the hydrodynamic drag α_L can be directly calculated from the persistence lengths of the polyelectrolyte and of the label using Equation 7.13. Here, $l_{\text{p,PE}}$ and $l_{\text{p,L}}$ are calculated from the bond correlation function [168]:

$$l_p = \frac{1}{2b} \sum_{i=0}^{N/2} \langle \vec{b}_{N/2} \cdot \vec{b}_{N/2+i} + \vec{b}_{N/2} \cdot \vec{b}_{N/2-i} \rangle, \quad (7.15)$$

where \vec{b}_i is the i -th bond vector and b is the average bond length. The angular brackets $\langle \dots \rangle$ denote an ensemble average.²

Under the chosen conditions, the persistence length of the polyelectrolyte is found to be

$$l_{\text{p,PE}} = 5.1 \pm 0.3,$$

and the label’s one

$$l_{\text{p,L}} = 1.9 \pm 0.1.$$

²For a discussion about different ways to determine the persistence length in computer simulations please refer to Reference 169.

In our model, all monomers have the same size, so that Equation 7.13 is reduced to

$$\alpha_L = \frac{l_{p,L}}{l_{p,PE}} L = (0.37 \pm 0.03) L. \quad (7.16)$$

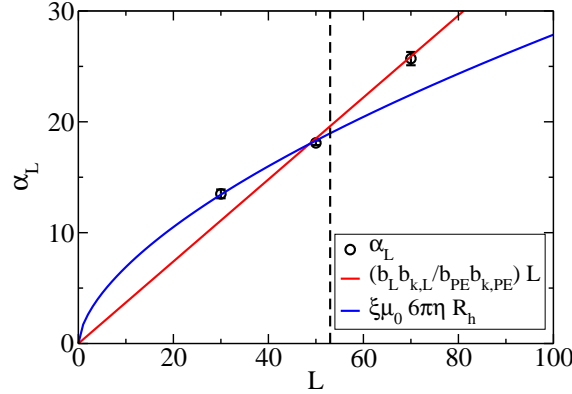


Figure 7.5: The hydrodynamic drag coefficient α_L for the linear label is compared to the theoretical predictions of Equations 7.11 and 7.13. Both predictions are valid in different regimes with the division being $R_h \approx \lambda_D$ indicated by the vertical dashed line. Note that neither theory has a free fitting parameter used to achieve the quantitative agreement with the simulation data.

The comparison between the measured drag coefficient and the theoretical prediction in Figure 7.5 shows an agreement for the respective regimes of validity and underlines the applicability of the chosen simulation model for this problem. For labels with a hydrodynamic size smaller than the Debye length, *i.e.*, $R_h < \lambda_D$, Equation 7.11 gives the correct prediction for the drag coefficient α_L . Longer labels, however, can no longer be seen as a single polymer coil with a hydrodynamic size R_h , but instead the blob picture described by Equation 7.13 has to be used. This prediction is only valid when the hydrodynamic size becomes larger than the Debye length. For $R_h \approx \lambda_D$ a cross-over between both predictions is observed.

It remains to be emphasised that, by determining α_L from the measurements of the persistence lengths and the hydrodynamic radius, there is *no free* fitting parameter and the *quantitative* agreement in Figure 7.5 is noteworthy.

7.4.1. Increasing the hydrodynamic drag coefficient

In Figure 7.5, it is shown that the total drag coefficient α_L for linear labels can be increased by using longer labels, and that beyond the Debye length the increase is linear with the length L of the label. Unfortunately, the experimental requirement

7. Size-separation by end-labeled free-solution electrophoresis

of strict monodispersity of the label limits the size of linear polymeric labels that are synthesizable. In this section, it will be shown how one can influence the total drag coefficient also by modifying the relative stiffness of the polyelectrolyte chain and the label.

Increasing the label stiffness

Equation 7.13 shows the dependence of α_L on the persistence lengths of polyelectrolyte and label. Therefore, α_L can be increased by either increasing the persistence of the label or decreasing the persistence of the polyelectrolyte. Both ways are shown here.

First, an additional harmonic bond angle potential,

$$U_{BA} = k_{BA} (\phi - \phi_0)^2, \quad (7.17)$$

is added to the interaction between the label monomers, where ϕ is the angle between two consecutive bonds. Here, $k_{BA} = 30$ and $\phi_0 = 0$ are chosen.

The bond angle potential increases the hydrodynamic radius of the 30 monomer label to

$$R_{h,L} = 5.25 \pm 0.05,$$

and thus puts the label size into the regime where the blob picture is valid. The increased stiffness doubles the persistence length of the label to

$$l_{p,L} = 4.0 \pm 0.1,$$

which yields an increased drag coefficient according to Equation 7.13 of:

$$\alpha_L = (0.79 \pm 0.04) L \approx 23.7.$$

Figure 7.6 compares the theoretical predicted slowdown of the stiffer 30 monomeric label to the measured mobilities. As before, a good agreement to the theory is found for the investigated label lengths.

Reducing the polyelectrolyte stiffness

Now, the amount of additional monovalent salt is increased from a concentration of $c_S = 16mM$ to $c_S = 1M$, thereby significantly reducing the Debye length of the system to $\lambda_D \approx 0.65$, making the blob picture fully applicable.

The increased electrostatic screening reduces the extension of the polyelectrolyte chain and reduces the contribution of electrostatics to the persistence length, which is determined to be

$$l_{p,PE} = 3.8 \pm 0.2,$$

whereas the label persistence is unaffected. Thus, one obtains a hydrodynamic drag coefficient of

$$\alpha_L = (0.50 \pm 0.04) L.$$

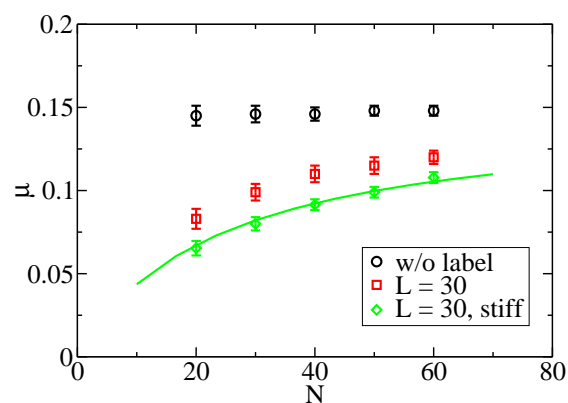


Figure 7.6: The hydrodynamic drag coefficient of a stiff linear label is higher than that of a fully flexible label with the same length. The slowdown of the stiff label is correctly predicted by Equation 7.13 (solid line).

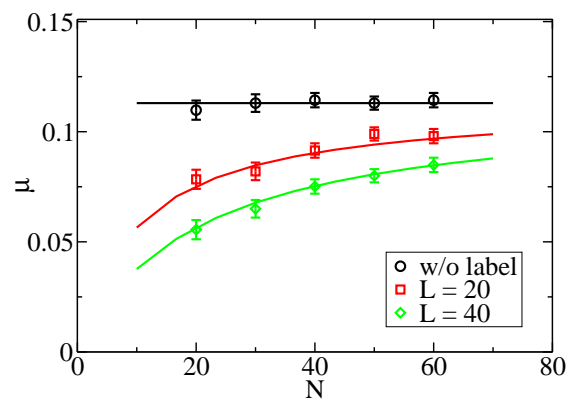


Figure 7.7: In the presence of 1 Mol additional salt, the persistence length of polyelectrolyte is reduced, changing the relative hydrodynamic drag α_L of the label. The measured mobilities for two linear labels of length 20 and 40 are compared to the prediction using Equation 7.13.

7. Size-separation by end-labeled free-solution electrophoresis

The change in electrophoretic mobilities for a label of length $L = 20$ and $L = 40$ can be seen in Figure 7.7. Please note that the free-draining mobility μ_0 also changes due to the fact that the additional salt also increases the screening of the polyelectrolyte charge, thus reducing the force from the external field:

$$\mu_0 = 0.113 \pm 0.002.$$

This reduction of the electrophoretic mobility has a negative impact on the size-selectivity of the separation, because the absolute difference between the mobilities of polyelectrolyte chains of different length is reduced. Consequently, an increased hydrodynamic drag coefficient is less effective when achieved by adding additional salt.

In conclusion, it has been found that, while it might be easier to influence the persistence length of the polyelectrolyte to be analysed by the addition of salt, a better size-selectivity can be achieved when a suitable stiff label with high persistence length is used. In any case, it was demonstrated that the hydrodynamic drag coefficient can be significantly increased without changing the label length.

7.5. Branched drag tags

In this section, it will be investigated if branched polymeric labels can be used as efficient drag-tags for ELFSE. First, the results obtained in a recent experimental study by Haynes *et al.* are briefly reviewed [159]. The study compared a linear polypeptide drag-tag with 30 repeat units to two branched drag-tags, each with 5 side-chains spaced evenly along a 30 unit-long backbone. The two different branched labels had 4 and 8 monomer long side-chains. The drag coefficients α_L were obtained by measuring the mobility of two different DNA fragments of 20 and 30 bases length. It was found that the value of α_L increases roughly linearly with the molecular weight of the branched label.

This astonishing observation was theoretically analysed by Nedelcu *et al.* [160]. It was shown that the drag coefficient is directly related to the hydrodynamic radius, and that the linear dependence on molecular weight is only true in the limit of short side chains.

Furthermore, the drag provided by a linear label is always higher than that provided by a branched label of the same molecular weight. The reason for this is that, with a fixed length backbone, a branched polymer is essentially a compact star polymer with a smaller hydrodynamic size than the linear equivalent. Indeed, as the number of arms increases, the branched polymer becomes even more compact and less favorable for ELFSE.

Based on the observations, the following optimal design is proposed when using branched polymeric labels for ELFSE: I) side chains with length comparable to the distance between branching points, or II) two long branches located near the ends of the molecule's backbone.

Here, the focus will be on investigating the effect of the length of the side chains for a polymeric drag-tag with a fixed backbone length. Similar to the structure of the label used by Haynes *et al.*, the label has a backbone of $L = 30$ monomers to which 5 side chains are attached evenly spaced along the backbone. The side-chain length is varied from 2 to 8 monomers, so that the total number of monomers in the label ranges from 40 to 70. The drag coefficient of the labels is determined by measuring the electrophoretic mobility of polyelectrolyte chains from $N = 20$ to $N = 60$.

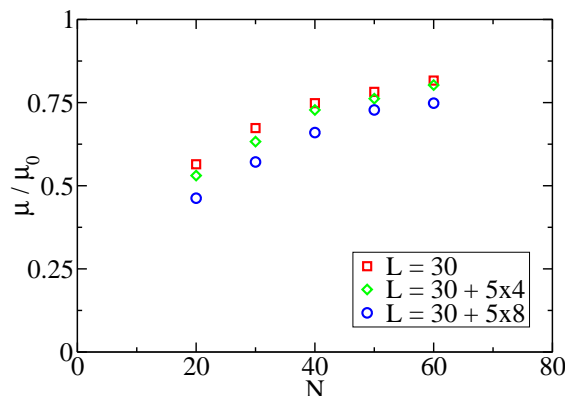


Figure 7.8: The reduced mobility μ/μ_0 for polyelectrolytes with an attached linear label with side chains of length 4 and 8 shows a more pronounced slowdown than for the label without side chains.

Figure 7.8 shows the simulation results for a 30 monomeric label without side chains and with the tetra and octamer side chains. To analyze the hydrodynamic drag of the branched labels in detail, α_L is determined according to Equation 7.6. The obtained α_L values are compared to the corresponding value of a purely linear drag-tag with the same number of monomers.

Figure 7.9 confirms the work by Nedelcu, showing that the label with the highest drag per monomer is the linear label. For the same number of monomers L , the hydrodynamic drag coefficient α_L of the linear label is higher than that of the branched one. But it also shows that the addition of side chains can be used to increase the hydrodynamic drag of the label. This is attributed to two effects: firstly, the hydrodynamic size of the label is increased as the side chains extend from the label. Of similar importance is the second effect, namely that the side chains stiffen the label due to steric repulsion with the backbone, increasing the overall persistence length and increasing the linear length of the backbone.

The drag coefficients obtained for the labels show a scaling with the hydrodynamic radius R_h , as given by Equation 7.11. Since the polymer coil formed by

7. Size-separation by end-labeled free-solution electrophoresis

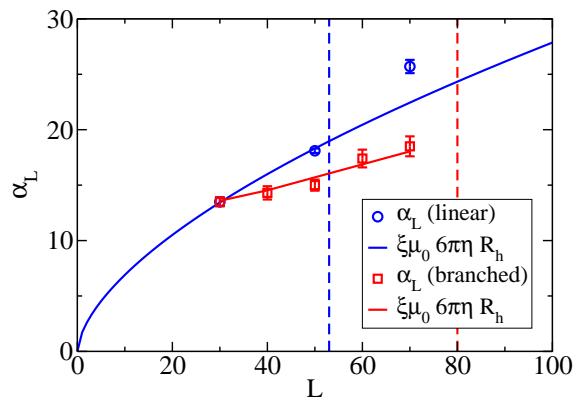


Figure 7.9: The hydrodynamic drag coefficient α_L of a branched polymeric label is compared to the previously determined drag of a linear label. L is the total number of monomers. As long as the hydrodynamic radius R_h of the label is smaller than the Debye length λ_D , the α_L is given by Equation 7.11. The vertical lines indicate the number of monomers L for which $R_h(L) \approx \lambda_D$ obtained from simulations.

the branched label is more compact, it is less penetrated by ions and, therefore, the prediction of Equation 7.11 remains valid for a higher number of monomers compared to the linear label.

The experimentally observed linear scaling with L can be attributed to seemingly linear relationship between R_h and L , but, as Nedelcu *et al.* have shown before, this is only true in the case of side chains smaller or equal to the spacing along the backbone. The only relevant quantity in all cases is the hydrodynamic radius and its contribution to the hydrodynamic drag, as formulated in Equation 7.11.

Although linear labels remain preferable as long as the pure hydrodynamic drag coefficient α_L per molecular weight is concerned, branched polymers offer practical advantages because of the possibility of synthesizing larger monodisperse molecules in a simple, stepwise way.

7.6. Micellar drag tags

Recently, Grosser *et al.* [161, 163] proposed another promising class of drag-tags that in principle can provide very large hydrodynamic drag coefficients α_L . They used nonionic surfactant Triton X-100 micelles that attach to PNAA-tagged DNA strands. The micelles are water-soluble and are created and destroyed on a timescale of milliseconds to seconds, forming a fairly monodisperse populations of structures with a tunable size and morphology. During the whole electrophoresis time, a single DNA strand attaches to a large number of different micelles. Of importance for the

ELFSE application is the fact that this leads to an averaging effect between micelles of different size for the individual DNA strand, meaning the DNA can be thought of as having a drag tag of fixed size $\langle R \rangle$, where $\langle R \rangle$ is the average micelle size. Only with this averaging, the natural polydispersity of the micelles is overcome and a measurement with a size resolution up to a couple of base pairs is possible.

As a free DNA strand quickly attaches to a new micelle, the DNA is bound to a micelle most of the electrophoresis time. Consequently, the transiently bound micelles provide about the same hydrodynamic drag as a covalently bound drag-tag of similar size would provide. The reported α_L values range between 33 and 58 for a single micelle, depending on the micelle type and the PNAA molecule used for connecting to the DNA strand. Savard *et al.* [163] showed that dual-tagging of the DNA, *i.e.*, attaching a PNAA molecule to both ends of the DNA strand so that two micelles are transiently bound can increase the hydrodynamic drag even further.

In this study, four different micelles with radius $R = 2$ to $R = 5$ are attached to polyelectrolyte chains of different length. Neither the attaching and detaching process or the forming of the micelles themselves is modelled explicitly, but only the hydrodynamic drag of a covalently bound spherical drag-tag is investigated. The results by Grosser and Savard show that the polyelectrolyte is in fact attached to micelles for most of the time and only spends a small fraction of time without drag-tag. As the micelle size can be exactly chosen in simulations, the averaging procedure resulting from the attaching and detaching process does not need to be included.

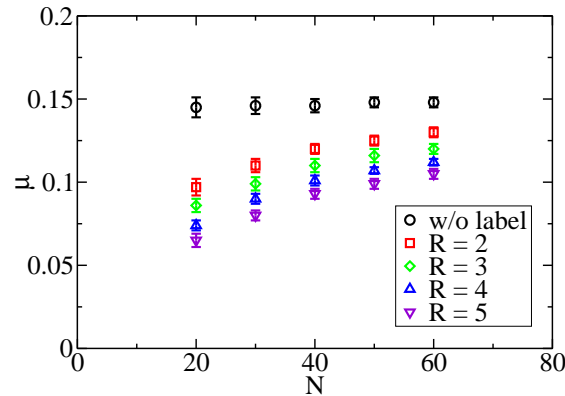


Figure 7.10: The electrophoretic mobility μ as a function of the polyelectrolyte length N becomes size dependent when a micellar drag-tag is attached. The strength of the slowdown depends on the radius R of the micelle.

7. Size-separation by end-labeled free-solution electrophoresis

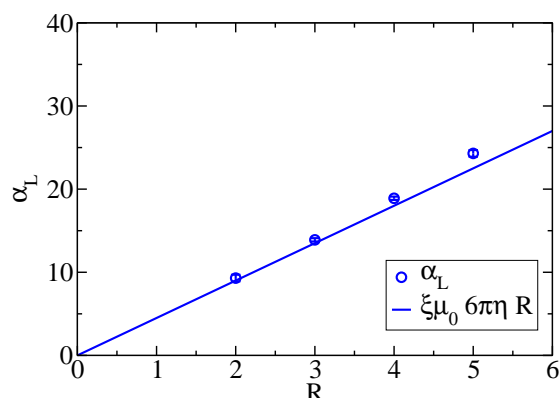


Figure 7.11: The hydrodynamic drag coefficient α_L of a micellar drag-tag is directly proportional to the radius R . The Equation 7.11 gives a very good prediction of the drag coefficient for all tested micelles.

Figure 7.10 shows that micellar drag-tags can be successfully used for electrophoretic separation of polyelectrolyte chains. The values for α_L are obtained as before and compared to Equation 7.11, which correctly predicts the observed behaviour. With the chosen radius of the micelle of $R = 5$, drag coefficients up to $\alpha_L = 24.3$ are achieved.

The results show that the hydrodynamic drag is directly depending on the size of the micelle, as can be seen in Figure 7.11. A linear increase with the radius is observed, as expected from Stokes theory. Again, Equation 7.11 give a correct prediction of the drag coefficient, clearly indicating that only the hydrodynamic size of the drag-tag is important, not the number of units it is made of or the weight associated with it.

The author strongly believes that the use of micellar drag-tags has great potential for the further advancement of end-labeled free-solution electrophoresis. Especially the tunable size makes them ideal candidates, as the drag coefficient can be optimised to the lengths of polyelectrolyte fragments to be analysed.

7.7. Summary

This chapter presented a detailed study of end-labeled free-solution electrophoresis using various hydrodynamic drag-tags by coarse-grained molecular dynamics simulations. Linear, branched and micellar drag-tags were investigated. The simulations support the theoretic predictions and can be matched qualitatively to it. This enables the use of computer simulation as a tool to support the design of improved

hydrodynamic drag-tags usable for electrophoretic separation of polyelectrolytes in free-solution.

It was specifically shown that the drag coefficient of the label is determined by its hydrodynamic size. The hydrodynamic drag per label monomer is largest for linear labels, but experimental restrictions in the synthesis of such labels and the monodispersity requirement limit their practical applicability.

The addition of side chains to a linear label offers the possibility to increase the hydrodynamic size without having to increase the linear length of the label. The synthesis process creates perfectly monodisperse labels. It was shown that the label efficiency is increased with the length of the side chains. In addition to increasing the lateral size of the drag-tag, the side chains also increase the persistence of the backbone and thus contribute two-fold to the increased hydrodynamic size. Especially the steric stabilisation of the linear backbone is responsible for an initial increase of the drag-coefficient with the total number of monomers of the label, *i.e.*, with the molecular weight. For longer side chains, the lateral contribution to the hydrodynamic radius becomes more important.

The third class of labels investigated seems very promising for usage in ELFSE. Transiently bound micelles provide a significant higher hydrodynamic drag, as they can be synthesised with a large hydrodynamic radius. Additionally, the time averaging by attaching to many different micelles over the electrophoresis time span helps to meet the monodispersity criteria. This study showed that the hydrodynamic drag is directly proportional to the hydrodynamic radius of the micelle. The efficiency of this method is, in principle, only limited by the size of labels that can be synthesised.

The results demonstrate convincingly that theory and computer models can support the experimental progress towards the design of novel improved drag-tags, thereby extending the applicability of the ELFSE technique.

8. Outlook: Other free-solution separation methods

The field of electrophoresis constantly produces new ideas on how to improve the separation of polyelectrolytes in terms of accuracy and speed. This chapter provides a brief outlook on two different free-solution separation techniques that are in principle treatable by state-of-the-art computer simulations such as the simulation model used in this thesis. Recent results show how the development of new methods can be supported by such computer simulations. Further promising approaches are reviewed in References 69, 71 and will not be discussed here.

8.1. Surface electrophoresis

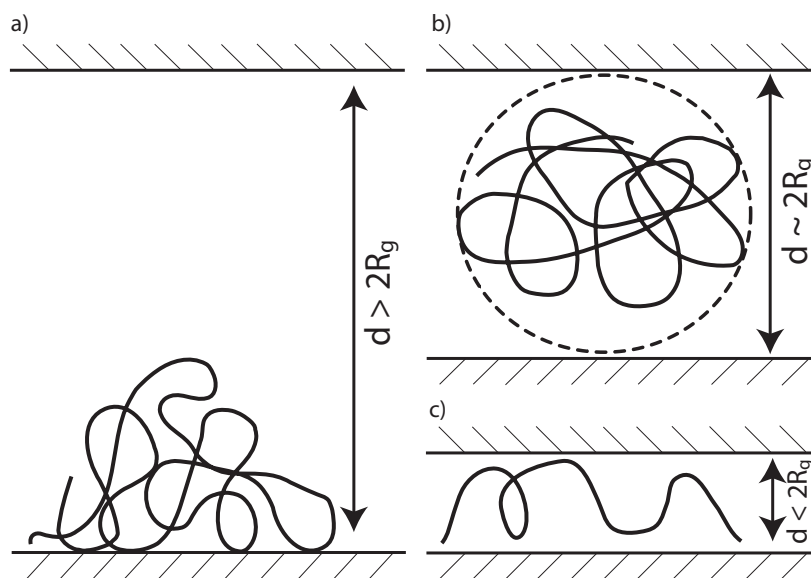


Figure 8.1: Different regimes of confinement used in some gel-free separation techniques: a) weak confinement ($d > 2R_g$) in the presence of an attractive surface, b) strong confinement ($d \sim 2R_g$) that starts to influence the chain conformations, and c) extreme confinement ($d < 2R_g$) in which the chain conformations are determined by the walls of the channels.

8. Outlook: Other free-solution separation methods

A novel electrophoretic separation technique based on the DNA's interaction with a surface was first reported by Pernodet et. al. [11] in 2000. By adsorbing DNA to a surface, length dependent separation on a flat surface without any restrictions or any sieving matrices was achieved (see Fig. 8.1a). It was found that the interactions between the molecule and the substrate essentially act as a length dependent source of friction, enabling electrophoretic separation. The initial experimental observations were accompanied by MD simulations [12, 170] and have been followed up by further studies [171, 172] under different conditions. The results showed that the DNA-surface interaction is a key parameter for the process: a strong attraction leaves the molecules fully adsorbed and no separation is possible, while a too weak attraction lets molecules desorb and resume bulk behaviour, where likewise no separation is possible. Additionally, the interaction can be noticeably influenced by choosing a specially patterned surface [173, 174], an exciting and unique approach for designing optimised and custom-made separation systems.

Since the exact nature of the interaction and the resulting separation mechanism remain elusive at this point, there is a pressing need for more elaborate theoretical studies that include electrostatic and hydrodynamic effects alike, as they are crucial when the molecules approach the surface. This has been neglected so far.

8.2. Confinement-driven separation

Recent progress in design and fabrication of microfluidic devices on a sub-micrometer length-scale [175–177] demands a good understanding of the statics and dynamics of the polyelectrolytes under steric confinement. Several regimes of confinement can be distinguished. In a device that is much larger than the size of the polyelectrolytes, given by its radius of gyration R_g , the conformations are unperturbed and isotropic (weak confinement). Reducing the dimensions of the devices to the order of R_g , the conformations of the polyelectrolytes start to become restricted by the walls, and show deviations from the equilibrium (strong confinement, see Fig. 8.1b). With further reduction of the device size, the polyelectrolyte becomes extremely restricted and the static and dynamic properties undergo significant changes [178, 179] (Fig. 8.1c).

The decrease in size of microfluidic devices used in actual experiments and the growth in size of the systems that are addressable by means of computer simulations - due to advancement of simulation methods together with the increase of computer power - led to a cross-over, creating systems that can be worked on from both sides. Recent experiments in slit-like nano channels studied the static and dynamic properties of single molecules and showed how confinement can be used as a tool to change polymer conformations as well as the dynamics through modulation of the hydrodynamic interactions [180–186]. Consequently, the role of hydrodynamic interactions in confinement has been the focus of several recent computer studies [186–194]. The results indicate that, under weak confinement, the hydrodynamic interactions between polymer and wall drive the polymer to the

center of the channel if an external flow is applied. However, in high confinement, a migration towards the channel walls was observed. Since this interesting physical phenomenon depends on the ratio between the size of the polymer and the width of the channel as well as on the strength of the driving force, it seems to be an ideal candidate for free-solution separation of polyelectrolytes. Recently reported measurements on the diffusion and the electrophoretic mobility of DNA in strongly confined systems [195–197] indicate a possible electrophoretic separation mechanism based on the modified dynamics in strong confinement. A systematic simulation study of this subject has yet to be done in order to verify these results. In particular, electrostatic interactions and the influence of counterions on the hydrodynamic interactions have been neglected so far, but they should be assumed to be of great importance if the length scales of the system become comparable to the Debye length, below which electrostatic interactions are not fully shielded by the solvent [193, 198].

9. Concluding remarks

Detailed studies of the importance of hydrodynamic interactions during free-solution electrophoresis of linear polyelectrolytes by means of coarse-grained molecular dynamics simulations including full electro-hydrodynamic interactions have been presented. The presented simulation model was shown to be fully capable of reproducing the theoretically predicted static conformations of polyelectrolyte chains and their experimentally observed dynamic behaviour, including a maximum in the free-solution electrophoretic mobility of flexible polyelectrolytes that was previously not understood from a theoretical point of view.

A rigorous analysis isolated the two decisive properties of the polyelectrolyte-counterion complex that govern the electrophoretic behaviour: the total effective charge and the total effective friction. These two terms have been defined more precisely and more concisely than they are commonly used, which allowed for a separated analysis of both quantities, explaining the complex dynamic behaviour of charged macromolecules. The main result shows that both quantities, friction and charge, ultimately exhibit a linear dependence on the length of the polyelectrolyte, resulting in a length-independent mobility for long chains.

The understanding of the underlying process paved the way not only for investigating the electrophoresis of single polyelectrolytes, but also for studying compounds consisting of a polyelectrolyte and an attached drag-tag as they are used for end-labeled free-solution electrophoresis. The contribution of various drag-tags to the total effective friction based on their hydrodynamic size has been studied. It was confirmed that recently suggested branched polymeric and micellar drag-tags offer properties suitable for efficient separation of polyelectrolytes using end-labeling.

The main results and observations of this work contribute to the theoretical understanding of polyelectrolyte electrophoresis. It was found that the static chain properties are not influenced by the presence of hydrodynamic interactions and that the expected scaling behaviour of the chain conformations is observed. Specifically, the influence of additional salt on the scaling exponent due to electrostatic screening was shown. The influence of the strength of an applied external electric field on the chain conformations and the counterion cloud was analysed and, below a critical value, no dependence on the field strength was observed, which is in agreement with linear response theory. The application of field strengths above the critical limit changes the static and dynamic properties of the polyelectrolyte. The threshold identified in this study is on a par with theoretical predictions.

The study of the transport properties of short PSS chains showed that the results of two different experimental approaches, namely, capillary electrophoresis and pulsed-field gradient NMR, can be quantitatively matched by the simulation data.

9. Concluding remarks

Excellent agreement is achieved as long as the simulation model correctly includes long-range hydrodynamic interactions. When these interactions are absent, the description of the short-length scale behaviour of the PSS diffusion coefficient and of the electrophoretic mobility fails completely. The findings of this thesis demonstrate convincingly that the transport coefficient of short polyelectrolytes can be quantitatively modeled by coarse-grained simulation techniques. To first order, no chemical details are needed to explain the experimental results.

The novel charge estimators introduced to investigate the dynamics even further are, on the one hand, computationally inexpensive, as they are correct even without the inclusion of hydrodynamic interactions. On the other hand, the estimator based on the measurement of the ion diffusion coefficient is at the same time directly transferable to experiments and can be measured by standard techniques. To the author's knowledge, this is the first time this method is proposed to determine the effective charge of polyelectrolytes during electrophoresis. This opens numerous new opportunities to investigate the dynamic behaviour of charged macromolecules and provides a handle to a previously non-accessible physical quantities of the system.

Using these estimators, the length dependence of the effective charge was studied and, combined with the measurements of the electrophoretic mobility, the effective friction of the polyelectrolyte was obtained. The results indicate that this effective friction during electrophoresis is different from the hydrodynamic friction for a single polyelectrolyte chain obtained from diffusion measurements. This difference is attributed to the contribution by the co-moving counterions, which cause a shielding of the hydrodynamic interactions.

A hydrodynamic screening length was identified, beyond which the effective friction approaches a constant value per monomer, which - together with the constant value per monomer of the effective charge - leads to the well-known and observed constant electrophoretic mobility for long polyelectrolyte chains. Furthermore, the previously not understood mobility maximum can be likewise attributed to this screening effect. The identification of the Debye length as the relevant length scale, for electrostatic and also for hydrodynamic screening, not only provides a concise description of the results presented in this thesis, but also proves the correctness of assumptions made in the theories describing electrophoresis. The direct proof of the free-draining assumption that is used to explain the length-independent mobility of long polyelectrolyte chains underlines the importance of this work.

The hydrodynamic drag of an uncharged molecule with the solvent can be successfully used to restore the size-dependent mobility of polyelectrolytes in free-solution using the ELFSE technique. This study showed that various classes of hydrodynamic drag-tags can be employed, but specifically revealed that the decisive property is the hydrodynamic drag which is directly related to the hydrodynamic size of the label. However, when linear polymeric labels are employed, the screening of hydrodynamic interactions by charged ions in the system results in an effective hydrodynamic drag coefficient for the label that is linear in the contour length of the label.

As such, the hydrodynamic drag per monomer is largest for linear labels, but experimental restrictions in the synthesis of such labels and the monodispersity requirement limit their practical applicability. The addition of side chains to a linear label offers the possibility to increase the hydrodynamic size without having to increase the linear length of the label, which simplifies the synthesis process and creates perfectly monodisperse labels. Although only recently introduced, transiently bound micelles, the third class of labels investigated, seems very promising for usage in ELFSE. They provide a significant higher hydrodynamic drag than the other drag-tags, as they can be synthesised with a large hydrodynamic radius. This study showed that the hydrodynamic drag is directly proportional to the hydrodynamic radius of the micelle, and that the efficiency of this method is, in principle, only limited by the size of labels that can be synthesised.

The characterisation of the dynamic effective friction of macromolecules based on the direct measurement of their effective charge seems to be a promising tool to investigate and understand systems related to the ones studied in this work. The author strongly believes that theory and computer models can support the experimental progress towards the design of novel improved drag-tags, thereby extending the applicability of the ELFSE technique. Likewise, they can be used to develop other matrix-free separation techniques that make use of the changed hydrodynamic interactions in confined geometries. The study of these problems will greatly benefit from the results of this thesis and will ultimately lead to a more profound understanding of soft matter as a whole.

The results of this work provide an in-depth understanding of the microscopic processes that govern the macroscopic behaviour of charged polyelectrolytes in free-solution electrophoresis. Having a simulation model at hand, which matches the experimental data and confirms theoretical predictions, opens new possibilities of investigating the dynamic behaviour of charged macromolecules. Due to the complex interactions between the system components, a purely theoretical description is often not possible or too general to provide insight into a specific problem. This highlights the great importance of computer simulations in the area of soft matter research and the contribution made by the presented work.

Appendix A.

Green-Kubo formula for the electrophoretic mobility

This appendix outlines the derivation of the Green-Kubo relation

$$\mu = \frac{1}{3k_{\text{B}}T} \sum_i q_i \int_0^{\infty} \langle \vec{v}_i(0) \cdot \vec{v}_c(\tau) \rangle d\tau \quad (5.4)$$

to calculate the electrophoretic mobility of a charged macromolecule at zero external electric field. In this equation the summation is executed over all charged particles (monomers, counterions and salt ions) in the system, and the \vec{v}_i are their individual velocities and the q_i their charges. Here, \vec{v}_{cm} is the velocity of the center of mass of the polyelectrolyte. The angular brackets $\langle \dots \rangle$ indicate an ensemble average which has to be taken over a large number of statistically independent samples.

This usage of the Green-Kubo relation has the great advantage of guaranteeing undistorted chain conformations and counterion distributions, as the measurement is done in the absence of any external field. As such, it can be an effective tool to determine dynamic quantities in computer simulations.

The derivation shown here is analogous to the derivation in Reference 76 and is a generalisation of the derivation for the electrophoretic mobility of colloidal objects shown in Reference 150.

The Hamiltonian of a charged system under the influence of an external electric field can be written as

$$H = H_0 + \sum_i q_i \vec{E} \cdot \vec{x}_i. \quad (\text{A.1})$$

Here, H_0 contains all interactions apart from the influence of the external field \vec{E} , which is taken into account by the scalar product between the electric field \vec{E} and the positions \vec{x}_i . The summation runs over all charged particles in the system, each of which is carrying a charge q_i .

Without loss of generality the following derivation is shown in 1d and for one particle only with $X(t)$ being the spatial coordinate. In general, the second part of the right hand side of Eq. A.1 can be seen as time dependent perturbation $f(t) = qE$ to the system with Hamiltonian H_0 :

$$H(t) = H_0 - f(t)X(t). \quad (\text{A.2})$$

Appendix A. Green-Kubo formula for the electrophoretic mobility

The mobility is defined as

$$\mu = \frac{\langle V_c(t) \rangle}{E}, \quad (\text{A.3})$$

where V_c is the velocity of the polyelectrolyte chain that is induced by the perturbation.

Onsager's regression states that "the correlation of microscopic thermal fluctuations at equilibrium describe the macroscopic decay of small non-equilibrium disturbances" [199, 200]. This can be translated to this system as follows: the center-of-mass velocity of the polyelectrolyte V_c (a macroscopic quantity) is related to the correlation function with the thermally fluctuating positions of the charges X (microscopic quantities). The proportionality constant is given by the perturbation causing the change in the macroscopic quantity, here by $f(t) = qE$. One obtains:

$$\langle V_c(t) \rangle = \beta f(t) \langle X(0) V_c(t) \rangle. \quad (\text{A.4})$$

Here, the averaging brackets denote an ensemble average.

Alternatively, one can apply linear response theory, which states that the most general response of a macroscopic property, here V_C , to a perturbation, $f(t)$, is given by:

$$\langle V_c(t) \rangle = \int_{-\infty}^{\infty} \chi_{VX}(t, t') f(t') dt'. \quad (\text{A.5})$$

The function $\chi_{VX}(t, t')$ describes the linear response of the system to the perturbation. It is often-called "after-effect" or memory function.

In order to describe a physical reponse, the after-effect function has to obey causality

$$\chi_{VX}(t, t') = 0 \quad \text{for} \quad t < t', \quad (\text{A.6})$$

and time-invariance, *i.e.*, the after-effect function can only depend on the time difference:

$$\chi_{VX}(t, t') = \chi_{VX}(t - t'). \quad (\text{A.7})$$

With this, Equation A.5 reads as follows:

$$\langle V_c(t) \rangle = \int_{-\infty}^t \chi_{VX}(t - t') f(t') dt'. \quad (\text{A.8})$$

If one now assumes $f(t') = 0$ for $t' > 0$ and $f(t') = f_0$ otherwise, *i.e.*, the perturbation is constant and switched off at time $t = 0$, this simplifies to:

$$\langle V_c(t) \rangle = f_0 \int_{-\infty}^0 \chi_{VX}(t - t') dt'. \quad (\text{A.9})$$

Now, let's define $\tau = t - t'$, and finally one obtains:

$$\langle V_c(t) \rangle = f_0 \int_0^{\infty} \chi_{VX}(\tau) d\tau \quad (\text{A.10})$$

By comparison of Equations A.4 and A.10 one finds an expression for the after-effect function

$$\chi_{VX}(\tau) = -\beta \langle X(0) \frac{d}{d\tau} V_c(\tau) \rangle \quad \text{for } \tau > 0, \quad (\text{A.11})$$

which can be substituted back into Equation A.10 to obtain the following Green-Kubo relation:

$$\langle V_c(t) \rangle = -\beta f_0 \int_0^{\infty} \langle X(0) \frac{d}{d\tau} V_c(\tau) \rangle d\tau \quad (\text{A.12})$$

Since time correlation functions are stationary, *i.e.*,

$$\frac{d}{dt} \langle X(t) V_c(t + t') \rangle = 0, \quad (\text{A.13})$$

the derivative can be shifted from V to X :

$$\langle X(t) \frac{d}{dt} V_c(t + t') \rangle = -\langle \frac{d}{dt} X(t) V_c(t + t') \rangle. \quad (\text{A.14})$$

Finally, f_0 is substituted back by the constant perturbation qE one ends up with

$$\langle V_c(t) \rangle = \beta E q \int_0^{\infty} \langle V(0) V_c(\tau) \rangle d\tau. \quad (\text{A.15})$$

After transforming this back to three dimensions and N charged particles in the system, the result is the Green-Kubo expression for the electrophoretic mobility:

$$\mu = \frac{1}{3k_B T} \sum_i^N q_i \int_0^{\infty} \langle \vec{v}_i(0) \cdot \vec{v}_c(\tau) \rangle d\tau. \quad (5.4)$$

Appendix B.

Sample ESPResSo scripts

The simulations presented in this thesis were done using the ESPResSo software package (see Ref. [128] and <http://www.espresso.mpg.de/> for details). ESPResSo is controlled by a scripting language that augments *tcl*¹.

The following detailed sample script was used to obtain the static and dynamic transport coefficients of polystyrene sulfonate. It has been tested and used on the standard version of Espresso including the most recent implementation of the Lattice Boltzmann algorithm by Ulf Schiller, *i.e.*, version 2.0.4t or higher².

The scripts use the following options that have to be activated: `FFTW3`, `ELECTROSTATICS`, `EXTERNAL_FORCES`, `LENNARD_JONES`, `BOND_ANGLE_HARMONIC`, `LB`.

The standard data generation procedure uses two scripts: a *simulation* script that sets the system up, performs the simulation and the data and saves all necessary data to the hard disk, and an *analysis* script that performs an offline analysis of the stored data. Even though, this method creates large amounts of data, it is nevertheless recommended as it ensures that all system information is available at all times and all data is present for inspection at any time following the quality guidelines of scientific work. Furthermore, disk space is fairly cheap nowadays and the long simulation time of up to 4 weeks warrant the usage of a couple of gigabytes.

All standard commands of *tcl* are highlighted in **blue**, whereas new ESPResSo commands are highlighted in **red**. Please refer to the ESPResSo documentation for detailed information on these commands.

B.1. Simulation script

The simulations script is divided in several independent sections that will be explained one by one. Only redundant lines of code and some comments are removed so that the combination of all code blocks yields the complete script.

B.1.1. Command line parsing

In order to simplify the specification of input parameters for various different simulations, a simple but flexible command line parser has been created.

¹<http://www.tcl.tk/>

²Please note that this version does not support proper treatment of boundary conditions for the LB fluid. A new implementation will be included in an upcoming release (December 2008).

Appendix B. Sample ESPResSo scripts

```
1 set parameters {nodes npc chains cm cs lbgamma lbtime run}  
2 set options {debug vmd {randomseed seed} {continue snapshot}  
   test}
```

The lists `parameters` contains all parameter that can be passed to the script as command line arguments. The parser automatically assigns the value to a variable of the specified name. As just the values are specified, the order of the parameters is crucial.

The list `options` provides the possibility to pass optional arguments to the script. An option is specified via `--identifier`, *e.g.*, `--debug`. The parser creates a variable of the given name that contains the value 0 if the options was not specified or 1 otherwise. Unlike parameters, the options can be specified in any order and can be either before or in between the parameters.³ Options in `{ }`-brackets have a second parameter that is read from the command line if this option is specified. The parameter has to directly follow the corresponding option.

This script takes the following input parameters:

nodes the number of nodes for parallel computing

npc the length of the polyelectrolyte chain

npc the number of independent polyelectrolyte chains

cm the monomer concentrations (in mMol/l), which together with the number and length of the chains defines the size of the simulation box.

cs the concentration of additional monovalent salt (in mMol/l)

lbgamma the value of the bare friction parameter of the LB algorithm

lbtime the interval of MD time steps at which the LB fluid is updated, *i.e.*, the LB time $\tau = \text{lbtime}\Delta t$.

run a unique identifier for this specific set of parameters

The available options are:

debug for additional console print outs

vmd opens an online connection to the program VMD (for visualisation)

randomseed set the initial state of the random number generator to `seed`⁴

³Note that the ESPResSO MPI wrapper expects the first value following the script name to be the number of processors, therefore it is advised to start with the parameter `nodes` and follow with options only thereafter.

⁴This allows for exactly reproducing the random numbers used in a simulation, which might be necessary for debugging.

continue accepts a file name that points to a snapshot of a previous simulation to be continued

test parameter that influence the choice of some simulation parameters, *e.g.*, results in short simulation times for testing purposes

Auxiliary functions

These two auxiliary functions are used by the automatic parser to display certain outputs in debug mode and to print out the information about the script usage if fewer parameters than expected are specified on the command line.

```

3 # debug display function (only works with debug flag)
4 proc debug { text } {
5     global debug
6     if { $debug } {
7         puts $text
8     }
9 }
10
11 # display usage information
12 proc usage_info { {msg} {excode -1} } {
13     global scriptname parameters options
14     puts $msg
15     puts "Usage: $scriptname"
16     puts "\tRequired parameters: $parameters"
17     puts "\tOptions: $options"
18     exit $excode
19 }

```

Automated parsing

The parameter are extracted from the arguments passed to the script via the command line that are stored in the list `argv`.

```

20 set scriptname [file tail $argv0]; # getting the script name
21 set num_params [llength $parameters]; # number of required
    parameter
22 set num_options [llength $options]; # number of different options
23
24 # default options to 0
25 for { set i 0 } { $i < $num_options } { incr i } {
26     for { set j 0 } { $j < [llength [lindex $options $i]] } { incr
        j } {
27         set [lindex [lindex $options $i] $j] 0
28     }
29 }
30
31 # parse command line

```

Appendix B. Sample ESPResSo scripts

```
32 set num_params_set 0; # number of arguments already set
33 set currarg 0; # current argument to be passed
34 while { $currarg < $argc } {
35     switch -glob -- [lindex $argv $currarg] {
36         --* {; # set options (starting with --) by name
37             set curropt [lindex $argv $currarg]
38             set curropt [string trimleft $curropt -]
39             set optpos [lsearch -glob $options "$curropt*"]
40             if { $optpos < 0 } { usage_info "Option not recognized:
41                 --$curropt." }
42             set curropt [lindex [lindex $options $optpos] 0]
43             set $curropt 1; incr currarg;
44             for { set i 1 } { $i < [llength [lindex $options $optpos]]
45                 } { incr i } { set [lindex [lindex $options $optpos] $i]
46                     [lindex $argv $currarg]; incr currarg }
47         }
48     default {; # set required parameters by order
49         if { $num_params_set < $num_params } { set [lindex
50             $parameters $num_params_set] [lindex $argv $currarg];
51             incr num_params_set; incr currarg }
52     }
53 }
54 if { $num_params_set < $num_params } { usage_info "Not enough
55     arguments ($num_params_set < $num_params)." }
56 unset currarg
57 unset num_params_set
```

Note that the usage of

```
set [lindex $parameters $num_params_set] [lindex $argv $currarg]
```

makes use of a special feature of the tcl language, namely that variable identifier can be variables themselves, *i.e.*, the first value of the list `parameter` becomes the variable `nodes` which is initialised with the corresponding command line value.

Feedback

Upon successful parsing of the command line arguments, the script displays all parameters and its values. For timing purposes, the start time is also recorded.

```
53 # start time
54 set starttime [clock seconds]
55 # check number of assigned processors
56 set rnodes [setmd n_nodes]
57
58 # feedback
59 puts "[code_info]"
60 puts ""
61 puts "$scriptname"
62 puts "Started at [clock format $starttime] on $rnodes cpu(s)."
```

```

63 puts "Parameters:"
64 for { set i 0 } { $i < $num_params } { incr i } { puts "\t[lindex
    $parameters $i] = [set [lindex $parameters $i]]" }
65 puts "Options given:"
66 for { set i 0 } { $i < $num_options } { incr i } {
67     if { [set [lindex [lindex $options $i] 0]] } {
68         puts "\t[lindex [lindex $options $i] 0]"
69         for { set j 1 } { $j < [llength [lindex $options $i]] } {
70             incr j } {
71                 puts "\t\t[lindex [lindex $options $i] $j] = [set [lindex
                    [lindex $options $i] $j]]"
72             }
73 }

```

Initialisation of random number generator

It is necessary to initialize the random number generator of ESPResSO with a unique number. Otherwise the drawing sequence of random numbers is always identical.

```

74 # check if randomseed and seed are available
75 if { [info exists randomseed] && [info exists seed] } {
76     # if randomseed is not given get a random one from cpu time
77     if { !($randomseed) } {
78         set seed [expr abs([clock clicks]%100000)]
79     }
80     # use list to distribute random seeds to more
81     # than one computing node
82     for { set i 0 } { $i < $rnodes } { incr i } {
83         lappend randomnums [expr $seed+$i*4543]
84     }
85     eval t_random seed $randomnums
86     unset randomnums
87 }
88 puts "\nInitial random number generator state = [t_random seed]"

```

B.1.2. System setup

The system is either generated according to the simulations parameters as specified in the script and via the command line or restored from a snapshot of a previous simulation run if specified via the `continue` option.

Continuation of a previous simulation

If a snapshot for continuation is specified, the system is restored to this snapshot. However, not the complete snapshot is restored, but only the MD variables (set by

Appendix B. Sample ESPResSo scripts

setmd), interactions, particles (including positions and velocities) and bonds. The variables on the tcl level are not restored by default.

```
89 if { $continue } {
90     puts "Restoring system ..."
91     if { [file exists $snapshot] } {
92
93         # only these blocks are restored
94         set restore "variable interactions particles bonds"
95         set blockfile_variable_blacklist {min_num_cells node_grid};
96         # this variables are not read from "variable" block
97
98         # get tags
99         puts "\tReading tags ..."
100        if { [string compare [lindex [split $snapshot "."] end]
101              "gz"]==0 } { set infile [open "|gzip -cd $snapshot" r] }
102        else { set infile [open "$snapshot" "r"] }
103        set eof 0; set tags {}
104        while { !$eof } {
105            if { [catch { lappend tags [blockfile $infile read start];
106                    blockfile $infile read toend } ] } { set eof 1 }
107        }
108        catch { close $infile }; unset eof
109        puts "\tdone."
110
111        # restore selected blocks
112        puts "\tReading system ..."
113        if { [string compare [lindex [split $snapshot "."] end]
114              "gz"]==0 } { set infile [open "|gzip -cd $snapshot" r] }
115        else { set infile [open "$snapshot" "r"] }
116        for { set i 0 } { $i < [llength $tags] } { incr i } {
117            if { [lsearch $restore [lindex $tags $i]] >= 0 } {
118                blockfile $infile read [lindex $tags $i]; puts
119                "\t\t[lindex $tags $i]"
120            } else {
121                blockfile $infile read start; blockfile $infile read
122                toend;
123            }
124        }
125        catch { close $infile }; unset tags; unset restore;
126        puts "\tdone."
127    } else { puts "Cannot open '$snapshot'"; exit }
128    puts "done."
129 }
```

Model parameter

Now, the model parameters are set. At this point the generic coarse-grained MD model is specified to match the system of interest, in this case polystyrene sulfonate (PSS) under the conditions used in the corresponding experiments.

```

123 set sigma [expr 2.5/0.91]; # beads are 0.91 apart and represent
    2.5 A (PSS)
124 set nm [expr $cm*1e-3*6.022*1e-4 * pow($sigma,3)];# number
    density in reduced units
125 set ns [expr $cs*1e-3*6.022*1e-4 * pow($sigma,3)];# number
    density in reduced units
126
127 set length [expr round(pow($npc*$chains/$nm,1./3.))]
128
129 set nsalt [expr round(pow($length,3)*$ns)]
130 set nci [expr $npc*$chains+$nsalt]
131 set nco [expr $nsalt]
132
133 # FENE parameters
134 set fene_k 30
135 set fene_r 1.5
136
137 # LJ parameters
138 set lj_eps 0.25
139 set lj_sig 1.0
140 set lj_cut 1.12246
141 set lj_shift 0.25
142 set lj_off 0.0
143
144 # lb fluid parameter
145 # set lbgamma 20.0 <- defined via command line
146 set lbdens 0.864
147 set agrid 1.0
148 set visc 3.0
149 set lb_timestep [expr $timestep*$lbtme]
150
151 # Bjerrum length
152 set bjerrum [expr 7.1/$sigma]
153
154 # Debye length
155 set l_d [expr
    1./sqrt(4*[PI]*$bjerrum*($nci+$nco)/pow($length,3))]
156 puts " l_d = $l_d sigma = [expr $l_d*$sigma] A"

```

Remember that the bare friction parameter of the LB fluid, `lbgamma`, is obtained as command line argument.

Generic simulation parameter

Additionally, the following generic parameters have to be specified.

```
157 # Integration parameter
158 set gamma 1.0; # langevin friction
159 set temp 1.0
160 set timestep 0.01
161 set skin 0.2
162
163 # Electrostatic interaction parameters
164 set accuracy 1.0e-5; # accuracy for electrostatic interaction
165
166 # Other parameters
167 set tcl_precision 6
168
169 # Integration cycles
170 if { $test } {
171   set warm_n_times 20
172   set warm_steps 100
173   set int_eq_steps 10000
174   set int_eqlb_steps 10000
175   set int_n_times 10000
176   set int_steps 10
177   set savesteps 100
178   set vacsteps 1000
179   set maxtau 100; # tau = 10.0
180   set interval 1; # dtau = 0.1
181 } else {
182   set warm_n_times 20
183   set warm_steps 100
184   set int_eq_steps 1000000
185   set int_eqlb_steps 1000000
186   set int_n_times 1000000
187   set int_steps 10
188   set savesteps 100
189   set vacsteps 100000
190   set maxtau 400; # tau = 40.0
191   set interval 1; # dtau = 0.1
192 }
```

System identification

Based on the chosen parameters a unique system identification is created and the necessary directories and files to store the simulation data are created.

```
193 set subdirname "pss-lb-t${lbtime}-g$gamma-gk"
194
195 # create subdirectory to store output data
196 if { ![ file isdirectory "$subdirname" ] } {
```



```

197 puts "Creating path '$subdirname'."
198 file mkdir $subdirname
199 }
200
201 # create subdirectory to store snapshots
202 if { ![ file isdirectory "$subdirname/snapshots" ] } {
203 puts "Creating path '$subdirname/snapshots'."
204 file mkdir $subdirname/snapshots
205 }
206
207 if { $test } {
208 set ident "test-pss-cm$cm-cs$cs-${chains}x${npc}-run${run}"
209 } else {
210 set ident "data-pss-cm$cm-cs$cs-${chains}x${npc}-run${run}"
211 }
212
213 puts "subdirname = $subdirname"
214 puts "ident = $ident"
215
216 if { !($test) } {
217 # check if simulation file already exists.
218 if { [ file exists "$subdirname/$ident.final.gz" ] } {
219 puts "WARNING: $subdirname/$ident.final.gz already exists."
220 puts "To continue, use the continue option and provide a
221     different run number"
222 exit
223 }

```

Simulation box setup

Now, it is time to specify the simulation box.

```

224 # define the cellsystem
225 cellsystem domain_decomposition -no_verlet_list
226
227 if { !($continue) } {
228 # set simulation box
229 setmd box_l $length $length $length
230 setmd periodic 1 1 1
231 setmd skin $skin
232 setmd time_step $timestep
233 }
234
235 puts "System size: [setmd box_l]."

```

Appendix B. Sample ESPResSo scripts

Interactions

Before setting up the particles, ESPResSO requires to specify the interactions. Please note that electrostatic and hydrodynamic interactions are only specified at a later point in the script.

```
236 if { !($continue) } {  
237   # non-bonded interaction  
238   # type 0 negative chain  
239   # type 1 counterions  
240   # type 2 salt ions +  
241   # type 3 salt ions -  
242   inter 0 0 lennard-jones $lj_eps $lj_sig $lj_cut $lj_shift  
     $lj_off  
243   inter 0 1 lennard-jones $lj_eps $lj_sig $lj_cut $lj_shift  
     $lj_off  
244   inter 0 2 lennard-jones $lj_eps $lj_sig $lj_cut $lj_shift  
     $lj_off  
245   inter 0 3 lennard-jones $lj_eps $lj_sig $lj_cut $lj_shift  
     $lj_off  
246   inter 1 1 lennard-jones $lj_eps $lj_sig $lj_cut $lj_shift  
     $lj_off  
247   inter 1 2 lennard-jones $lj_eps $lj_sig $lj_cut $lj_shift  
     $lj_off  
248   inter 1 3 lennard-jones $lj_eps $lj_sig $lj_cut $lj_shift  
     $lj_off  
249   inter 2 2 lennard-jones $lj_eps $lj_sig $lj_cut $lj_shift  
     $lj_off  
250   inter 2 3 lennard-jones $lj_eps $lj_sig $lj_cut $lj_shift  
     $lj_off  
251  
252   # bonded interaction  
253   inter 0 FENE $fene_k $fene_r  
254 } else {  
255   puts "System restore: [inter]"  
256 }
```

Particles

Last but not least the MD particles are added to the system.

```
257 if { !($continue) } {  
258   # polymer  
259   polymer $chains $npc 1.0 types 0 0 charge -1 distance 1 mode RW  
     1.0 30000  
260   counterions [expr $chains*$npc] charge 1 type 1 mode SAW 1.0  
     30000  
261  
262   if { $nsalt > 0 } {
```

```

263     # setup salt
264     salt $nsalt $nsalt mode SAW 1.0 2000 charges 1 -1 types 2 3
265 }
266 }
267 puts "[setmd n_part] particles."

```

Open connection to VMD

The system setup is completed and a connection to VMD is opened to visualize the system if the corresponding option is specified.

```

268 if { $vmd } {
269     puts "Set up VMD connection at [clock format [clock seconds]]"
270     prepare_vmd_connection "$ident" 10 1
271     imd listen 30
272     imd positions -unfolded
273     puts "Done."
274 }

```

B.1.3. System warmup

Initially the system is in an artificial configuration and has to be relaxed to an equilibrium configuration first. This process called the system warmup is again split in different parts.

```

275 thermostat off
276 thermostat langevin $stemp $gamma

```

For equilibration a pure Langevin thermostat is used without the inclusion of hydrodynamic interactions as it is orders of magnitude faster⁵.

Chain relaxation

The first, very short warmup cycle allows the polyelectrolyte chain and the counterions to relax from their initial positions. This way, they can escape energetically unfavourable initial position that were chosen at random.

```

277 if { !($continue) } {
278     puts "Start warmup 1 at [clock format [clock seconds]]"
279
280     # set LJ cap
281     set cap 5
282     inter ljforcecap $scap
283
284     # Warmup Integration Loop for chain setup
285     set i 0

```

⁵Furthermore, the static properties are not affected by the presence of hydrodynamic interactions.

Appendix B. Sample ESPResSo scripts

```
286 while { $i < $warm_n_times } {
287   if {[catch {integrate $warm_steps} err]} {
288     puts "caught error $err at time [setmd time]"
289     puts [part [lindex [lindex $err end] end] print pos]
290     exit
291   }
292   stop_particles
293   if { $test } {
294     puts "run $i at time=[setmd time] (LJ cap=$cap) at [clock
295       format [clock seconds]]"
296     flush stdout
297   }
298   if { $vmd } {
299     imd positions -unfolded
300   }
301   # Increase LJ cap
302   set cap [expr $cap+5]
303   inter ljforcecap $cap
304   incr i
305 }
306 # Bring back the original forces
307 inter ljforcecap 0
308 integrate $warm_steps
309 puts "\nDone."
310 }
```

Note that the Lennard-Jones interactions are capped to avoid nonphysically high forces that arise when two particles are arbitrary close as a consequence of the random placement. Likewise, the velocities of the particles is reduced to zero after each integration cycle to improve numerical stability.

Setting up electrostatics

As a next step, electrostatic interactions are added to the system by activating the P3M algorithm. Here, the automated tuning routine is used to specify the P3M parameter. The tuning of the parameter is followed by a second warmup phase now including electrostatic interactions between all particles.

```
311 puts "Set up electrostatics at [clock format [clock seconds]]"
312 if { $test } {
313   puts "Tune p3m ... "
314   puts "[inter coulomb 2.84 p3m 7.93306 16 5 0.317383
315     0.000996235]"
316   puts "Coulomb parameters: [inter coulomb]"
317 } else {
318   puts "[inter coulomb $bjerrum p3m tunev2 accuracy $accuracy
319     r_cut 0 cao 0 mesh 0]"
320   puts "Coulomb parameters: [inter coulomb]"
321 }
```

```

319 }
320 puts "Done."
321
322 # Equilibrate with electrostatics
323 if { !($continue) } {
324   puts "Start equilibration at [clock format [clock seconds]]"
325   integrate $int_eq_steps
326   if { $vmd } {
327     imd positions -unfolded
328   }
329   # save equilibrated configuration
330   checkpoint_set "$subdirname/$ident.equilibrated.gz"
331 }

```

Setting up hydrodynamics

The last warmup phase is done after activating the hydrodynamic interactions via coupling of the MD particles to the LB fluid.

```

332 # stop all particles before entering lb
333 stop_particles
334 thermostat off
335 thermostat lb $stemp
336 lbfluid dens $lbdens visc $visc agrid $agrid tau $lb_timestep
337 lbfluid friction $lbgamma
338 puts " [thermostat]"
339 puts " lbfluid dens $lbdens visc $visc agrid $agrid tau
340     $lb_timestep"
341 puts " lbfluid friction $lbgamma"
342
343 # Equilibrate with LB
344 puts "Start equilibration with lb at [clock format [clock
345     seconds]]"
346 integrate $int_eqlb_steps

```

B.1.4. Data generation

The system is integrated over 10^7 time steps and snapshots are saved at equal intervals for offline analysis.

```

345 puts "Start simulation at [clock format [clock seconds]]"
346
347 # reset time
348 setmd time 0
349
350 # integration loop
351 for {set i 1} { $i <= $int_n_times } { incr i } {
352   integrate $int_steps

```

Appendix B. Sample ESPResSo scripts

```
353 # save snapshot
354 if { $i%$savesteps==0 } {
355     if { $test } { puts "Integration $i / $int_n_times" }
356     if { $vmd } {
357         imd positions -unfolded
358     }
359     # save snapshot
360     set out [open "|gzip -c - >
        $subdirname/snapshots/$ident.[format %06u [expr
        round([setmd time])]].gz" "w"]
361     #blockfile $out write variable all
362     #blockfile $out write tclvariable all
363     #blockfile $out write interactions
364     #blockfile $out write particles "id pos type q v f" all
365     #blockfile $out write bonds all
366     blockfile $out write particles "id pos" all
367     close $out
368 }
369 # ... for loop continued here
```

Velocity auto-correlation functions

The measurement of the diffusion and the electrophoretic mobility via Green-Kubo relation requires the calculation of velocity auto-correlation functions for all particles. These correlation functions decay very fast, but have to be sampled with high accuracy to obtain useful measurements. Therefore, they can not be determined with the same intervals as for example the static chain properties but have to be sampled individually. The large number of independent samples needed to obtain reasonable statistics also prohibits the complete storage of the trajectories, and thus the auto-correlation functions are analysed during the data production run and not via a separate offline analysis script.

```
370 # ... continuation of for loop
371
372 # normalizaton factor
373 # velocity correlation funtions use difference of positions
    instead of velocities
374 # normalisation by dt*dt (where dt is distance between two
    saved positions)
375 set norm [expr 1./pow($int_steps*[setmd time_step],2)]
376
377 # store configuratons in memory
378 analyze push $vacsteps
379
380 # analyze vac functions
381 if { $i%$vacsteps==0 } {
382     # analyze transport properties
383     # caculate ion diffusion
```

```

384 set vac [analyze vac 1 1 $maxtau $interval]
385 set ion [lindex $vac 0]
386 set eion [lindex $vac 1]
387 # caculate chain diffusion
388 set vac [analyze vac 2 1 $maxtau $interval]
389 set diff [lindex $vac 0]
390 set ediff [lindex $vac 1]
391 # caculate chain mobility
392 set vac [analyze vac 3 1 $maxtau $interval]
393 set mob [lindex $vac 0]
394 set emob [lindex $vac 1]
395
396 # write out diffusion graphs
397 set currtime [expr round([setmd time])]
398 set alldiffdat [open
    "$subdirname/$ident.alldiff-$maxtau-$interval.[format %06u
    [expr round([setmd time])]].dat" "w"]
399 puts $alldiffdat "#tau ion e(ion) diff e(diff) mob e(mob)"
400 for { set j 0 } { $j <= $maxtau } { incr j } {; # errors are
    multiplied with sqrt(2*t_auto), where t_auto is the
    autocorrelation time
401 puts -nonewline $alldiffdat "[expr $j*$sint_steps*$timestep]
    [expr [lindex $ion $j]*$norm] [expr [lindex $eion
    $j]*$norm*sqrt(10)]"
402 puts -nonewline $alldiffdat " [expr [lindex $diff
    $j]*$norm] [expr [lindex $ediff $j]*$norm*sqrt(10)]"
403 puts -nonewline $alldiffdat " [expr -1.0*[lindex $mob
    $j]*$norm] [expr [lindex $emob $j]*$norm*sqrt(10)]\n"
404 }
405 flush $alldiffdat
406 close $alldiffdat
407 }
408
409 # end of for loop
410 }

```

The function **analyze** vac is a user-defined function to efficiently calculate the auto-correlation functions from trajectories stored via **analyze** push.

End of script

The script finishes with the storage of a final snapshot. Additionally, the run-time is calculated for timing purposes.

```

411 # save final configuration (but not config array)
412 analyze remove
413 checkpoint_set "$subdirname/$ident.final.gz"
414
415 set stoptime [clock seconds]
416 puts "\nFinished without errors at [clock format $stoptime]"

```

Appendix B. Sample ESPResSo scripts

```
417 set usedtime [expr $stoptime - $starttime]
418 puts "Total time used: [format "%02u:%02u:%02u" [expr
    $usedtime/(60*60)] [expr ($usedtime%(60*60))/60] [expr
    ($usedtime%60)]] ."
419 exit
```

B.2. Analysis script

Upon the completion the data generation via the simulation script, a second analysis script is executed that loads the previously saved trajectories and calculates observables of interest. Note that the auto-correlation functions for the diffusion and mobility measurements are already calculated during the simulation script for reasons of efficiency.

B.2.1. Command line parsing

The analysis script starts with the same flexible command line parser which is therefore not discussed in detail.

```
1 set parameters {nodes npc chains cm cs lbgamma lbtme run}
2 set options {debug vmd {randomseed seed} {continue snapshot} test
    {skip skiplength}}
```

The parameter are identical to the ones provided to the simulation script. Additionally the option skip is available that removes the first skiplength stored snapshots from the analysis process.

B.2.2. User-defined functions

The script uses some of reoccurring functions to load and analyze the data. These are defined at the beginning of the script.

Column average

This procedure calculates the average over a data file column using the an auto-correlation time calculation to obtain the error estimate as explained in Reference 127.

```
89 proc get_uwerr_av { { filename } { dcol } { skip 0 } } {
90     if { [file exists $filename] } {
91         set input [open $filename r]
92         gets $input line
93         set header [lindex $line $dcol]
94         if { $::debug } {
95             puts "$line -> $header"
96         }
97         set data ""
```



```

98   while {[gets $input line] >= 0} {
99       if { $skip > 0 } {
100          incr skip -1
101       } else {
102          set tmp [lindex $line $dcol]
103          if { $tmp!=""} {
104             lappend data $tmp
105          }
106       }
107   }
108   set nrep [llength $data]
109   if { $::debug } {
110      puts "Analyze '$filename' - column $dcol - nrep $nrep"
111   }
112   if { [catch {set uwout [uwerr $data $nrep 1]} err] } {
113      puts "UW-Error: $filename"
114      puts "$err"
115      set result " 0.0 0.0 0.0"
116   } else {
117      set result "[lindex $uwout 0] [lindex $uwout 1]"
118   }
119   close $input
120   return "$header $result"
121 } else {
122   puts "WARNING: File '$filename' not found."
123   return ""
124 }
125 }

```

Simpson integration

To calculate the diffusion coefficient and the electrophoretic mobility the auto-correlation functions have to be integrated. This is done via Simpson integration.

```

126 proc simpsonintegrate { { datafile } { tcol } { dcol } { header 1
127   } { upperbound -1 } } {
128   # open data file
129   if { ![file exists $datafile] } {
130      puts "Could not find input file: $datafile."
131      puts "Exiting ..."
132      exit -1
133   }
134   set input [open $datafile "r"]
135   #puts "Data file opened: $datafile."
136
137   # read and discard header
138   set i 0
139   while { $i < $header } {
140      gets $input line

```

Appendix B. Sample ESPReso scripts

```

140     incr i
141     # if { $::debug } { puts "Line discarded: $line." }
142 }
143
144 # read data sets
145 set currt 0
146 set t { }
147 set data { }
148 set err { }
149 while { ([gets $input line] >= 0) &&
150 ((($upperbound != -1) && ($currt < $upperbound)) ||
151 ($upperbound == -1)) } {
152     set currt [lindex [split $line] $tcol]
153     lappend t $currt
154     set currd [lindex [split $line] $dcol]
155     lappend data $currd
156     set curre [lindex [split $line] [expr $dcol+1]]
157     if { $curre > 0 } {
158         lappend err $curre
159     } else {
160         lappend err 0.0
161     }
162 }
163 set n [llength $data]
164 set dt [expr ([lindex $t end]-[lindex $t 0])/(1.*($n-1))]
165
166 if { $n%2 == 0 } {
167     lappend t [expr [lindex $t end]+$dt]
168     lappend data 0.0
169     lappend err 0.0
170 }
171 set n [llength $data]
172
173 # simpson integration
174 set m [expr ([llength $t] - 1.)/2.]
175 set dat $data
176 set sumEven 0
177 for { set k 1 } { $k <= [expr $m-1] } { incr k } {
178     set sumEven [expr $sumEven + [lindex $dat [expr 2*$k]]]
179 }
180 set sumOdd 0
181 for { set k 1 } { $k <= $m } { incr k } {
182     set sumOdd [expr $sumOdd + [lindex $dat [expr 2*$k-1]]]
183 }
184 set intavg [expr $dt/3.*([lindex $dat 0]+[lindex $dat
185     end]+2.*$sumEven+4.*$sumOdd)]
186 }

```

Load system

This function restores the complete system description from a snapshot file and sets all internal variables accordingly.

```

187 proc loadsystem { { filename } } {
188   if { [ file exists $filename ] } {
189
190     # only these blocks are restored
191     set restore "variable interactions particles bonds"
192     # this variables are not read from "variable" block
193     set blockfile_variable_blacklist {min_num_cells node_grid};
194
195     # get tags
196     puts "\tReading tags ..."
197     if { [ string compare [ lindex [ split $filename "." ] end ]
198           "gz" ] == 0 } { set infile [ open "|gzip -cd $filename" r ] }
199       else { set infile [ open "$filename" "r" ] }
200     set eof 0; set tags {}
201     while { !$eof } {
202       if { [ catch { lappend tags [ blockfile $infile read start ];
203             blockfile $infile read toend ] ] } { set eof 1 }
204     }
205     catch { close $infile }; unset eof
206     puts "\tdone."
207
208     # restore selected blocks
209     puts "\tReading system ..."
210     if { [ string compare [ lindex [ split $filename "." ] end ]
211           "gz" ] == 0 } { set infile [ open "|gzip -cd $filename" r ] }
212       else { set infile [ open "$filename" "r" ] }
213     for { set i 0 } { $i < [ llength $tags ] } { incr i } {
214       if { [ lsearch $restore [ lindex $tags $i ] ] >= 0 } {
215         blockfile $infile read [ lindex $tags $i ]; puts
216           "\t\t[ lindex $tags $i ]"
217       } else {
218         blockfile $infile read start; blockfile $infile read
219           toend;
220       }
221     }
222     catch { close $infile }; unset tags; unset restore;
223     puts "\tdone."
224   } else { puts "Cannot open '$filename'"; exit }
225   puts "done."
226 }

```

Load snapshot

In contrast to `loadsystem` this function only updates the particle positions and velocities with the data from the snapshot file. It does not recreate a system from scratch. The loaded positions are added to the internal configuration array of ESPResSO via `analyze append`.

```

221 proc loadsnapshot { { filename } } {
222   if { [ file exists $filename ] } {
223
224     set tags "particles"
225     # only these blocks are restored
226     set restore "particles"
227     set blockfile_variable_blacklist {min_num_cells node_grid};
228     # this variables are not read from "variable" block
229
230     # restore selected blocks
231     #puts "\tReading system ..."
232     if { [ string compare [ lindex [ split $filename "." ] end ]
233           "gz" ] == 0 } { set infile [ open "|gzip -cd $filename" r ] }
234     else { set infile [ open "$filename" r ] }
235     for { set i 0 } { $i < [ llength $tags ] } { incr i } {
236       if { [ lsearch $restore [ lindex $tags $i ] ] >= 0 } {
237         blockfile $infile read [ lindex $tags $i ]; #puts
238         "\t\t[lindex $tags $i]"
239       } else {
240         blockfile $infile read start; blockfile $infile read
241         toend;
242       }
243     }
244     catch { close $infile }; unset tags; unset restore;
245     #puts "\tdone."
246   } else { puts "Cannot open '$filename'"; exit }
247   #puts "done."
248 }
249 analyze append
250 }
```

B.2.3. Restore system

The system is restored from a snapshot file and the configurations are loaded for analysis.

```

247 puts "\nStart analysis at [ clock format [ clock seconds ] ]"
248
249 # system identification
250 set subdirname "pss-lb-t$lbtime-g$gamma-gk"
251 if { $test } {
```

```

252  set ident "test-pss-cm$cm-cs$cs-${chains}x${npc}-run${run}"
253  } else {
254  set ident "data-pss-cm$cm-cs$cs-${chains}x${npc}-run${run}"
255  }
256  puts "subdirname = $subdirname"
257  puts "ident = $ident"
258
259  # output results
260  set outdirname "results"
261  if { ![file isdirectory "$outdirname"] } {
262  puts "Creating path '$outdirname'."
263  file mkdir $outdirname
264  }
265  set outident "result-lb-t$lbtime-g$lbgamma-E$E"\
266  "-cm$cm-cs$cs-${chains}x$npc-run$run.dat"
267  set output [open "$outdirname/$outident" w]
268
269  # load system
270  puts "Load system ..."
271  loadsystem $subdirname/$ident.final.gz
272
273  # load snapshots
274  set start 10
275  set stop 100000
276  set step 10
277  puts "Load snapshots ..."
278  for { set i $start } { $i <= $stop } { incr i $step } {
279  loadsnapshot $subdirname/snapshots/$ident.[format %06u $i].gz
280  }
281  puts "done."
282  puts "[analyze stored] configurations loaded."

```

B.2.4. Data analysis

Chain conformations and ion distributions

The stored configurations are used to calculate the static observables of the system such as the chain conformations and the distributions of ions around the chains.

```

284  # set chain
285  analyze set chains 0 $chains $npc
286
287  set pedat [open "$subdirname/$ident.pestats.dat" "w"]
288  puts $pedat "#time pe_re pe_rg pe_rh"
289
290  set cidat [open "$subdirname/$ident.counterion.dat" "w"]
291  puts $cidat "#time ci2 ci3 co2 co3"
292
293  for { set i 0 } { $i < [analyze stored] } { incr $i } {

```

Appendix B. Sample ESPResSo scripts

```

294 # activate i-th configuration
295 activate_configuration $i
296
297 #chain props
298 puts -nonewline $pedat "$i "
299 puts -nonewline $pedat "[lindex [analyze re] 0] "
300 puts -nonewline $pedat "[lindex [analyze rg] 0] "
301 puts $pedat "[lindex [analyze rh] 0]"
302
303 # ion distribution
304 if {$nsalt>0} {
305     set codist [lindex [analyze distribution { 3 } { 0 } 1.0
306                     3.0 2 0 1] 1]
307     set cidist [lindex [analyze distribution { 1 2 } { 0 } 1.0
308                     3.0 2 0 1] 1]
309 } else {
310     set cidist [lindex [analyze distribution { 1 } { 0 } 1.0
311                     3.0 2 0 1] 1]
312     set codist { {0 0} {0 0} }
313 }
314 puts $cidat "$i [expr $nci/$chains*[lindex [lindex $cidist 0]
315             1]] [expr $nci/$chains*[lindex [lindex $cidist 1] 1]]
316             [expr $nco/$chains*[lindex [lindex $codist 0] 1]] [expr
317             $nco/$chains*[lindex [lindex $codist 1] 1]]"
318 }
319 close $pedat
320 close $cidat

```

Averaging of the data files is done as a second step using the previously defined procedure `get_uwerr_av`.

```

321 # chainstats
322 puts $output "[get_uwerr_av $subdirname/$ident.pestats.dat 1
323 $skiplength]"
324 puts $output "[get_uwerr_av $subdirname/$ident.pestats.dat 2
325 $skiplength]"
326 puts $output "[get_uwerr_av $subdirname/$ident.pestats.dat 3
327 $skiplength]"
328
329 # counterions
330 puts $output "[get_uwerr_av $subdirname/$ident.counterion.dat 1
331 $skiplength]"
332 puts $output "[get_uwerr_av $subdirname/$ident.counterion.dat 2
333 $skiplength]"
334 puts $output "[get_uwerr_av $subdirname/$ident.counterion.dat 3
335 $skiplength]"
336 puts $output "[get_uwerr_av $subdirname/$ident.counterion.dat 4
337 $skiplength]"

```

Dynamic transport coefficients

After the static properties the dynamic properties are analysed, starting with the chain diffusion coefficient. Here, a linear fit to the root-mean square displacement is used which is also obtained from the stored configurations.

```

325 # output
326 set diffdat [open "$dirname/$ident.chaindiff.dat" w]
327 set deltat 10
328
329 # chain diffusion
330 set g3 [analyze <g3>]
331 for {set i 0} { $i < [llength $g3] } { incr i } {
332   puts $diffdat "[expr $i*$deltat] [lindex $g3 $i]"
333 }
334 close $diffdat
335
336 # prepare lin reg
337 set min 100
338 set max 2000
339 set reg ""
340 for { set i $min } { $i < $max } { incr i } {
341   lappend reg "[expr $i*$deltat] [lindex $g3 $i]"
342 }
343 set res [LinRegression $reg]
344 puts $output "D_rmsd [expr [lindex $res 1]/6.] [expr [lindex $res
345   3]/6.]"

```

Now, the velocity auto-correlation functions that were calculated during the simulation run have to be analysed. The integral value is calculated using Simpson integration and the averages of the independent correlation functions yield the final values for the dynamic transport coefficients of the chains and the ions.

```

345 set maxtau 400; # tau = 40.0
346 set interval 1; # dtau = 0.1
347 set start 10000
348 set stop 100000
349 set step 10000
350 set temp 1.0
351
352 # ion diffusion
353 set val 0; set err 0; set n 0
354 for { set snap $start } { $snap <= $stop } { incr snap $step } {
355   set tmp [expr 1./3.*[simpsonintegrate
356     "$dirname/$ident.alldiff-$maxtau-$interval.[format %06u
357     $snap].dat" 0 1]]
358   set val [expr $val+$tmp]
359   set err [expr $err+$tmp*$tmp]
360   incr n
361 }

```

Appendix B. Sample ESPResSo scripts

```
360 puts $output "D_ion [expr $val/$n] [expr
    sqrt(($n*$err-$val*$val)/($n*($n-1)))]"
361
362 # cm diffusion
363 set val 0; set err 0; set n 0
364 for { set snap $start } { $snap <= $stop } { incr snap $step } {
365     set tmp [expr 1./3.*[simpsonintegrate
        "$dirname/$ident.alldiff-$maxtau-$interval.[format %06u
        $snap].dat" 0 3]]
366     set val [expr $val+$tmp]
367     set err [expr $err+$tmp*$tmp]
368     incr n
369 }
370 puts $output "D_cm [expr $val/$n] [expr
    sqrt(($n*$err-$val*$val)/($n*($n-1)))]"
371
372 # cm diffusion
373 set val 0; set err 0; set n 0
374 for { set snap $start } { $snap <= $stop } { incr snap $step } {
375     set tmp [expr 1./(3.*$temp)*[simpsonintegrate
        "$dirname/$ident.alldiff-$maxtau-$interval.[format %06u
        $snap].dat" 0 5]]
376     set val [expr $val+$tmp]
377     set err [expr $err+$tmp*$tmp]
378     incr n
379 }
380 puts $output "mu_cm [expr $val/$n] [expr
    sqrt(($n*$err-$val*$val)/($n*($n-1)))]"
```

End of script

The script finishes after all observables have been written to the output file.

```
381 flush $output; close $output
382
383 # End of program
384 set stoptime [clock seconds]
385 puts "\nFinished without errors at [clock format $stoptime]"
386 set usedtime [expr $stoptime - $starttime]
387 puts "Total time used: [format "%02u:%02u:%02u" [expr
    $usedtime/(60*60)] [expr ($usedtime%(60*60))/60] [expr
    ($usedtime%60)]] ."
388 exit
```


Acknowledgments

Although only my name appears on the cover of this dissertation, many people have supported me throughout its three-year production. I would like to express my gratitude to all those people who have made this dissertation possible.

First of all, I want to thank my family for the invaluable help and support they have provided my whole life.

I want to thank Graziela for always motivating and comforting me, as well as for rigorous proof reading and aid in graphic design.

I am grateful to Christian Holm for involving me in the interesting research area of soft matter systems and for his inspiring supervision and guidance.

For myriads of helpful physical discussions, criticism, and advice, I further want to thank the whole SimBio group, in particular Sofia Kantorovich, Marcello Sega and Mehmet Süzen.

Furthermore, I want to thank my collaborators, who greatly contributed to the success of this work: Hervé Cottet, Ulrich Scheler, and Ute Böhme. Special thanks to Gary Slater for inviting me to Canada and to all current and former members of his group for a warm welcome and an awesome time.

I thank all developers of the formidable ESPResSo package, and in particular Ulf Schiller for his work on the implementation of the Lattice Boltzmann algorithm.

I thank the FIAS community for providing a fruitful and memorable environment for my dissertation.

This work was supported by the FIAS, the OSS, and the DAAD under a PPP grant, and the Volkswagen foundation.

Bibliography

- [1] J. D. McPherson, M. Marra, L. Hillier, R. H. Waterston, A. Chinwalla, J. Wallis, M. Sekhon, K. Wylie, E. R. Mardis, R. K. Wilson, R. Fulton, T. A. Kucaba, C. Wagner-McPherson, W. B. Barbazuk, S. G. Gregory, S. J. Humphray, L. French, R. S. Evans, G. Bethel, A. Whittaker, J. L. Holden, O. T. McCann, A. Dunham, C. Soderlund, C. E. Scott, D. R. Bentley, G. Schuler, H. C. Chen, W. H. Jang, E. D. Green, J. R. Idol, V. V. B. Maduro, K. T. Montgomery, E. Lee, A. Miller, S. Emerling, R. Kucherlapati, R. Gibbs, S. Scherer, J. H. Gorrell, E. Sodergren, K. Clerc-Blankenburg, P. Tabor, S. Naylor, D. Garcia, P. J. de Jong, J. J. Catanese, N. Nowak, K. Osoegawa, S. Z. Qin, L. Rowen, A. Madan, M. Dors, L. Hood, B. Trask, C. Friedman, H. Massa, V. G. Cheung, I. R. Kirsch, T. Reid, R. Yonescu, J. Weissenbach, T. Bruls, R. Heilig, E. Branscomb, A. Olsen, N. Doggett, J. F. Cheng, T. Hawkins, R. M. Myers, J. Shang, L. Ramirez, J. Schmutz, O. Velasquez, K. Dixon, N. E. Stone, D. R. Cox, D. Haussler, W. J. Kent, T. Furey, S. Rogic, S. Kennedy, S. Jones, A. Rosenthal, G. P. Wen, M. Schilhabel, G. Gloeckner, G. Nyakatura, R. Siebert, B. Schlegelberger, J. Korenburg, X. N. Chen, A. Fujiyama, M. Hattori, A. Toyoda, T. Yada, H. S. Park, Y. Sakaki, N. Shimizu, S. Asakawa, K. Kawasaki, T. Sasaki, A. Shintani, A. Shimizu, K. Shibuya, J. Kudoh, S. Minoshima, J. Ramser, P. Seranski, C. Hoff, A. Poustka, R. Reinhardt, and H. Lehrach. A physical map of the human genome. *Nature*, 409(6822):934–941, 2001.
- [2] C. Heller, G. W. Slater, P. Mayer, N. Dovichi, D. Pinto, J. L. Viovy, and G. Drouin. Free-solution electrophoresis of dna. *Journal of Chromatography a*, 806(1):113–121, 1998.
- [3] H. J. Ren, A. E. Karger, F. Oaks, S. Menchen, G. W. Slater, and G. Drouin. Separating dna sequencing fragments without a sieving matrix. *Electrophoresis*, 20(12):2501–2509, 1999.
- [4] J. Han and H. G. Craighead. Separation of long dna molecules in a micro-fabricated entropic trap array. *Science*, 288(5468):1026–1029, 2000.
- [5] A. E. Barron, D. S. Soane, and H. W. Blanch. Capillary electrophoresis of dna in uncross-linked polymer-solutions. *Journal of Chromatography A*, 652(1):3–16, 1993.
- [6] A. E. Barron, H. W. Blanch, and D. S. Soane. A transient entanglement coupling mechanism for dna separation by capillary electrophoresis in ultradilute polymer-solutions. *Electrophoresis*, 5(5):597–615, 1994.

Bibliography

- [7] L. Ulanovsky, G. Drouin, and W. Gilbert. Dna trapping electrophoresis. *Nature*, 343(6254):190–192, 1990.
- [8] C. Desruisseaux, G. W. Slater, and G. Drouin. The gel edge electric field gradients in denaturing polyacrylamide gel electrophoresis. *Electrophoresis*, 19:627–634, 1998.
- [9] L. Liu, P. S. Li, and S. A. Asher. Entropic trapping of macromolecules by mesoscopic periodic voids in a polymer hydrogel. *Nature*, 397:141–144, 1999.
- [10] L. A. Clark, G. T. Ye, and R. Q. Snurr. Molecular traffic control in a nanoscale system. *Physical Review Letters*, 84:2893–2896, 2000.
- [11] N. Pernodet, V. Samuilov, K. Shin, J. Sokolov, M. H. Rafailovich, D. Gersappe, and B. Chu. Dna electrophoresis on a flat surface. *Physical Review Letters*, 85(26):5651–5654, 2000.
- [12] Y. S. Seo, V. A. Samuilov, J. Sokolov, M. H. Rafailovich, B. Tinland, J. Kim, and B. Chu. Dna separation at a liquid-solid interface. *Electrophoresis*, 23(16):2618–2625, 2002.
- [13] P. S. Doyle, J. Bibette, A. Bancaud, and J. L. Viovy. Self-assembled magnetic matrices for dna separation chips. *Science*, 295(5563):2237–2237, 2002.
- [14] M. J. Chacron and G. W. Slater. Particle trapping and self-focusing in temporally asymmetric ratchets with strong field gradients. *Physical Review E*, 56(3):3446–3450, 1997.
- [15] L. L. Frumin, S. E. Peltek, and G. V. Zilberstein. Nonlinear focusing of dna macromolecules. *Phys. Rev. E*, 6402(2):021902, 2001.
- [16] C. Heller. Influence of electric field strength and capillary dimensions on the separation of dna. *Electrophoresis*, 21(3):593–602, 2000.
- [17] C. Heller. Principles of dna separation with capillary electrophoresis. *Electrophoresis*, 22(4):629–643, 2001.
- [18] C. Desruisseaux, D. Long, G. Drouin, and G. W. Slater. Electrophoresis of composite molecular objects. 1. relation between friction, charge, and ionic strength in free solution. *Macromolecules*, 34(1):44–52, 2001.
- [19] J. M. Deutsch. Dynamics of pulsed-field electrophoresis. *Phys. Rev. Lett.*, 59(11):1255–1258, 1987.
- [20] J. M. Deutsch. Theoretical-studies of dna during gel-electrophoresis. *Science*, 240(4854):922–924, 1988.
- [21] J. M. Deutsch and T. L. Madden. Theoretical-studies of dna during gel-electrophoresis. *J. Chem. Phys.*, 90(4):2476–2485, 1989.
- [22] M. Matsumoto and M. Doi. Brownian dynamics simulation of dna gel-electrophoresis. *Molecular Simulation*, 12(3-6):219–226, 1994.

- [23] H. Noguchi and M. Takasu. Dynamics of dna in entangled polymer solutions: An anisotropic friction model. *Journal of Chemical Physics*, 114(16):7260–7266, 2001.
- [24] T. T. Duong, G. Kim, R. Ros, M. Streek, F. Schmid, J. Brugger, D. Anselmetti, and A. Ros. Size-dependent free solution dna electrophoresis in structured microfluidic systems. *Microelectron. Eng.*, 67-8:905–912, 2003.
- [25] M. Streek, F. Schmid, T. T. Duong, and A. Ros. Mechanisms of dna separation in entropic trap arrays: a brownian dynamics simulation. *Journal of Biotechnology*, 112(1-2):79–89, 2004.
- [26] D. Long, J. L. Viovy, and A. Ajdari. Simultaneous action of electric fields and nonelectric forces on a polyelectrolyte: Motion and deformation. *Physical Review Letters*, 76(20):3858–3861, 1996.
- [27] M. Doi and S. F. Edwards. *The theory of polymer dynamics*. Oxford Science Publications, 1986.
- [28] A. E. Nkodo, J. M. Garnier, B. Tinland, H. J. Ren, C. Desruisseaux, L. C. McCormick, G. Drouin, and G. W. Slater. Diffusion coefficient of dna molecules during free solution electrophoresis. *Electrophoresis*, 22(12):2424–2432, 2001.
- [29] G. Nägele and P. Baur. Influence of hydrodynamic interactions on long-time diffusion in charge-stabilized colloids. *Europhysics Letters*, 38(7):557–562, 1997.
- [30] G. Nägele and P. Baur. Long-time dynamics of charged colloidal suspensions: hydrodynamic interaction effects. *Physica A*, 245(3-4):297–336, 1997.
- [31] P. Ahlrichs, R. Everaers, and B. Dünweg. Screening of hydrodynamic interactions in semidilute polymer solutions: A computer simulation study. *Physical Review E*, 64(4), 2001. doi: ARTN040501.
- [32] E. Stellwagen and N. C. Stellwagen. Determining the electrophoretic mobility and translational diffusion coefficients of dna molecules in free solution. *Electrophoresis*, 23(16):2794–2803, 2002.
- [33] E. Stellwagen, Y. J. Lu, and N. C. Stellwagen. Unified description of electrophoresis and diffusion for dna and other polyions. *Biochemistry*, 42(40):11745–11750, 2003. doi: DOI10.1021/bi035203p.
- [34] N. Grønbech-Jensen, R. J. Mashl, R. F. Bruinsma, and W. M. Gelbart. Counterion-induced attraction between rigid polyelectrolytes. *Phys. Rev. Lett.*, 78:2477–2480, 1997.
- [35] A. Y. Grosberg, T. T. Nguyen, and B. I. Shklovskii. Colloquium: The physics of charge inversion in chemical and biological systems. *Rev. Mod. Phys.*, 74:329, 2002.
- [36] J.-L. Barrat and J.-F. Joanny. Theory of polyelectrolyte solutions. *Advances in Chemical Physics*, 94:1–66, 1996.

Bibliography

- [37] M. Muthukumar. Theory of electrophoretic mobility of a polyelectrolyte in semidilute solutions of neutral polymers. *Electrophoresis*, 17(6):1167–1172, 1996.
- [38] A. R. Volkelt and J. Noolandi. On the mobility of stiff polyelectrolytes. *Journal of Chemical Physics*, 102(13):5506–5511, 1995.
- [39] U. Mohanty and N. C. Stellwagen. Free solution mobility of oligomeric dna. *Biopolymers*, 49(3):209–214, 1999.
- [40] K. Grass, U. Böhme, U. Scheler, H. Cottet, and C. Holm. Importance of hydrodynamic shielding for the dynamic behavior of short polyelectrolyte chains. *Physical Review Letters*, 100(9):096104, 2008.
- [41] K. Grass and C. Holm. On the importance of hydrodynamic interactions in polyelectrolyte electrophoresis. *J. Phys.: Condens. Matter*, 20(494217), 2008.
- [42] K. Grass and C. Holm. Polyelectrolytes in electric fields: Measuring the dynamical effective charge and effective friction. *Soft Matter*, *accepted*, 2009. <http://arxiv.org/abs/0902.1886>.
- [43] K. Grass, C. Holm, and G. W. Slater. Optimizing end-labeled free-solution electrophoresis by increasing the hydrodynamic friction of the drag labels. *Submitted to Macromolecules*, 2009. <http://arxiv.org/abs/0902.1889>.
- [44] G. W. Slater, C. Holm, M. V. Chubynsky, H. W. de Haan, A. Dubé, K. Grass, O. A. Hickey, C. Kingsburry, D. Sean, T. N. Shendruk, and L. Zhan. Modeling separation processes: A review of current computer simulation methods. *Electrophoresis*, (30):792–818, 2009.
- [45] H. Lamb. *Hydrodynamics*. Cambridge University Press, 6 edition, 1932.
- [46] L. D. Landau and E. M. Lifshitz. *Fluid Mechanics*, volume 6. Butterworth-Heinemann, 1987.
- [47] M. Rubinstein and R. H. Colby. *Polymer Physics*. Oxford University Press, Oxford, UK, 2003.
- [48] I. Teraoka. *Polymer solutions*. Wiley-Interscience, 2002.
- [49] P. J. Flory. *Principles of Polymer Chemistry*. Cornell University Press, Ithaca, NY, 1953.
- [50] J. L. Lebowitz, J. Descloiz, A. Isihara, J. L. Jackson, and M. E. Fisher. Discussion of statistics of long chains with repulsive interactions, 1969. *Journal of the Physical Society of Japan*.
- [51] D. S. McKenzie. Polymers and scaling. *Physics Reports. Physics Letters Section C*, 27c(2):35–88, 1976.
- [52] J. C. Leguillou and J. Zinnjustin. Critical exponents for n-vector model in 3 dimensions from field-theory. *Physical Review Letters*, 39(2):95–98, 1977.

- [53] M. A. Moore and A. J. Bray. Flory formula for polymer size exponent-nu. *Journal of Physics A-Mathematical and General*, 11(7):1353–1359, 1978.
- [54] P. E. Rouse. A theory of the linear viscoelastic properties of dilute solutions of coiling polymers. *Journal of Chemical Physics*, 21(7):1272–1280, 1953.
- [55] B. H. Zimm. Dynamics of polymer molecules in dilute solution - viscoelasticity, flow birefringence and dielectric loss. *Journal of Chemical Physics*, 24(2): 269–278, 1956.
- [56] B. Dünweg. Molecular dynamics algorithms and hydrodynamic screening. *J. Chem. Phys.*, 99(9):6977–82, 1993.
- [57] J. G. Kirkwood and J. Riseman. The intrinsic viscosities and diffusion constants of flexible macromolecules in solution. *Journal of Chemical Physics*, 16(6):565–573, 1948.
- [58] P. G. de Gennes. *Scaling Concepts in Polymer Physics*. Cornell University Press, Ithaca, NY, 1979.
- [59] G. S. Manning. Limiting laws and counterion condensation in polyelectrolyte solutions .1. colligative properties. *Journal of Chemical Physics*, 51(3):924–&, 1969.
- [60] F. Oosawa. *Polyelectrolytes*. Marcel Dekker, New York, 1971.
- [61] G. S. Manning and J. Ray. Counterion condensation revisited. *Journal of Biomolecular Structure & Dynamics*, 16(2):461–476, 1998.
- [62] D. Stigter. Evaluation of the counterion condensation theory of polyelectrolytes. *Biophysical Journal*, 69(2):380–388, 1995.
- [63] L. Belloni, M. Drifford, and P. Turq. Counterion diffusion in polyelectrolyte solutions. *Chem. Phys.*, 83:147, 1984.
- [64] L. Belloni. Ionic condensation and charge renormalization in colloidal suspensions. *Colloids and Surfaces*, A 140:227, 1998.
- [65] M. Deserno, C. Holm, and S. May. Fraction of condensed counterions around a charged rod: Comparison of poisson-boltzmann theory and computer simulations. *Macromolecules*, 33(1):199–206, 2000.
- [66] T. Odijk. Polyelectrolytes near the rod limit. *J. Polym. Sci., Polym. Phys. Ed.*, 15:477, 1977.
- [67] J. Skolnick and M. Fixman. Electrostatic persistence length of a wormlike polyelectrolyte. *Macromolecules*, 10:944, 1977.
- [68] G. W. Slater, T. B. L. Kist, H. J. Ren, and G. Drouin. Recent developments in DNA electrophoretic separations. *Electrophoresis*, 19(10):1525–1541, 1998.
- [69] J. L. Viovy. Electrophoresis of dna and other polyelectrolytes: Physical mechanisms. *Reviews of Modern Physics*, 72(3):813–872, 2000.

Bibliography

- [70] G. W. Slater, C. Desrulsseaux, S. J. Hubert, J. F. Mercier, J. Labrie, J. Boileau, F. Tessier, and M. P. Pepin. Theory of DNA electrophoresis: A look at some current challenges. *Electrophoresis*, 21(18):3873–3887, 2000.
- [71] G. W. Slater, S. Guillouzie, M. G. Gauthier, J. F. Mercier, M. Kenward, L. C. McCormick, and F. Tessier. Theory of dna electrophoresis (similar to 1999-2002(1)/(2)). *Electrophoresis*, 23(22-23):3791–3816, 2002.
- [72] P. G. Righetti, editor. *Capillary Electrophoresis in Analytical Biotechnology*. CRC Press, Boca Raton, 1996.
- [73] D. A. Hoagland, E. Arvanitidou, and C. Welch. Capillary electrophoresis measurements of the free solution mobility for several model polyelectrolyte systems. *Macromolecules*, 32(19):6180–6190, 1999.
- [74] H. Cottet, P. Gareil, O. Theodoly, and C. E. Williams. A semi-empirical approach to the modeling of the electrophoretic mobility in free solution: Application to polystyrenesulfonates of various sulfonation rates. *Electrophoresis*, 21(17):3529–3540, 2000.
- [75] M. P. Allen and D. J. Tildesley. *Computer Simulation of Liquids*. Oxford Science Publications. Clarendon Press, Oxford, 1 edition, 1987.
- [76] D. Frenkel and B. Smit. *Understanding Molecular Simulation*. Academic Press, San Diego, second edition, 2002.
- [77] J. D. Weeks, D. Chandler, and H. C. Andersen. Role of repulsive forces in determining the equilibrium structure of simple liquids. *J. Chem. Phys.*, 54: 5237, 1971.
- [78] T. Soddemann, B. Dünweg, and K. Kremer. A generic computer model for amphiphilic systems. *Eur. Phys. J. E*, 6:409, 2001.
- [79] W. C. Swope, H. C. Andersen, P. H. Berens, and K. R. Wilson. A computer-simulation method for the calculation of equilibrium-constants for the formation of physical clusters of molecules - application to small water clusters. *Journal of Chemical Physics*, 76(1):637–649, 1982.
- [80] A. Arnold and C. Holm. Efficient methods to compute long-range interactions for soft matter systems. *Advanced Computer Simulation Approaches For Soft Matter Sciences Ii*, 185:59–109, 2005. doi: DOI10.1007/b136793.
- [81] S. W. Deleeuw, J. W. Perram, and E. R. Smith. Simulation of electrostatic systems in peridodic boundary-conditions. 1. lattice sums and dielectric-constants. *Proceedings of the Royal Society of London Series A-Mathematical Physical and Engineering Sciences*, 373(1752):27–56, 1980.
- [82] P. P. Ewald. The calculation of optical and electrostatic grid potential. *Annalen Der Physik*, 64(3):253–287, 1921.
- [83] J. W. Eastwood, R. W. Hockney, and D. N. Lawrence. P3m3dp - the 3-dimensional periodic particle-particle-particle-mesh program. *Computer*

- Physics Communications*, 19(2):215–261, 1980.
- [84] R. W. Hockney and J. W. Eastwood. *Computer Simulation Using Particles*. IOP, London, 1988.
- [85] T. Darden, D. York, and L. G. Pedersen. Particle mesh ewald - an $n \cdot \log(n)$ method for ewald sums in large systems. *Journal of Chemical Physics*, 98(12):10089–10092, 1993.
- [86] U. Essmann, L. Perera, M. L. Berkowitz, T. Darden, H. Lee, and L. G. Pedersen. A smooth particle mesh ewald method. *Journal of Chemical Physics*, 103(19):8577–8593, 1995.
- [87] M. Deserno and C. Holm. How to mesh up ewald sums. i. a theoretical and numerical comparison of various particle mesh routines. *Journal of Chemical Physics*, 109(18):7678–7693, 1998.
- [88] L. Greengard and V. Rokhlin. A fast algorithm for particle simulations. *Journal of Computational Physics*, 73(2):325–348, 1987.
- [89] F. S. Lee and A. Warshel. A local reaction field method for fast evaluation of long-range electrostatic interactions in molecular simulations. *Journal of Chemical Physics*, 97(5):3100–3107, 1992.
- [90] M. Deserno and C. Holm. How to mesh up ewald sums. ii. an accurate error estimate for the particle-particle-particle-mesh algorithm. *Journal of Chemical Physics*, 109(18):7694–7701, 1998.
- [91] G. S. Grest and K. Kremer. Molecular-dynamics simulations for polymers in the presence of a heat bath. *Physical Review A*, 33(5):3628–3631, 1986.
- [92] H. B. Callen and T. A. Welton. Irreversibility and generalized noise. *Physical Review*, 83(1):34–40, 1951.
- [93] M. Deserno. *Counterion condensation for rigid linear polyelectrolytes*. PhD thesis, University of Mainz, 2000.
- [94] A. Malevanets and R. Kapral. Mesoscopic model for solvent dynamics. *Journal of Chemical Physics*, 110(17):8605–8613, 1999.
- [95] A. Malevanets and J. M. Yeomans. Dynamics of short polymer chains in solution. *Europhysics Letters*, 52(2):231–237, 2000.
- [96] A. Malevanets and R. Kapral. Solute molecular dynamics in a mesoscale solvent. *Journal of Chemical Physics*, 112(16):7260–7269, 2000.
- [97] T. Ihle and D. M. Kroll. Stochastic rotation dynamics. i. formalism, galilean invariance, and green-kubo relations. *Physical Review E*, 67(6), 2003. doi: ARTN066705.
- [98] T. Ihle and D. M. Kroll. Stochastic rotation dynamics. ii. transport coefficients, numerics, and long-time tails. *Physical Review E*, 67(6), 2003. doi: ARTN066706.

Bibliography

- [99] M. Ripoll, K. Mussawisade, R. G. Winkler, and G. Gompper. Low-reynolds-number hydrodynamics of complex fluids by multi-particle-collision dynamics. *Europhysics Letters*, 68(1):106–112, 2004. doi: DOI10.1209/epl/i2003-10310-1.
- [100] M. Ripoll, K. Mussawisade, R. G. Winkler, and G. Gompper. Dynamic regimes of fluids simulated by multiparticle-collision dynamics. *Physical Review E*, 72(1), 2005. doi: ARTN016701.
- [101] P. Espanol. Hydrodynamics from dissipative particle dynamics. *Physical Review E*, 52(2):1734–1742, 1995.
- [102] P. Espanol and P. Warren. Statistical-mechanics of dissipative particle dynamics. *Europhysics Letters*, 30(4):191–196, 1995.
- [103] P. Espanol. Dissipative particle dynamics with energy conservation. *Europhysics Letters*, 40(6):631–636, 1997.
- [104] R. D. Groot and P. B. Warren. Dissipative particle dynamics: Bridging the gap between atomistic and mesoscopic simulation. *Journal of Chemical Physics*, 107(11):4423–4435, 1997.
- [105] P. J. Hoogerbrugge and J. M. V. A. Koelman. Simulating microscopic hydrodynamic phenomena with dissipative particle dynamics. *Europhysics Letters*, 19(3):155–160, 1992.
- [106] G. R. McNamara and G. Zanetti. Use of the boltzmann-equation to simulate lattice-gas automata. *Physical Review Letters*, 61(20):2332–2335, 1988.
- [107] R. Benzi, S. Succi, and M. Vergassola. The lattice boltzmann-equation - theory and applications. *Physics Reports-Review Section of Physics Letters*, 222(3):145–197, 1992.
- [108] A. J. C. Ladd. Numerical simulations of particulate suspensions via a discretized boltzmann-equation .1. theoretical foundation. *Journal of Fluid Mechanics*, 271:285–309, 1994.
- [109] A. J. C. Ladd. Numerical simulations of particulate suspensions via a discretized boltzmann-equation .2. numerical results. *Journal of Fluid Mechanics*, 271:311–339, 1994.
- [110] S. Chen and G. D. Doolen. Lattice boltzmann method for fluid flows. *Annual Review of Fluid Mechanics*, 30:329–364, 1998.
- [111] J. M. Yeomans. Mesoscale simulations: Lattice boltzmann and particle algorithms. *Physica A-Statistical Mechanics and Its Applications*, 369(1):159–184, 2006. doi: DOI10.1016/j.physa.2006.04.011.
- [112] G. Gompper, T. Ihle, D. M. Kroll, and R. G. Winkler. *Advanced Computer Simulation Approaches for Soft Matter Sciences III*, chapter I, pages 1–88. Springer, 2009.

- [113] B. Dünweg and A. J. C. Ladd. *Advanced Computer Simulation Approaches for Soft Matter Sciences III*, chapter II, pages 89–166. Springer, 2009.
- [114] C. Junghans, M. Praprotnik, and K. Kremer. Transport properties controlled by a thermostat: An extended dissipative particle dynamics thermostat. *Soft Matter*, 4(1):156–161, 2008. doi: DOI10.1039/b713568h.
- [115] H. Noguchi and G. Gompper. Transport coefficients of off-lattice mesoscale-hydrodynamics simulation techniques. *Physical Review E*, 78(1), 2008. doi: ARTN016706.
- [116] C. M. Pooley and J. M. Yeomans. Kinetic theory derivation of the transport coefficients of stochastic rotation dynamics. *Journal of Physical Chemistry B*, 109(14):6505–6513, 2005. doi: DOI10.1021/jp046040x.
- [117] Y. Inoue, Y. L. Chen, and H. Ohashi. Development of a simulation model for solid objects suspended in a fluctuating fluid. *Journal of Statistical Physics*, 107(1-2):85–100, 2002.
- [118] M. Revenga, I. Zuniga, P. Espanol, and I. Pagonabarraga. Boundary models in dpd. *International Journal of Modern Physics C*, 9(8):1319–1328, 1998.
- [119] J. Smiatek, M. P. Allen, and F. Schmid. Tunable-slip boundaries for coarse-grained simulations of fluid flow. *European Physical Journal E*, 26(1-2):115–122, 2008. doi: DOI10.1140/epje/i2007-10311-4.
- [120] S. Y. Chen, D. Martinez, and R. W. Mei. On boundary conditions in lattice boltzmann methods. *Physics of Fluids*, 8(9):2527–2536, 1996.
- [121] A. J. C. Ladd and R. Verberg. Lattice-boltzmann simulations of particle-fluid suspensions. *Journal of Statistical Physics*, 104(5-6):1191–1251, 2001.
- [122] P. Ahlrichs and B. Dünweg. Simulation of a single polymer chain in solution by combining lattice boltzmann and molecular dynamics. *Journal of Chemical Physics*, 111(17):8225–8239, 1999.
- [123] J. Horbach and S. Succi. Lattice boltzmann versus molecular dynamics simulation of nanoscale hydrodynamic flows. *Physical Review Letters*, 96(22), 2006. doi: ARTN224503.
- [124] P. L. Bhatnagar, E. P. Gross, and M. Krook. A model for collision processes in gases .1. small amplitude processes in charged and neutral one-component systems. *Physical Review*, 94(3):511–525, 1954.
- [125] R. Adhikari, K. Stratford, M. E. Cates, and A. J. Wagner. Fluctuating lattice boltzmann. *Europhysics Letters*, 71(3):473–479, 2005. doi: DOI10.1209/epl/i2004-10542-5.
- [126] B. Dünweg, U. D. Schiller, and A. J. C. Ladd. Statistical mechanics of the fluctuating lattice boltzmann equation. *Physical Review E*, 76(3), 2007. doi: ARTN036704.

Bibliography

- [127] U. Wolff. Monte carlo errors with less errors. *Comput. Phys. Commun.*, 156: 143–153, 2004.
- [128] H. J. Limbach, A. Arnold, B. A. Mann, and C. Holm. ESPResSo – an extensible simulation package for research on soft matter systems. *Comp. Phys. Comm.*, 174(9):704–727, 2006.
- [129] W. Humphrey, A. Dalke, and K. Schulten. VMD – Visual Molecular Dynamics. *Journal of Molecular Graphics*, 14:33–38, 1996.
- [130] R. R. Netz. Polyelectrolytes in electric fields. *Journal of Physical Chemistry B*, 107(32):8208–8217, 2003. doi: DOI10.1021/jp022618w.
- [131] R. R. Netz. Nonequilibrium unfolding of polyelectrolyte condensates in electric fields. *Physical Review Letters*, 90(12):128104, 2003. doi: ARTN128104.
- [132] X. Schlagberger and R. R. Netz. Orientation of elastic rods in homogeneous stokes flow. *Europhysics Letters*, 70:129–135, 2005.
- [133] S. Frank and R. G. Winkler. Polyelectrolyte electrophoresis: field effects and hydrodynamic interactions. *Europhys. Lett.*, 83:38004, 2008.
- [134] V. Dolnik. Capillary electrophoresis of proteins 2003-2005. *Electrophoresis*, 27(1):126–141, 2006.
- [135] H. Cottet, C. Simo, W. Vayaboury, and A. Cifuentes. Nonaqueous and aqueous capillary electrophoresis of synthetic polymers. *Journal of Chromatography A*, 1068(1):59–73, 2005.
- [136] H. Cottet and P. Gareil. *CE from small ions to Macromolecules, in the Serie Methods in Molecular Biology, Molecular Medicine and Biotechnology*, chapter Separation of synthetic (co)polymers by capillary electrophoresis techniques. Humana Press, NJ, USA, 2007.
- [137] E. O. Stejskal and J. E. Tanner. Spin diffusion measurements - spin echoes in presence of a time-dependent field gradient. *J. Chem. Phys.*, 42(1):288–&, 1965.
- [138] P. Stilbs and I. Furo. Electrophoretic nmr. *Current Opinion In Colloid & Interface Science*, 11(1):3–6, 2006.
- [139] U. Scheler. *Handbook of Polyelectrolytes and Their Application, Vol. 2*, page 173ff. Tripaty, S. K. and Kumar, J. and Nalwa, H. S., 2002.
- [140] U. Böhme and U. Scheler. Effective charge of poly(styrenesulfonate) and ionic strength - an electrophoresis nmr investigation. *Colloids and Surfaces A-Physicochemical and Engineering Aspects*, 222(1-3):35–40, 2003. doi: DOI10.1016/S0927-7757(03)00230-9.
- [141] U. Böhme and U. Scheler. Hydrodynamic size and electrophoretic mobility of poly(styrene sulfonate) versus molecular weight. *Macromolecular Chemistry and Physics*, 208(19-20):2254–2257, 2007. doi: DOI10.1002/macp.200700386.

- [142] U. Böhme and U. Scheler. Hydrodynamic size and charge of polyelectrolyte complexes. *Journal of Physical Chemistry B*, 111(29):8348–8350, 2007. doi: DOI10.1021/jp070611e.
- [143] M. G. Khaledi, editor. *High-Performance Capillary Electrophoresis*. John Wiley & Sons, Inc., New York, 1998.
- [144] A. Gottwald, P. Kuran, and U. Scheler. Separation of velocity distribution and diffusion using pfg nmr. *Journal of Magnetic Resonance*, 162(2):364–370, 2003.
- [145] J. D. van Beek. matnmr: A flexible toolbox for processing, analyzing and visualizing magnetic resonance data in matlab(r). *Journal of Magnetic Resonance*, 187:19, 2007.
- [146] H. Cottet and P. Gareil. From small charged molecules to oligomers: A semiempirical approach to the modeling of actual mobility in free solution. *Electrophoresis*, 21(8):1493–1504, 2000.
- [147] N. C. Stellwagen, C. Gelfi, and P. G. Righetti. The free solution mobility of dna. *Biopolymers*, 42(6):687–703, 1997.
- [148] N. C. Stellwagen, S. Magnusdottir, C. Gelfi, and P. G. Righetti. Measuring the translational diffusion coefficients of small dna molecules by capillary electrophoresis. *Biopolymers*, 58(4):390–397, 2001.
- [149] V. Lobaskin, B. Dünweg, M. Medebach, T. Palberg, and C. Holm. Electrophoresis of colloidal dispersions in the low-salt regime. *Phys. Rev. Lett.*, 98:176105, 2007.
- [150] B. Dünweg, V. Lobaskin, K. Seethalakshmy-Hariharan, and C. Holm. Colloidal electrophoresis: scaling analysis, green-kubo relation, and numerical results. *Journal of Physics: Condensed Matter*, 20:404214, 2008.
- [151] A. Chatterji and J. Horbach. Electrophoretic properties of highly charged colloids: A hybrid molecular dynamics/lattice boltzmann simulation study. *The Journal of Chemical Physics*, 126(6):064907, 2007.
- [152] V. Lobaskin, B. Dünweg, and C. Holm. Electrophoretic mobility of a charged colloidal particle: a computer simulation study, 2004. *Journal of Physics-Condensed Matter*.
- [153] T. Palberg, M. Medebach, N. Garbow, M. Evers, A. Barreira Fontecha, H. Reiber, and E. Bartsch. Electrophoresis of model colloidal spheres in low salt aqueous suspension. *J. Phys.: Condens. Matter*, 16:4039–4050, 2004.
- [154] D Long and A Ajdari. A note on the screening of hydrodynamic interactions, in electrophoresis, and in porous media. *European Physical Journal E*, 4(1): 29–32, 2001.
- [155] M Tanaka and AY Grosberg. Giant charge inversion of a macroion due to multivalent counterions and monovalent coions: Molecular dynamics study.

Bibliography

- Journal of Chemical Physics*, 115(1):567–574, 2001.
- [156] R. J. Meagher, J. I. Won, L. C. McCormick, S. Nedelcu, M. M. Bertrand, J. L. Bertram, G. Drouin, A. E. Barron, and G. W. Slater. End-labeled free-solution electrophoresis of dna. *Electrophoresis*, 26(2):331–350, 2005. doi: DOI10.1002/elps.200410219.
- [157] R. J. Meagher, L. C. McCormick, R. D. Haynes, J. I. Won, J. S. Lin, G. W. Slater, and A. E. Barron. Free-solution electrophoresis of dna modified with drag-tags at both ends. *Electrophoresis*, 27(9):1702–1712, 2006. doi: DOI10.1002/elps.200500554.
- [158] L. C. McCormick and G. W. Slater. The molecular end effect and its critical impact on the behavior of charged-uncharged polymer conjugates during free-solution electrophoresis. *Electrophoresis*, 26(9):1659–1667, 2005.
- [159] R. D. Haynes, R. J. Meagher, J. I. Won, F. M. Bogdan, and A. E. Barron. Comblike, monodisperse polypeptoid drag-tags for dna separations by end-labeled free-solution electrophoresis (elfse). *Bioconjugate Chemistry*, 16(4):929–938, 2005. doi: DOI10.1021/bc0496915.
- [160] S. Nedelcu and G. W. Slater. Branched polymeric labels used as drag-tags in free-solution electrophoresis of ssdna. *Electrophoresis*, 26(21):4003–4015, 2005. doi: DOI10.1002/elps.200500471.
- [161] S. T. Grosser, J. M. Savard, and J. W. Schneider. Identification of pcr products using pna amphiphiles in micellar electrokinetic chromatography. *Analytical Chemistry*, 79(24):9513–9519, 2007. doi: DOI10.1021/ac7016376.
- [162] J. M. Savard and J. W. Schneider. Sequence-specific purification of dna oligomers in hydrophobic interaction chromatography using peptide nucleic acid amphiphiles: Extended dynamic range. *Biotechnology and Bioengineering*, 97(2):367–376, 2007. doi: DOI10.1002/bit.21242.
- [163] J. M. Savard, S. T. Grosser, and J. W. Schneider. Length-dependent dna separations using multiple end-attached peptide nucleic acid amphiphiles in micellar electrokinetic chromatography. *Electrophoresis*, 29(13):2779–2789, 2008. doi: DOI10.1002/elps.200700580.
- [164] D. Long, A. V. Dobrynin, M. Rubinstein, and A. Ajdari. Electrophoresis of polyampholytes. *Journal of Chemical Physics*, 108(3):1234–1244, 1998.
- [165] L. C. McCormick, G. W. Slater, A. E. Karger, W. N. Vreeland, A. E. Barron, C. Desruisseaux, and G. Drouin. Capillary electrophoretic separation of uncharged polymers using polyelectrolyte engines - theoretical model. *Journal of Chromatography a*, 924(1-2):43–52, 2001.
- [166] L. C. McCormick and G. W. Slater. Molecular deformation and free-solution electrophoresis of dna-uncharged polymer conjugates at high field strengths: Theoretical predictions. part 1: Hydrodynamic segregation. *Electrophoresis*, 28(4):674–682, 2007. doi: DOI10.1002/elps.200600590.

- [167] V. Lobaskin and B. Dünweg. A new model for simulating colloidal dynamics. *New Journal of Physics*, 6, 2004. doi: ARTN54.
- [168] P.-Y. Hsiao. Chain morphology, swelling exponent, persistence length, like-charge attraction, and charge distribution around a chain in polyelectrolyte solutions: Effects of salt concentration and ion size studied by molecular dynamics simulations. *Macromolecules*, 39(20):7125–7137, 2006. doi: ARTNMA0609782.
- [169] M. Ullner and C. E. Woodward. Orientational correlation function and persistence lengths of flexible polyelectrolytes. *Macromolecules*, 35(4):1437–1445, 2002. doi: 10.1021/ma010863s. URL <http://pubs.acs.org/doi/abs/10.1021/ma010863s>.
- [170] H. B. Luo and D. Gersappe. Modeling the dynamics of dna electrophoresis on a flat surface. *Electrophoresis*, 23(16):2690–2696, 2002.
- [171] Y. S. Seo, H. B. Luo, V. A. Samuilov, M. H. Rafailovich, J. Sokolov, D. Gersappe, and B. Chu. Dna electrophoresis on nanopatterned surfaces. *Nano Letters*, 4(4):659–664, 2004. doi: DOI10.1021/nl0498435.
- [172] B. Q. Li, X. H. Fang, H. B. Luo, E. Petersen, Y. S. Seo, V. Samuilov, M. Rafailovich, J. Sokolov, D. Gersappe, and B. Chu. Influence of electric field intensity, ionic strength, and migration distance on the mobility and diffusion in dna surface electrophoresis. *Electrophoresis*, 27(7):1312–1321, 2006. doi: DOI10.1002/elps.200500444.
- [173] C. J. O. Reichhardt and C. Reichhardt. Electrophoresis of dna on a disordered two-dimensional substrate. *Physical Review E*, 74(5):051908, 2006. doi: ARTN051908.
- [174] N. Hoda and S. Kumar. Brownian dynamics simulations of polyelectrolyte adsorption onto topographically patterned surfaces. *Langmuir*, 23(23):11747–11760, 2007. doi: DOI10.1021/la701356a.
- [175] T. W. Odom, V. R. Thalladi, J. C. Love, and G. M. Whitesides. Generation of 30–50 nm structures using easily fabricated, composite pdms masks. *Journal of the American Chemical Society*, 124(41):12112–12113, 2002. doi: DOI10.1021/ja0209464.
- [176] C. W. Kan, C. P. Fredlake, E. A. S. Doherty, and A. E. Barron. Dna sequencing and genotyping in miniaturized electrophoresis systems. *Electrophoresis*, 25(21-22):3564–3588, 2004. doi: DOI10.1002/elps.200406161.
- [177] C. K. Fredrickson and Z. H. Fan. Macro-to-micro interfaces for microfluidic devices. *Lab On a Chip*, 4(6):526–533, 2004. doi: DOI10.1039/b410720a.
- [178] W. Reisner, K. J. Morton, R. Riehn, Y. M. Wang, Z. N. Yu, M. Rosen, J. C. Sturm, S. Y. Chou, E. Frey, and R. H. Austin. Statics and dynamics of single dna molecules confined in nanochannels. *Physical Review Letters*, 94(19):196101, 2005. doi: ARTN196101.

Bibliography

- [179] M. Krishnan, I. Moench, and P. Schuille. Spontaneous stretching of dna in a two-dimensional nanoslit. *Nano Letters*, 7(5):1270–1275, 2007. doi: DOI10.1021/nl0701861.
- [180] S. Pennathur and J. G. Santiago. Electrokinetic transport in nanochannels. 2. experiments. *Analytical Chemistry*, 77(21):6782–6789, 2005. doi: DOI10.1021/ac0508346.
- [181] S. Pennathur, F. Baldessari, J. G. Santiago, M. G. Kattah, J. B. Steinman, and P. J. Utz. Free-solution oligonucleotide separation in nanoscale channels. *Analytical Chemistry*, 79(21):8316–8322, 2007. doi: DOI10.1021/ac0710580.
- [182] A. Balducci, P. Mao, J. Han, and P. S. Doyle. Double-stranded dna diffusion in slitlike nanochannels. *Macromolecules*, 39(18):6273–6281, 2006. doi: DOI10.1021/ma061047t.
- [183] J. J. Zheng and E. S. Yeung. Anomalous radial migration of single dna molecules in capillary electrophoresis. *Analytical Chemistry*, 74(17):4536–4547, 2002. doi: DOI10.1021/ac0257344.
- [184] J. J. Zheng and E. S. Yeung. Mechanism for the separation of large molecules based on radial migration in capillary electrophoresis. *Analytical Chemistry*, 75(15):3675–3680, 2003. doi: DOI10.1021/ac034430u.
- [185] Y. L. Chen, M. D. Graham, J. J. de Pablo, G. C. Randall, M. Gupta, and P. S. Doyle. Conformation and dynamics of single dna molecules in parallel-plate slit microchannels. *Physical Review E*, 70(6):060901, 2004. doi: ARTN060901.
- [186] Y. L. Chen, M. D. Graham, J. J. de Pablo, K. Jo, and D. C. Schwartz. Dna molecules in microfluidic oscillatory flow. *Macromolecules*, 38(15):6680–6687, 2005. doi: DOI10.1021/ma050238d.
- [187] R. M. Jendrejack, E. T. Dimalanta, D. C. Schwartz, M. D. Graham, and J. J. de Pablo. Dna dynamics in a microchannel. *Physical Review Letters*, 91(3):038102, 2003. doi: ARTN038102.
- [188] R. M. Jendrejack, D. C. Schwartz, M. D. Graham, and J. J. de Pablo. Effect of confinement on dna dynamics in microfluidic devices. *Journal of Chemical Physics*, 119(2):1165–1173, 2003. doi: DOI10.1063/1.1575200.
- [189] R. M. Jendrejack, D. C. Schwartz, J. J. de Pablo, and M. D. Graham. Shear-induced migration in flowing polymer solutions: Simulation of long-chain deoxyribose nucleic acid in microchannels. *Journal of Chemical Physics*, 120(5):2513–2529, 2004. doi: DOI10.1063/1.1637331.
- [190] J. P. Hernandez-Ortiz, H. Ma, J. J. de Pablo, and M. D. Graham. Cross-stream-line migration in confined flowing polymer solutions: Theory and simulation. *Physics of Fluids*, 18(12), 2006. doi: ARTN123101.
- [191] O. B. Usta, A. J. C. Ladd, and J. E. Butler. Lattice-boltzmann simulations of the dynamics of polymer solutions in periodic and confined geometries.

- Journal of Chemical Physics*, 122(9):094902, 2005. doi: ARTN094902.
- [192] O. B. Usta, J. E. Butler, and A. J. C. Ladd. Flow-induced migration of polymers in dilute solution. *Physics of Fluids*, 18(3):031703, 2006. doi: ARTN031703.
- [193] O. B. Usta, J. E. Butler, and A. J. C. Ladd. Transverse migration of a confined polymer driven by an external force. *Physical Review Letters*, 98(9):098301, 2007. doi: ARTN098301.
- [194] Y. L. Chen, H. Ma, M. D. Graham, and J. J. de Pablo. Modeling dna in confinement: A comparison between the brownian dynamics and lattice boltzmann method. *Macromolecules*, 40(16):5978–5984, 2007. doi: DOI10.1021/ma070729t.
- [195] J. Mathe, J.-M. Di Meglio, and B. Tinland. Electrophoretic separation of large dnas using steric confinement. *Journal of Colloid and Interface Science*, 316(2):831–835, 2007. doi: DOI10.1016/j.jcis.2007.07.063.
- [196] J. Mathe, J.-M. Di Meglio, and B. Tinland. Diffusion of latex and dna chains in 2d confined media. *Journal of Colloid and Interface Science*, 322(1):315–320, 2008. doi: DOI10.1016/j.jcis.2008.02.005.
- [197] J. D. Cross, E. A. Strychalski, and H. G. Craighead. Size-dependent dna mobility in nanochannels. *Journal of Applied Physics*, 102(2):024514, 2007. doi: ARTN024514.
- [198] S. Pennathur and J. G. Santiago. Electrokinetic transport in nanochannels. 1. theory. *Analytical Chemistry*, 77(21):6772–6781, 2005.
- [199] L. Onsager. Reciprocal relations in irreversible processes. i. *Physical Review*, 37(4):405–426, 1931.
- [200] L. Onsager. Reciprocal relations in irreversible processes. ii. *Physical Review*, 38(12):2265–2279, 1931.
- [201] K. Grass, M. O. Steinhauser, K. Thoma, and A. Blumen. Sequential modelling of failure behavior in cohesive brittle materials. In *Powders and Grains*, page 1447. Balkema Publ., Leiden, 2005.
- [202] M. O. Steinhauser and K. Grass. Failure and plasticity models of ceramics. a numerical study. In *Dislocations, Plasticity, Damage and Metal Forming: Material Response and Multiscale Modeling - Proceedings of PLASTICITY '05*. Neat Press, Maryland, USA, 2005.
- [203] M. O. Steinhauser, K. Grass, K. Thoma, and A. Blumen. Impact dynamics and failure of brittle solid states by means of nonequilibrium molecular dynamics simulations. *Europhysics Letters*, 73(1):62–68, 2006.
- [204] M. O. Steinhauser, K. Grass, E. Strassburger, and A. Blumen. Impact failure of granular materials - non-equilibrium multiscale simulations and high-speed experiments. *International Journal of Plasticity*, 1(25):161–182, 2009.

CURRICULUM VITAE

KAI CHRISTIAN GRASS

PERSONAL DETAILS

Date of birth: 7th of January, 1980

Place of birth: Bielefeld, Germany

Citizenship: German

ACADEMIC CAREER

- 10/2005–2/2009 PhD in theoretical physics at the Frankfurt Institute for Advanced Studies (FIAS), JW Goethe-University Frankfurt under the supervision of PD Dr. Christian Holm
- 7/2008–9/2008 Research stay at Université d'Ottawa, Ontario, Canada with Prof. Dr. Gary W. Slater
- 5/2007–9/2007 Research stay at Université d'Ottawa
- 2/2002–12/2002 Student at University of Auckland, New Zealand
- 12/2002 Postgraduate Diploma in Science (Applied Mathematics)
- 5/2000–6/2005 Physics student at Albert-Ludwigs-University Freiburg
- 6/2005 Diploma in physics (Grade: 1.2)
Diploma thesis with Prof. Dr. Alexander Blumen in cooperation with the Fraunhofer Institute for high-speed dynamics (EMI), Freiburg.
Thesis title: “Modelle zum Versagensverhalten von spröden Materialien” (Models for failure prediction in brittle materials)
- 10/2001 Vordiplom in physics (Grade: 1.1)
- 9/1999–3/2000 Distance/Online course in physics at the Technical University of Kaiserslautern (“FiPS”)
-

EDUCATION

- 6/1999 Abitur at Humboldt Gymnasium, Bad Pyrmont (Grade: 1.0)

PROFESSIONAL EXPERIENCE

- 2/2008–5/2008 Internship at Bain & Company, Munich
- 8/2005–9/2005 Trainee at Accenture Technology Solutions, Kronberg
- 5/2003–2/2004 Student researcher at Fraunhofer Institute for high-speed dynamics (EMI), Freiburg
-

COMMUNITY SERVICE

- 8/1999–5/2000 Community service at Arbeiterwohlfahrt Freiburg
-

HONARY WORK

- since 6/2007 Leader of e-fellows.net city group Frankfurt:
Organisation of monthly meetings and special events with co-operation partners
- since 2/2006 Representative of FIGSS graduate students:
Organisation of FIAS student seminar and of regular events for the student community
-

SCHOLARSHIPS

- since 8/2007 Member of the Otto Stern School for Integrated Doctoral Education
- since 10/2006 DAAD (German Academic Exchange Service) PPP scholarship for a two year research project with Prof. Dr. G. W. Slater, Université d'Ottawa, Ontario, Kanada
- since 10/2005 Scholarship of the foundation of the Johann Wolfgang Goethe-University, Frankfurt am Main
- since 10/2005 Member of Frankfurt International Graduate School for Science (FIGSS)
- since 2/2003 e-fellows.net online scholarship

PUBLICATION LIST

- K. Grass, M. O. Steinhauser, K. Thoma, and A. Blumen. Sequential modelling of failure behavior in cohesive brittle materials. In *Powders and Grains*, page 1447. Balkema Publ., Leiden, 2005
- M. O. Steinhauser and K. Grass. Failure and plasticity models of ceramics. a numerical study. In *Dislocations, Plasticity, Damage and Metal Forming: Material Response and Multiscale Modeling - Proceedings of PLASTICITY '05*. Neat Press, Maryland, USA, 2005
- M. O. Steinhauser, K. Grass, K. Thoma, and A. Blumen. Impact dynamics and failure of brittle solid states by means of nonequilibrium molecular dynamics simulations. *Europhysics Letters*, 73(1):62–68, 2006
- M. O. Steinhauser, K. Grass, E. Strassburger, and A. Blumen. Impact failure of granular materials - non-equilibrium multiscale simulations and high-speed experiments. *International Journal of Plasticity*, 1(25):161–182, 2009
- K. Grass, U. Böhme, U. Scheler, H. Cottet, and C. Holm. Importance of hydrodynamic shielding for the dynamic behavior of short polyelectrolyte chains. *Physical Review Letters*, 100(9):096104, 2008
- K. Grass and C. Holm. On the importance of hydrodynamic interactions in polyelectrolyte electrophoresis. *J. Phys.: Condens. Matter*, 20(494217), 2008
- K. Grass and C. Holm. Polyelectrolytes in electric fields: Measuring the dynamical effective charge and effective friction. *Soft Matter*, *accepted*, 2009. <http://arxiv.org/abs/0902.1886>
- K. Grass, C. Holm, and G. W. Slater. Optimizing end-labeled free-solution electrophoresis by increasing the hydrodynamic friction of the drag labels. *Submitted to Macromolecules*, 2009. <http://arxiv.org/abs/0902.1889>
- G. W. Slater, C. Holm, M. V. Chubynsky, H. W. de Haan, A. Dubé, K. Grass, O. A. Hickey, C. Kingsbury, D. Sean, T. N. Shendruk, and L. Zhan. Modeling separation processes: A review of current computer simulation methods. *Electrophoresis*, (30):792–818, 2009